

SIMULATION AND CHARACTERIZATION OF A DENSE PLASMA FOCUS DEVICE

A Thesis Submitted to the College of
Graduate and Postdoctoral Studies
In Partial Fulfillment of the Requirements
For the Degree of Master of Science
In the Department of Physics and Engineering Physics
University of Saskatchewan
Saskatoon

By
Seanne Chung

Permission to Use

In presenting this thesis/dissertation in partial fulfillment of the requirements for a Post-graduate degree from the University of Saskatchewan, I agree that the Libraries of this University may make it freely available for inspection. I further agree that permission for copying of this thesis/dissertation in any manner, in whole or in part, for scholarly purposes may be granted by the professor or professors who supervised my thesis/dissertation work or, in their absence, by the Head of the Department or the Dean of the College in which my thesis work was done. It is understood that any copying or publication or use of this thesis/dissertation or parts thereof for financial gain shall not be allowed without my written permission. It is also understood that due recognition shall be given to me and to the University of Saskatchewan in any scholarly use which may be made of any material in my thesis/dissertation.

Disclaimer

Reference in this thesis/dissertation to any specific commercial products, process, or service by trade name, trademark, manufacturer, or otherwise, does not constitute or imply its endorsement, recommendation, or favoring by the University of Saskatchewan. The views and opinions of the author expressed herein do not state or reflect those of the University of Saskatchewan, and shall not be used for advertising or product endorsement purposes.

Requests for permission to copy or to make other uses of materials in this thesis/dissertation in whole or part should be addressed to:

Department Head
Physics and Engineering Physics Department
University of Saskatchewan
116 Science Place
Saskatoon, Saskatchewan S7N 5E2
Canada

or

Dean
College of Graduate and Postdoctoral Studies
University of Saskatchewan
110 Science Place
Saskatoon, Saskatchewan S7N 5C9
Canada

Abstract

Electron temperatures have been measured in a 1 kJ Mather-type dense plasma focus device (UofS-I DPF) with a hollow copper anode at the University of Saskatchewan (UofS) Plasma Physics Lab (PPL). The UofS-I DPF device is powered by a 5 μF capacitor bank charged up to 20 kV with an optimum operating pressure of 100 - 200 mTorr argon gas. The features of the plasma dynamics in the UofS-I DPF device have been studied by analyzing signals of the discharge current, the anode voltage, the intensities of electron and ion beams, and the soft x-ray (SXR) and hard x-ray (HXR) radiations. The peak times of signals have been compared with the pinch time. A negatively-biased BPX-65 Si-PIN photodiode array has been used to measure SXR emissions from the UofS-I DPF. The double-filter technique and the ratio method have been used to determine the electron temperature based on the measured SXR intensities. An electron temperature of 5.7 ± 0.7 keV has been obtained for the argon plasma. Moreover, linear correlations of the current dip, the peaks of the electron beam and the SXR and HXR emissions with the peak of the anode voltage have been observed. Linear correlations of the same signals with the electron temperature have also been observed.

The Lee model code has been used to determine the optimum capacitor bank voltage and operating pressure for the UofS-I DPF. The Lee code has also been used for fitting the experimental current waveform to the computed waveform in order to obtain the mass and current factors. These factors allow the computations of the radial positions and the speeds of the focusing plasma.

Acknowledgements

First off, I would like to express my deepest and most sincere gratitude to my mentor, professor and thesis adviser, Dr. Chijin Xiao, of the Plasma Physics Lab at the University of Saskatchewan. The door to Prof. Xiao's office has always been open especially whenever I needed his guidance the most. He has unconditionally dedicated his time to my progress and has willingly shared wholeheartedly his passion in science. More importantly, his uncompromising patience and understanding of my weaknesses kept my emotional and mental insanity at bay.

I would like to thank the experts who were involved in this research, most especially my colleague, Dr. Reza Alibazi Behbahani, who has shared his expertise in the field. He has provided me with academic and moral support and has always been available whenever I requested for his help. He has led the progress all throughout this research, so thus without him this would not have succeeded, nor initiated at the least.

I would also like to acknowledge the late Dr. Akira Hirose, Director of the Plasma Physics Lab, and Jiping Zhang, Manager of the Plasma Physics Lab, for allowing me to do my project efficiently and comfortably through their support. As well, the Plasma Physics Machine Shop staff, and my colleagues: Sayf Elgriw, Akbar Rohollahi, Michael Patterson, Joseph Adegun, Vincent Morin, Ayub Khodae, Igor Voldiner, and Heba Bsharat, for the fun, meaningful discussions and undying support.

Finally, I must express my very profound gratitude to my parents, Susan and Roberto, and to my brother and sisters, for providing me with their unfailing support and continuous encouragement throughout my years of study especially at times when I felt close to giving up, and for keeping my mental and physical health stable. This accomplishment would not have been possible without them. Thank you.

Dedicated to my family

Table of Contents

Permission to Use	i
Disclaimer	i
Abstract	ii
Acknowledgements	iii
Dedication	iv
List of Tables	vii
List of Figures	xv
Chapter 1	
Introduction	1
1.1 Plasma Temperature	2
1.2 Fusion in Plasmas	3
1.3 Magnetic Pinch	4
1.4 Goals of the Thesis	8
1.5 Thesis Outline	9
Chapter 2	
The Dense Plasma Focus	10
2.1 DPF Plasma Dynamics	11
2.1.1 Breakdown Phase	12
2.1.2 Axial Rundown Phase	14
2.1.3 Radial-Compression Phase	15
2.1.3.1 Compression Phase	15
2.1.3.2 Quiescent Phase	17
2.1.3.3 Unstable Phase	17
2.1.3.4 Decay Phase	18
2.2 The Lee Model	18
2.2.1 Model Equations	19

Chapter 3	
X-ray Emission from DPF	22
3.1 Silicon-PIN Photodiodes	25
3.2 Ratio Method on SXR's	28
Chapter 4	
The UofS-I Dense Plasma Focus Device	31
4.1 Design Consideration	32
4.2 Device Schematic, Circuit, and Controls	34
4.3 Electrical Parameter Measurements	38
4.3.1 Current Measurement	38
4.3.2 High Voltage Measurement	43
4.3.3 Soft and Hard X-ray Measurements	43
4.3.4 Ion Beam Measurement	48
4.3.5 Data Acquisition	50
4.4 UofS-I DPF Operation and Parameters	52
Chapter 5	
Simulation and Experimental Results	55
5.1 UofS-I DPF Plasma Dynamics	55
5.2 Lee Model Simulation	58
5.3 Electron Temperature Measurement	63
5.4 Correlation of DPF Properties with the Anode Voltage	73
5.5 Correlation of DPF Properties with the Electron Temperature	81
Chapter 6	
Summary and Suggested Future Work	84
References	87

List of Tables

4.1 The UofS-I DPF device parameters and locations of detectors. 54

5.1 Summary of ratios and corresponding interpolated temperatures for different cobalt foil filter thicknesses. Electron temperatures range from a minimum of 4.35 keV and a maximum of 6.6 keV. An overall average for the electron temperature is 5.7 ± 0.7 keV. 72

List of Figures

1.1	The four states of matter at different stages of energy: solid, liquid, gas, and plasma.	1
1.2	Classification of some natural and laboratory plasmas. Plasma pinches and thermonuclear fusion plasmas are achieved in extreme conditions of electron temperatures and electron densities.	3
1.3	The tokamak device that uses magnetic field to confine plasma in a torus shape. It consists of poloidal and toroidal magnetic field coils to create magnetic field lines that run helically around the torus center [7].	4
1.4	An axial current induces an azimuthal magnetic field resulting in a radially $\mathbf{J} \times \mathbf{B}$ force compressing the plasma radially inwards toward the center. A compression, or “pinch”, results in the direction of the Lorentz force.	5
1.5	The Z-pinch. The current flows in the z direction, inducing a magnetic field flowing in the θ direction. A Lorentz force is induced in the radially inward direction, pinching the plasma toward the center.	6
1.6	The θ -pinch. The external coil current, J_{ext} , flows in the θ direction, inducing a current, J , plasma in the opposite azimuthal direction and a magnetic field in the z direction in the plasma. A Lorentz force is induced in the radially inward direction, pinching the plasma toward the center.	6
2.1	The two types of DPF designs: Filippov-type (left) and Mather-type (right). Both are similar in plasma dynamics and components but differ in aspect ratios and geometry. The umbrella-shaped lines indicate the current sheath moving upwards to the top of the electrode and then being compressed radially to form a hot and dense plasma.	11
2.2	Plasma focus dynamics: break-down, acceleration, and radial compression phases; radiation and neutron emission, and the electron and ion beam emissions from the focusing region.	13
2.3	Plasma compression-voltage comparison chart showing the time evolution of the sheath with respect to the voltage, and that the peak of the anode voltage corresponds to the maximum compression of the plasma sheath [16].	16
2.4	The DPF electrodes’ configuration and dimensions and plasma dimensions used in the Lee code in the axial (left) and radial (right) phases [11].	19
2.5	The DPF circuit diagram used in the Lee code.	21

3.1	The model of the production of Bremsstrahlung x-rays producing a continuum spectrum of radiation caused by the retardation of the incident electron approaching a target atom.	23
3.2	The model of the characteristic line radiation x-ray emission: electrons (in orange) orbiting the nucleus (in green) at different orbital states (or shells). EM radiation in the x-ray energy range are emitted due to energy loss due to electron transitions from a higher to a lower orbital state.	24
3.3	The expected experimental spectrum (in green) of the superposition of both continuum (in blue) and line/characteristic (in yellow) x-ray spectra.	25
3.4	PIN diode schematic in reverse-bias with a large intrinsic layer (the depletion region) in between the P- and N- type layers.	26
3.5	PIN diode cross-section with photon absorption and electron-hole pair dynamics. Electron-hole pairs are formed in the intrinsic layer from the photons absorbed through the p-type layer. Electrons (green circles) are swept to the n-type layer and the holes (red circles) into the p-type layer due to the applied potential.	27
3.6	Typical BPX-65 reverse-biased circuit diagram [32].	28
4.1	The UofS-I dense plasma focus device. A control panel is situated beside the DPF device, and a Faraday cage built by means of copper mesh encloses the signals measurement devices.	31
4.2	Electrodes in vacuum: a hollow copper anode nested in 12 concentric cathode rods, and a quartz-infused glass insulator separating the electrodes.	32
4.3	The UofS-I DPF device schematic of the major components and detectors with respect to the pinch position. The gas inlet and outlet are situated on the same side. X-ray detectors point directly to the pinch position, while the charged particles detectors are placed in opposite directions in the z-axis. A Rogowski coil measures the current through the grounded wire connected to the electron beam collector, and a Faraday cup is placed inside the chamber opposite the electron beam collector.	34
4.4	A cross-section of the UofS-I DPF showing the electrodes' assembly and dimensions enclosed in the vacuum chamber. Twelve copper rods act as the cathode which concentrically nests the copper anode inside, both separated by a quartz-infused glass insulator. The electron beam collector is situated concentrically inside the electrodes' configuration and is 150 mm away from the anode tip.	35
4.5	The UofS-I DPF trigger circuit.	36

4.6	DPF control panel: chamber pressure display in Torr (top panel), automated or manual controls for firing/charging/discharging (middle panel), and the power supply controls for capacitor charging (bottom panel).	37
4.7	Charging and discharging Ross relays used for three different operational states: charging, discharging, and dumping of capacitor. The dumping resistor (behind the relays) consists of parallel resistors in series, equivalently 6.6 M Ω	38
4.8	Rogowski coil equivalent circuit encircling a current path (in green). Rogowski coil turns (in yellow) wound an internal loop (in blue) forming a toroidal configuration encircling the conducting wire for which the current is to be measured.	39
4.9	RC circuit used as a current integrator connected to the Rogowski coil. L and r are the internal inductance and resistance of the Rogowski coil, and R and C are the external resistor and capacitor. An output signal to oscilloscope is on the right.	40
4.10	Self-integrating circuit of the Rogowski coil. A small external resistor, R , is added to the input signal. An output signal to oscilloscope is on the right.	41
4.11	A commercial Rogowski coil used to measure the fast, high current waveform from the DPF discharge. Extra “Kapton” tape is added to provide high-voltage insulation.	42
4.12	A Tektroniks P6015a voltage probe used to measure the voltage of the DPF anode.	43
4.13	Negatively-biased BPX-65 circuit.	44
4.14	Silicon-PIN BPX-65 photodiodes and the circuit box.	45
4.15	A 4-PIN photodiode array attachment on one side of the chamber situated at the same distance from the pinch position as that of the other array under the chamber. The other array is shown in Fig. 4.16.	45
4.16	A 4-PIN photodiode array attachment under the chamber to allow more simultaneous detection of SXR per shot.	46
4.17	A 30-micron cobalt foil filter x-ray transmission as a function of photon energy in eV calculated using the CXRO site [54]. The curve shows a transmission window of 4 to 7.7 keV, which discriminates the copper line at 8.08 keV. The sharp drop of the transmission around 7.7 keV is due to the resonant absorption edge of cobalt.	46

4.18	Picture of the assembled scintillated PMT for detecting hard x-rays situated 2 meters away from the chamber in the Faraday cage, directly facing the anode tip.	48
4.19	A negatively-biased Faraday cup circuit.	48
4.20	The Faraday cup. The cup is attached inside the vacuum chamber and the collector end is situated 70 mm away from the anode tip. The copper layer on the surface of the cup is due to the copper impurities.	50
4.21	Tektronix oscilloscopes (TDS 2024c) for signals measurement and recording, with attached USB flash drives for storage. Each oscilloscope inputs 4 channels triggered by a common signal.	50
4.22	Tektronix oscilloscope (TDS 2024c) signals display: labels at bottom indicate divisions of four channels and time division of 500 ns. Ch. 1 (in orange) represents the inverted current trace with 50.0 V/div.; ch. 2 (in blue) represents the inverted HXR signal with 500 mV/div.; ch. 3 (in magenta) represents the electron beam signal with 5.00 V/div.; and ch. 4 (in green) represents the ion beam signal with 10.0 V/div. The signals are triggered by a common falling edge from ch. 1.	51
4.23	Timing sequence for operation in automation: capacitor charging duration of 25 s, buzzer at 25th s, fire at 28th s, dumping at 30th s with a duration of 30 s, and resets after 1 min. The cycle repeats after the reset.	53
5.1	Raw signals (from top to bottom): Discharge current from Rogowski coil, anode voltage from voltage probe, electron beam from charge collector and Rogowski coil, ion beam from Faraday cup, SXR from PIN diode, and HXR from PMT-scintillator. The different phases of plasma dynamics, and the time difference of peaks of signals relative to the pinch phase are also defined. . .	57
5.2	The model and operational parameters of the UofS-I DPF encoded onto the Lee code excel file for simulation and computation: The first two rows in the box are the DPF geometrical and electrical circuit parameters, the next two are the fitting and model parameters, and the last two are the operating parameters [39].	58
5.3	A short-circuit RLC current waveform signal of the UofS-I DPF measured using a Rogowski coil (solid blue), with a recorded and measured time period of around 5.3 μ s and a frequency of 188 kHz calculated from the zeroes of the sinusoid (vertical dashed red).	59

5.4	Calculated current waveforms at various charging voltages: 15 kV (dashed blue), 20 kV (solid red), and 25 kV (dotted green) at a fixed operating pressure of 150 mTorr of argon gas using the Lee code. An increase in current and a time shift of the current drop to the left, is evident due to an increase in charging voltage.	60
5.5	Calculated current waveforms at various operating pressures: 100 mTorr (dashed blue), 150 mTorr (solid red), 200 mTorr (dotted green) and 300 mTorr (solid violet) of argon gas at a fixed charging voltage of 20 kV using the Lee code. A time shift of the current drop to the left is evident as the pressure is decreased.	61
5.6	Comparison between the experimental (blue) and computed (red) discharge current waveforms. The fitting is nearly perfect, and both shows that the pinch phase starts at around 1.5 μ s.	62
5.7	The computed discharge current waveform (blue) and the anode voltage (pink) from the Lee code, showing the pinch effect corresponding to the peak of the voltage and the end of the current dip.	62
5.8	The computed axial plasma position (in blue) and the speed (in pink) in the axial trajectory, with a peak axial speed of 6.4 cm/ μ s. The gap in the curves indicate that the plasma trajectory is in the radial direction.	63
5.9	The computed radial positions: Radial inward shock (in dark blue), radial piston (in pink), pinch elongation (in yellow), and the radial reflected shock (in light blue). The pinch phase starts at 200 ns.	64
5.10	Attenuation length coefficients of titanium (dotted red), nickel (dashed green), cobalt (solid black), and silicon (dashed dotted blue), as a function of photon energy. The abrupt drops are due to the corresponding material's resonant absorption. The x-ray absorption K-edges of Ti, Ni, Co, and Si are 4.965 keV, 8.339 keV, 7.712 keV, and 1.840 keV, respectively.	65
5.11	The transmission of several foil filters: Ti of 30 microns (dotted red), Co of 5 μ m (solid black), Co of 20 μ m (solid yellow), Co of 30 μ m (solid blue), and Al of 50 μ m (dashed green). The Cu-K α at 8050 eV (dotted gray) is also drawn as a reference.	66
5.12	The calculated BPX-65 Si-PIN photodiode sensitivity with the thickness of the intrinsic and the active layers of the photodiodes are 0.5 μ m and 10 μ m, respectively.	67

5.13	The calculated response of the detector as a function of energy: Co of 10 μm with BPX-65 (solid black), Co of 15 μm with BPX-65 (dotted red), Co of 20 μm with BPX-65 (dashed green), Co of 25 μm with BPX-65 (dashed violet), Co of 30 μm with BPX-65 (dashed blue), and the Cu-K alpha line (dotted gray).	68
5.14	Argon spectrum at electron density of 10^{18} cm^{-3} and electron temperature of 6 keV. The spectrum is obtained based on calculation from the NIST site [57].	68
5.15	Ratio of response as a function of cobalt filter thickness for various temperatures: 3 keV (dotted green), 4 keV (dashed yellow), 5 keV (dashed red), 6 keV (dash-dot blue), and 7 keV (solid black). The reference filter thickness is 10 μm cobalt.	69
5.16	SXRs measured from Si-PIN BPX-65 detectors through different cobalt foil filters. Shot (a) at $p_0 = 100 \text{ mTorr}$ shows the measured intensities through 3 filters: Co 10 μm reference (black), Co 15 μm (green), and Co 20 μm (blue). Shot (b) at $p_0 = 130 \text{ mTorr}$ shows the measured intensities through the same filters: Co 10 μm reference (black), Co 25 μm (green), and Co 30 μm (blue). The percentage of intensities are labelled with respect to the reference intensity from the Co 10 μm reference. The pinch time shift is caused by the difference in operating gas pressure.	70
5.17	Ratio of experimental SXR intensities superimposed on the calibration curve. An electron temperature can be interpreted to fall in the range of 5.5 keV to 7.5 keV. An electron temperature average of 4.7 keV, 5.2 keV, 6.2 keV, and 6.1 keV were obtained from the Co 15 μm , 20 μm , 25 μm , and 30 μm , respectively. Based on data collected from 50 good discharges, the measured electron temperature is $5.7 \pm 0.7 \text{ keV}$	71
5.18	Anode voltage (in black) and Pearson Rogowski coil signal (in red) for shot (a) at $p_0 = 100 \text{ mTorr}$ and shot (b) at $p_0 = 130 \text{ mTorr}$. The vertical dashed lines indicate the plasma pinch times, which correspond to the voltage peak and the current dip. The shift in pinch time is due to the difference in operating pressure.	73
5.19	Correlation of the discharge current dip and the peak anode voltage of different shots at fixed running parameters of 20 kV charging voltage and 100-200 mTorr argon gas. A linear trend between the discharge current dip and the peak anode voltage can be observed (dashed red).	75

5.20	Anode voltage (in black) and electron beam signal (in green) for shot (a) at $p_0 = 100$ mTorr and shot (b) at $p_0 = 130$ mTorr. Dashed lines indicate the plasma pinch time which correspond to the voltage peak. A time delay between the pinch time and the electron beam peak is around 60 ns for both operating pressures.	75
5.21	Anode voltage (in black) and Faraday cup signal (in blue) for shot (a) at $p_0 = 100$ mTorr and shot (b) at $p_0 = 130$ mTorr. Dashed lines indicate the plasma pinch time which correspond to the voltage peak. A time delay between the pinch time and the ion beam peak is observed to be around 300 ns for both operating pressures.	76
5.22	Correlation of the electron beam (green circles) and ion beam (blue squares) intensities and the peak anode voltage of a collection of shots at fixed running parameters (20 kV charging voltage and 100-200 mTorr argon gas). A linear trend between the electron beam intensity and the peak voltage can be observed (dashed green). No apparent correlation for the ion beam intensity can be observed.	77
5.23	Anode voltage (in black) and BPX-65 photodiode signal (in magenta) for shot (a) at $p_0 = 100$ mTorr and shot (b) at $p_0 = 130$ mTorr. Dashed lines indicate the plasma pinch time which correspond to the voltage peak. A time delay between the pinch time and the SXR peak is observed to be around 30 ns for both operating pressures.	78
5.24	Anode voltage (in black) and HXR (in blue) for shot (a) at $p_0 = 100$ mTorr and shot (b) at $p_0 = 130$ mTorr. Dashed lines indicate the plasma pinch time which correspond to the voltage peak. A time delay between the HXR peak and the pinch time is about 120 ns for both operating pressures.	79
5.25	Correlation of the soft x-ray (magenta circles) and hard x-ray (blue squares) intensities and the peak anode voltage of different shots at fixed running parameters of 20 kV charging voltage and 100-200 mTorr argon gas. A linear trend for the soft x-rays and hard x-rays with the peak voltage can be observed (dashed magenta and blue, respectively).	80

5.26 Correlations with the electron temperature: (a) A linear correlation between the anode voltage (in black) and the electron temperature; (b) a linear correlation between the current dip (in red) and the electron temperature; (c) a linear correlation between the electron beam (in green) and the electron temperature, no correlation with the ion beam (in dark blue); and (d) a linear correlation between the SXR (in magenta) and HXR (in blue) with the electron temperature. 83

Chapter 1

Introduction

Plasma is commonly referred to as the fourth state of matter in addition to solid, liquid, and gas. In solids, molecules are held in place and arranged in a regular pattern. In liquids, molecules flow easily and assume the container shape. In gases, molecules are free and are far apart. When more energy is injected into the gas, some atoms may lose their electrons and some molecules may acquire extra electrons, forming a mixture of electrons, positively, negatively charged and neutral particles, called “plasma”.

These states of matter are consecutively formed with increasing temperatures, as shown in Fig. 1.1.

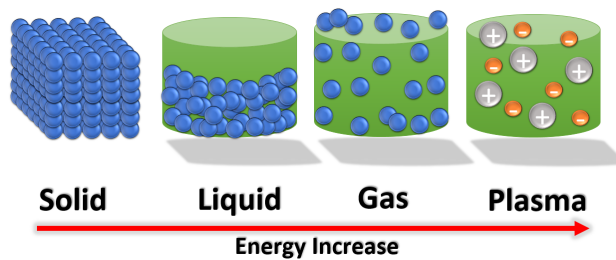


Figure 1.1: The four states of matter at different stages of energy: solid, liquid, gas, and plasma.

An example of a plasma is the sun where the temperatures surpass 10^7 K in its core [1]. Two other earlier known plasma phenomena include the lightning strikes and the aurora borealis, which occur at different magnitudes in pressure causing a drastic difference in their appearances. Plasmas lead to a number of important applications as a consequence of possessing such tremendous amounts of energies.

1.1 Plasma Temperature

The average kinetic energy of particles (electrons and ions) defines the plasma kinetic temperatures, T_e and T_i , respectively for electrons and ions. These energies follow a Maxwell-Boltzmann distribution function [2]. In plasmas where collisions dominate, the heavier species (ions, for example) and the electrons, among themselves, will have a Maxwellian distribution which allows the definition of the temperatures of the corresponding specie [3].

However, if the temperatures of the electron and the heavy particle are equal, the plasma is said to be in kinetic equilibrium. This equilibrium also requires that the energy gained by the electrons from the electric field between collisions should be extremely small relative to its average kinetic energy. In such a case, the electron temperature approaches the heavy particle temperature, which is a basic requirement for a plasma being in a state of *Local Thermodynamic Equilibrium (LTE)* [1].

Plasmas occur in a wide range of pressures and they are commonly classified in terms of electron densities and electron temperatures. Some other examples of plasmas include the solar corona, which has a temperature exceeding 10^6 K, the ionosphere, which is typically in the range of 10^3 K or lower, and flames that reach relatively high densities and temperatures. In extreme conditions, compressed plasmas (called “plasma pinches”) and thermonuclear fusion plasmas exist, where the electron and ion densities of 10^{26} m⁻³ and temperatures above 10^3 K up to 10^8 K can be achieved [4].

Figure 1.2 shows the parameter ranges of some of the classified natural and laboratory plasmas.

The mechanisms of plasma radiation is highly dependent on the plasma temperature. As a consequence, the plasma temperature measurements hold great importance for investigating the plasma radiation properties.

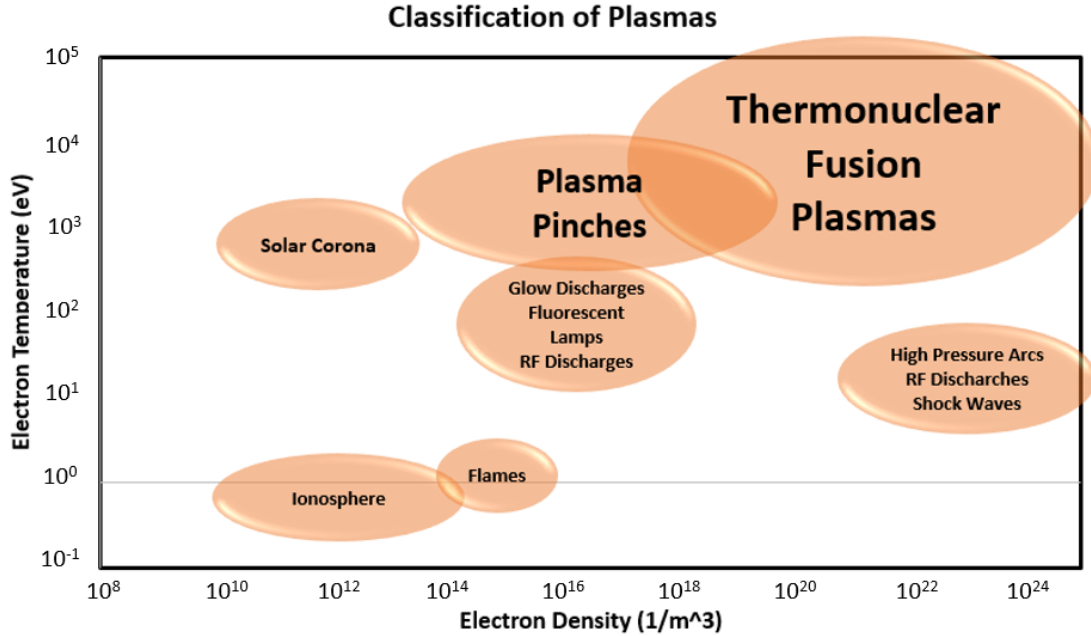


Figure 1.2: Classification of some natural and laboratory plasmas. Plasma pinches and thermonuclear fusion plasmas are achieved in extreme conditions of electron temperatures and electron densities.

1.2 Fusion in Plasmas

An example of fusion plasma is an environment wherein the temperature is in the order of 100 millions of Kelvin and density of 10^{20} m^{-3} . To produce such level of temperature and density, several major methods are explored: Magnetic Confinement Fusion (MCF), Inertial Confinement Fusion (ICF), and Magnetized Target Fusion (MTF).

Magnetic Confinement Fusion is an approach to use magnetic fields to confine the hot fusion fuel [6]. The charged particles gyrate around magnetic field lines due to the Lorentz force. Since plasmas consist of charged particles, transverse motion across the magnetic field lines are significantly reduced. This feature is used to confine the plasma particles by forcing the orbital motion and imposing a magnetic field pressure on the plasma.

Some examples of MCF devices are the tokamaks and stellarators [5]. The most promising candidate for MCF at present time is the tokamak [6] which is presented in Fig. 1.3.

Inertial Confinement Fusion research aims at creating nuclear fusion conditions by com-

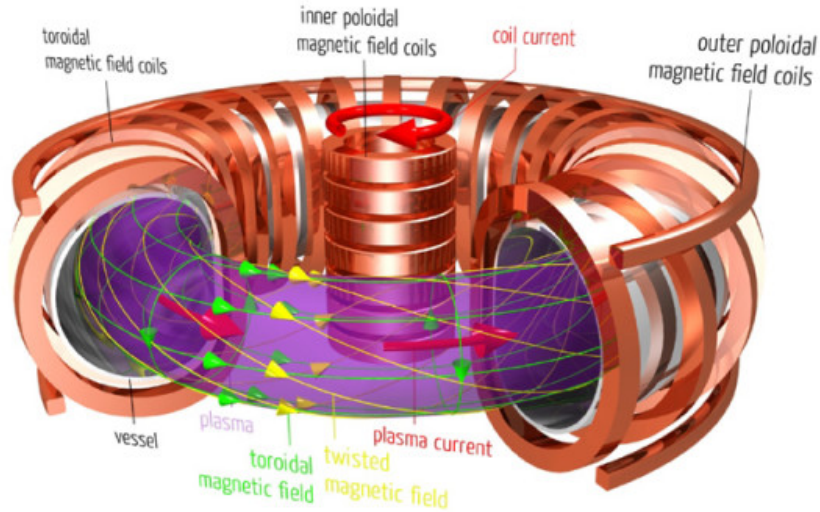


Figure 1.3: The tokamak device that uses magnetic field to confine plasma in a torus shape. It consists of poloidal and toroidal magnetic field coils to create magnetic field lines that run helically around the torus center [7].

pressing a fuel target using laser or electron beams. The target typically is in the form of a pellet that consists of a mixture of deuterium and tritium (D-T). To compress and heat the fuel, energy is delivered to the outer layer of the target using either high-energy beams of laser light, electrons, or ions. Since the confinement time is very short, it is necessary to have a high-density plasma [6].

Magnetized Target Fusion is the concept where a plasma target is compressed to thermonuclear conditions. The compression is not obtained through lasers or electron beams but by driving the magnetic or mechanical forces onto a solid or liquid metal lining to compress the fuels. An example of an MTF device is a Z-pinch. A Z-pinch device uses the concept of magnetic pinch to implode the plasma itself as a target, creating a compressed, hot and dense plasma [8].

1.3 Magnetic Pinch

The magnetic pinch is based on a strong current driven through the plasma. The current generates a magnetic field, \mathbf{B} , that squeezes the plasma to fusion conditions. If

some current, \mathbf{J} , is distributed continuously through the plasma, the plasma will be pulled together, compressing it and increasing the pressure. This compression is due to the induced Lorentz force, $\mathbf{J} \times \mathbf{B}$, that is orthogonal to the direction of the current and the induced magnetic field. This process will eventually stop when the increase in the plasma pressure gradient force equals the Lorentz force that compresses the plasma, that is, $\nabla p = \mathbf{J} \times \mathbf{B}$. This process is called the *pinch effect*. The process is shown in Fig. 1.4.

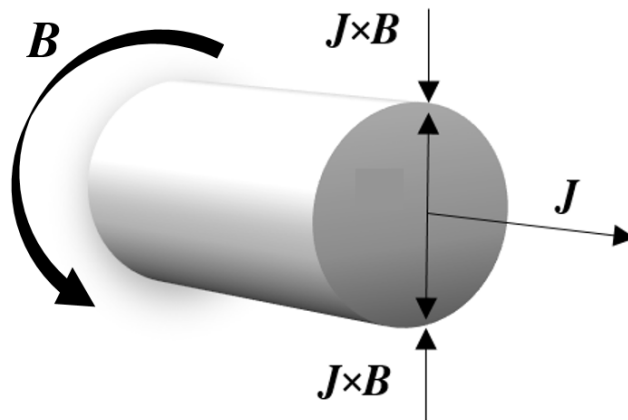


Figure 1.4: An axial current induces an azimuthal magnetic field resulting in a radially $\mathbf{J} \times \mathbf{B}$ force compressing the plasma radially inwards toward the center. A compression, or “pinch”, results in the direction of the Lorentz force.

Pinches were the early attempts for man-made controlled fusion reactors [8]. Some examples of the pinch devices are the Z-pinch and the θ (theta)-pinch. In a Z-pinch illustrated in Fig. 1.5, the current is driven in the axial (Z-) direction by a pair of parallel disk-like electrodes, and the magnetic field induced by the current is in the azimuthal (θ -) direction. The electromagnetic force induced is in the radially inward direction, compressing the high-density plasma toward the axis. In a θ pinch as shown on Fig. 1.6, the current in the plasma is induced by the current in a coil running in the azimuthal direction. The induced magnetic field is in the axial direction. The self-consistent $\mathbf{J} \times \mathbf{B}$ force is also radially inward.

The pinch configurations are named after the direction of the current. In the θ -pinch, the current flows in the θ direction. In a Z-pinch, the current flows in the z direction.

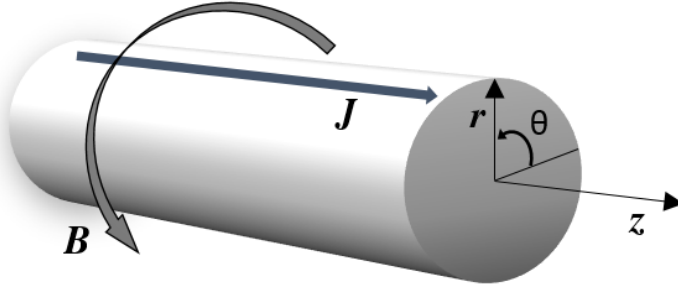


Figure 1.5: The Z-pinch. The current flows in the z direction, inducing a magnetic field flowing in the θ direction. A Lorentz force is induced in the radially inward direction, pinching the plasma toward the center.

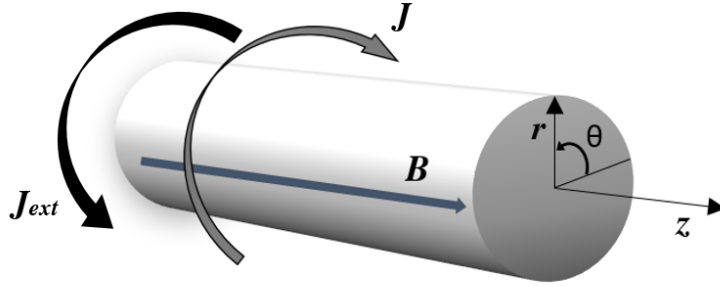


Figure 1.6: The θ -pinch. The external coil current, J_{ext} , flows in the θ direction, inducing a current, J , plasma in the opposite azimuthal direction and a magnetic field in the z direction in the plasma. A Lorentz force is induced in the radially inward direction, pinching the plasma toward the center.

The Z-pinch is somewhat orthogonal to the θ -pinch. A longitudinal current, $J_z(r)$, flowing in the plasma induces a magnetic field component, $B_\theta(r)$, thereby causing the Lorentz force in the radial inward direction.

Some basic equations describing the Z-pinch are determined as follows, assuming that all quantities are only functions of r [8]:

$$\nabla \cdot \mathbf{B} = 0 \quad \rightarrow \quad \frac{1}{r} \frac{\partial}{\partial r} (r B_r) + \frac{1}{r} \frac{\partial B_\theta}{\partial \theta} + \frac{\partial B_z}{\partial z} = 0 \quad (1.1)$$

But since $B_r = B_z = 0$,

$$\frac{\partial B_\theta}{\partial \theta} = 0 \quad (1.2)$$

which is satisfied trivially due to symmetry.

Applying Ampere's law:

$$\mathbf{J} = \frac{1}{\mu_0} \nabla \times \mathbf{B} \quad \rightarrow \quad J_z = \frac{1}{\mu_0 r} \frac{d}{dr}(r B_\theta) \quad (1.3)$$

where μ_0 is the vacuum permeability, and finding that only $J_z(r)$ is non-zero.

Applying the momentum equation (or the force balance equation):

$$\mathbf{J} \times \mathbf{B} = \nabla p \quad \rightarrow \quad J_z B_\theta = -\frac{dp}{dr} \quad (1.4)$$

where ∇p is the pressure force and finding that only the radial component yields a non-trivial equation.

Combining equations (1.3) and (1.4), one gets

$$\frac{dp}{dr} = -\frac{B_\theta}{\mu_0 r} \frac{d}{dr}(r B_\theta) = -\frac{B_\theta}{\mu_0} \frac{dB_\theta}{dr} - \frac{B_\theta^2}{\mu_0 r} \quad (1.5)$$

which can be rewritten as

$$\frac{d}{dr} \left(p + \frac{B_\theta^2}{2\mu_0} \right) = -\frac{B_\theta^2}{\mu_0 r} \quad (1.6)$$

Equation (1.6) is the Z-pinch radial pressure balance equation. The first term represents the particle pressure. The second term represents the magnetic pressure. The last term represents the generated tension force due to the curvature of the magnetic field lines.

In the earlier years of the fusion program, several linear Z-pinch devices were constructed. A typical Z-pinch device consists of a capacitor bank that is discharged across two electrodes located at each end of a hollow cylindrical insulator. A high voltage is supplied across the electrodes that ionizes the gas, creating a plasma. The current that is produced flows along

the plasma in the z -direction.

An example of a Z-pinch device is a dense plasma focus (DPF). It is in a certain way a form of a Z-pinch, wherein the current flowing in the z -axis provides the magnetic field confinement. Moreover, the dense plasma focus stands between the magnetic and the inertial confinement devices with regard to the time scales of the processes [10].

The dense plasma focus is a device for compressing and heating plasmas. The compressed, or the so-called “pinched”, plasma is column-shaped and appears like a point when viewed end-on [11]. This self-constriction of a cylinder of an electrically conducting plasma is where the “pinch effect” occurs. Moreover, it can produce a short-lived (50-100 ns) plasma of high density and temperature [10].

DPF devices can emit intensive ion beams [12,13] and electron beams [14,15,17,18], soft and hard x-rays [19–24], and neutron beams [25].

The charged particles from the DPF have been extensively and recently studied for applications such as a compact electron accelerator [15], production of energetic ions [12], and coating samples [26–28].

The DPF radiation spectrum in the x-ray region ranges from below 1 keV and up to 500 keV, and the emission times range from a few to a few hundred nanoseconds [20]. The electron temperature of the DPF plasma has been measured using x-rays to range from 3 to 7 keV [4,29–33]. X-rays from a DPF are also studied for applications such as x-ray lithography [34–36], microscopy [37], and radiography [38].

1.4 Goals of the Thesis

The main objectives of this thesis work is outlined below:

1. Studying the features of the plasma dynamics in the UofS-I DPF device by analyzing the signals of the discharge current, the anode voltage, the intensities of the electron and ion beams, and the SXR and HXR emissions,

2. Using a model code (the “Lee model” code [39], discussed in section 2.2) to determine the optimum capacitor bank voltage and the operating pressure for the UofS-I DPF device, and to compute the radial positions and the speeds of the focusing plasma by curve fitting,
3. Measuring the electron temperature of the UofS-I DPF plasma using an array of photodiodes and the double-filter technique, and finally,
4. Correlating the signals with the anode voltage and electron temperature.

1.5 Thesis Outline

An introduction of the plasma, the plasma temperature, fusion in plasmas, and the magnetic pinch are highlighted in this chapter. The remainder of this thesis comprise the following chapters:

- the DPF dynamics and the Lee model in chapter 2,
- the x-ray emission from DPF devices, the PIN photodiodes, and the ratio method in chapter 3,
- the UofS-I DPF device, its design and schematics, the electrical parameter measurements, and the UofS-I DPF device operation and parameters in chapter 4,
- the simulation and experimental results comprising the UofS-I DPF device plasma dynamics, the Lee model simulation, the electron temperature measurements, and the electron temperature correlations in chapter 5, and finally,
- a summary and suggested future work in chapter 6.

Chapter 2

The Dense Plasma Focus

The dense plasma focus (DPF) has always been considered as an alternative magnetic fusion device [8]. It is a plasma gun in a coaxial arrangement that uses pulsed high current electrical discharges for compressing plasmas to achieve high electron densities and electron temperatures.

The plasma focus was discovered independently by Mather [40] and Filippov [41] in the 1960s. Their devices had significantly different aspect ratios. The Mather type is a modification of the coaxial plasma gun operated at a higher fill pressure. It consists of two coaxial electrodes separated by an insulator sleeve, placed in a vacuum chamber. The Filippov machine, on the other hand, was developed as a modification of the Z-pinch to hide the insulator zone from the pinch region and prevent re-strikes caused by radiation from the plasma. Figure 2.1 illustrates the electrode geometries of the two types of DPF plasma devices.

The DPF device became well known as both a source of fusion neutrons and a source of x-rays. Since then, many plasma focus devices have been built, with stored bank energies ranging from 1 kJ to 1 MJ. Early works have shown that the device produces hot and dense plasmas with a lifetime of around 50 ns. Besides being a source of hot dense plasma and fusion neutrons, the plasma focus also emits copious amounts of x-rays especially when operated with high Z (atomic number) gases [24].

A way of optimizing the machine is to choose the dimensions of the electrodes, both length and diameters, and the operational pressure in relation to the characteristics of the energy source. Moreover, the current should be at its maximum when the plasma sheath moves from the base, in the case of Mather DPF, to the top of the inner electrode along

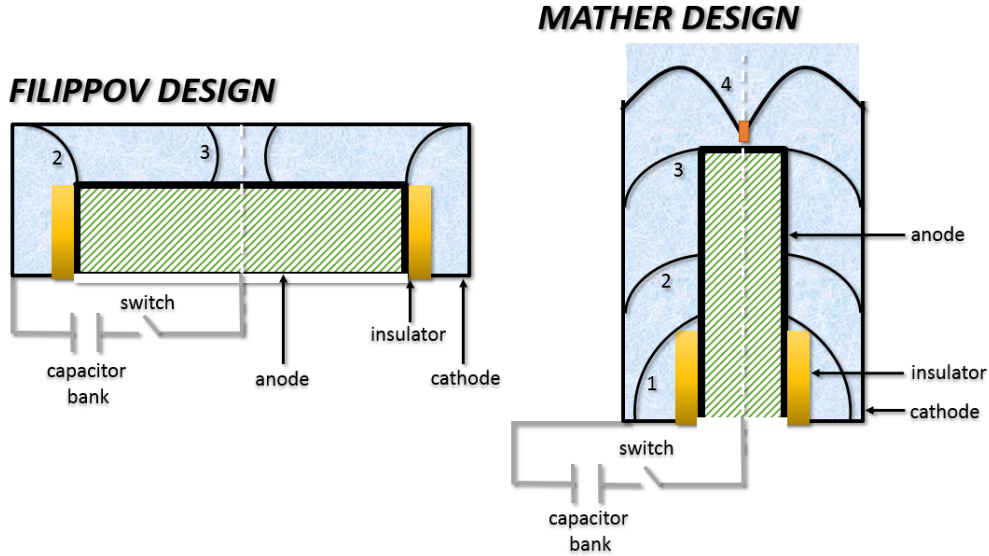


Figure 2.1: The two types of DPF designs: Filippov-type (left) and Mather-type (right). Both are similar in plasma dynamics and components but differ in aspect ratios and geometry. The umbrella-shaped lines indicate the current sheath moving upwards to the top of the electrode and then being compressed radially to form a hot and dense plasma.

the z -axis (axial direction). It is at such instance that a filament of hot and dense plasma is formed in front of the inner electrode and is at its maximum compression. The details of the dynamics in a Mather-type DPF device will be explained in the following subsection.

2.1 DPF Plasma Dynamics

The Mather-type plasma focus consists of two coaxial electrodes separated by an insulator sleeve at the base and placed in a vacuum chamber. These electrodes are immersed in a low-pressure gas, and the electrodes are connected to a capacitor bank through a transmission line typically via a spark gap acting as a fast switch. The efficiency of the energy transfer highly depends on the design of the transmission lines from the capacitor bank to the plasma focus chamber.

The simplified working principle of a DPF device is based on conversion of the stored electrical energy supplied by the capacitor bank into magnetic energy that appears behind the moving current sheath in the chamber. A portion of this energy is converted into plasma

energy during the rapid collapse of the sheath beyond the anode tip.

When voltage is applied between the positive central electrode (anode) and the outer electrode (cathode), the outer surface of the insulator sleeve acquires a positive charge due to polarization. Free electrons present in the surroundings of the insulator sleeve tend to accumulate on its outer surface as it is positively charged. A current sheath is developed as the gas breakdown occurs across the insulator sleeve surface. The current sheath is then detached from the insulator sleeve surface and is accelerated towards the open end of the anode under the influence of its self-generated $\mathbf{J} \times \mathbf{B}$ force. At the end of the anode, current sheath implosion takes place by this force. Consequently, a short-lived plasma with high density and high temperature in the order of several keVs is formed. Finally, the pinch generates beams of ions and electrons in opposite directions, and x-rays.

Generally, the DPF dynamics is divided into three distinct phases: the breakdown phase (Fig. 2.2-1), the axial acceleration phase (or axial rundown phase)(Fig. 2.2-2), and the radial phase (or radial compression phase)(Fig. 2.2-3).

2.1.1 Breakdown Phase

A pulse of high voltage is applied between the electrodes of the DPF while the chamber is filled with working gas under a suitable pressure. As an effect, an azimuthally symmetric electrical discharge will be initiated. This discharge is preceded by an electrical breakdown phase which occurs initially along the insulator tube and expands outwards.

Free charged particles drift towards the surfaces of the electrodes and towards the insulator before the high voltage is applied. Free electrons close to the insulator surface tend to induce a negative potential at the insulator surface due to a dielectric constant of a material and high surface resistivity. Experiments have shown that a time delay of some tens of nanoseconds exists before the breakdown along the insulator surface upon applying a high voltage between the electrodes [40].

More electrons are created by field emission and ionization of the gas after applying a

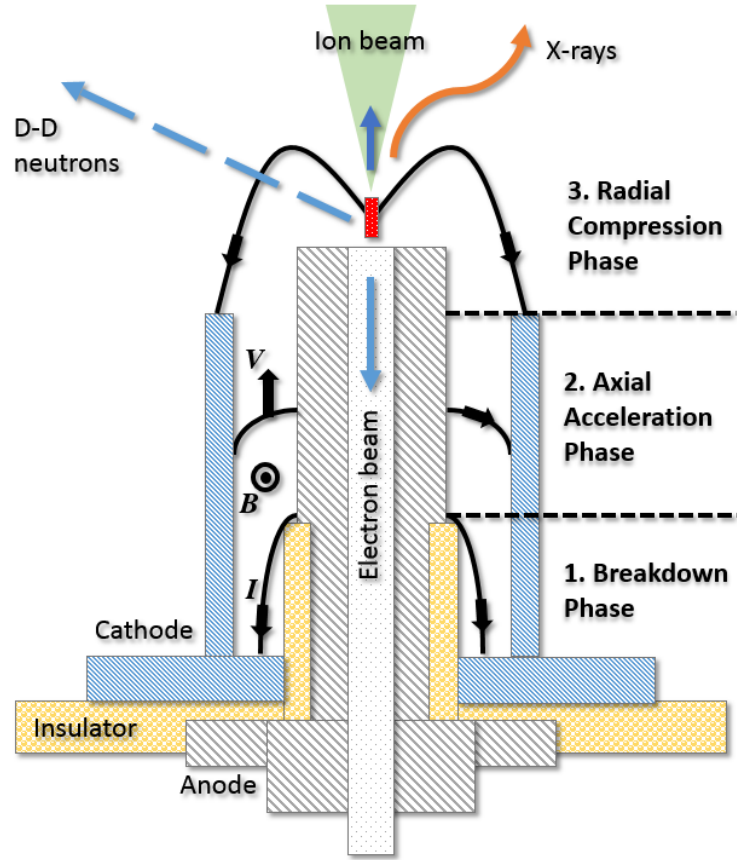


Figure 2.2: Plasma focus dynamics: break-down, acceleration, and radial compression phases; radiation and neutron emission, and the electron and ion beam emissions from the focusing region.

high voltage between the electrodes. These electrons are then accelerated along the electric field lines, radially directed towards the inner electrode and the insulator. As the discharge progresses, the electric field stays at the front of the discharge. This effect helps with the ionization at the front along the insulator, until the sliding discharge reaches the end of the insulator, connecting both the electrodes. It is due to the $\mathbf{J} \times \mathbf{B}$ force that the current is lifted off in an inverse pinch process. The conductance of the sliding discharge gets sufficiently high after several hundred nanoseconds, and converts into a plasma sheath, with a double-layer structure that consists of the ionization front and the magnetic piston [11].

During the break down phase, the direction of the current is primarily downwards, and the magnetic field induced due to the upward current in along the anode is in the counter-

clockwise direction when viewed from the top, causing the magnetic force, $\mathbf{J} \times \mathbf{B}$, directed radially outwards. The $\mathbf{J} \times \mathbf{B}$, due to small radially outward current in the plasma, moves the plasma upwards. Once the breakdown has completed, the current fans out and flows axis-symmetrically from the anode to the cathode within a time of around 100 - 300 ns [11]. The current sheath then lifts off, setting the stage for the axial rundown phase.

2.1.2 Axial Rundown Phase

The next stage is known as the axial acceleration or the axial rundown phase. This phase describes the propagation of the magnetically-driven plasma sheath along the z direction towards the end of the electrodes. This phase is mainly important in the formation of the hot, dense plasma pinch such that the current sheath preferably arrives at the axis coincident to or close to the initial maximum of the discharge current. This phase is also responsible for the plasma sheath structure having certain properties to ensure a strong focusing. These properties include the requirements of axial symmetry, smooth profiles, and a thin, uniform current sheath structure.

Since the amplitudes of the discharge current are sufficiently large and the pressure values of the operating gas are sufficiently low, the sheath pushed by the $\mathbf{J} \times \mathbf{B}$ force moves against the stationary gas from the beginning at supersonic speeds. The moving structure induces a gas-dynamic shock due to the small mean-free-paths of the ion-atom charge exchange and elastic collisions. These collisions heat and compress the neutral gas in front. As a result, the sheath has a complex structure that comprises a compressed and hot layer in front, followed by an ionizing region, then a hot plasma region carrying current at its trail, and an almost vacuum magnetic field region. The structure of the sheath is determined by the pattern of the current that drives it, that is, if the pattern is uniform enough, the plasma will also be uniform, and an azimuthal filamented pattern of the sheath will be produced [11].

Typical experiments use magnetic probes [42], optical and spectroscopic diagnostics [21], interferometric arrangements [43], and image converter cameras [44] to study this phase.

Large fractions of up to 50 percent of the current going into the device flow behind the sheath as per experiments [11]. It has also been found that the thickness of the plasma sheath structure ranges from 2 to 3 cm, and the axial sheath velocities range in orders of cm/ μ s [10]. Since the magnetic field is inversely proportional to r (radial position) within the inter-electrode region, the current sheath profiles are curved. While maintaining the axisymmetric property of the current sheath, a parabolic shape is acquired with a thinner sheath in the region close to the central electrode.

The plasma sheath will eventually arrive at the tip of the electrodes. The inner edge of the current sheath sweeps radially around the end of the anode at the end of this phase. The outer end of the sheath continually moves along the z -axis, sweeping along with it the greater portion of the plasma.

2.1.3 Radial-Compression Phase

The current sheath radially sweeps around the end of the anode by the radial inward $\mathbf{J} \times \mathbf{B}$ force. The plasma then forms a column extended in the axial direction and finally collapses in the way similar to the Z-pinch discussed earlier in Chapter 1. This period occurs within about 200 ns depending on the DPF characteristics [10, 11]. This phase plays the most important role in the plasma focus evolution because this leads to the compression and final formation of the hot and dense plasma column.

This compressed and heated plasma leads to the emission of intense radiation, high-energy particles, and copious amounts of nuclear fusion products such as neutrons when deuterium gas is used. Furthermore, this phase could be divided into four sub-phases namely: the compression phase, the quiescent phase, the unstable phase, and the decay phase.

2.1.3.1 Compression Phase

This phase begins with the sweeping of the current sheath around the end of the inner electrode. The sheath then collapses radially with azimuthal symmetry, funnel-shaped pro-

file. The sharp voltage spike (Fig. 2.3) and the current dip are typical features of compression where the large increase of the plasma column impedance (inductance and resistance) has occurred [11].

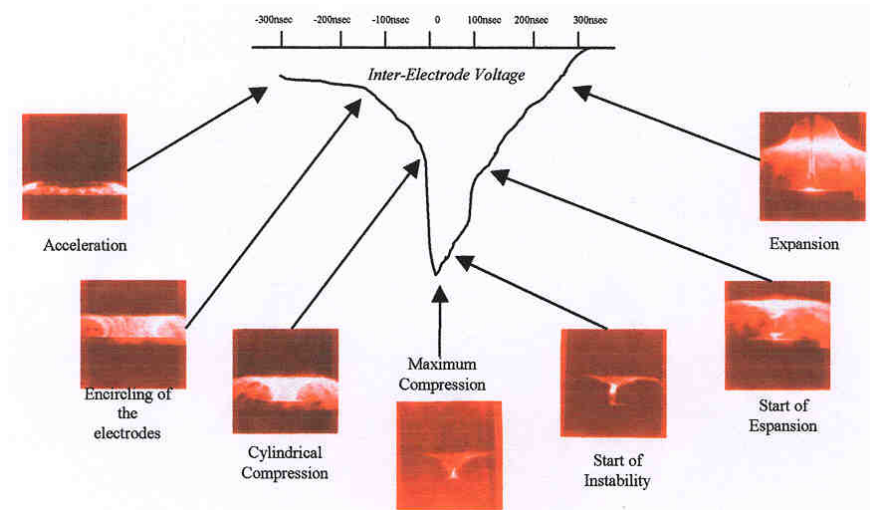


Figure 2.3: Plasma compression-voltage comparison chart showing the time evolution of the sheath with respect to the voltage, and that the peak of the anode voltage corresponds to the maximum compression of the plasma sheath [16].

Shock heating [45] is the main mechanism inside the plasma before the front of the current sheath arrives at the z -axis. Hence, the electrons with temperatures up to 1 eV, depending on the speed of the gas, are cold compared to the ions whose temperatures range up to 300 eV. *Joule heating* [17, 45] becomes the main mechanism after the transformation of the plasma structure into a plasma column. This column will be adiabatically compressed due to the pinch effect.

In the implosion phase, the energy is mainly transferred to the ions due their larger mass compared to the electron mass. Anomalous electron heating may occur as well [17].

The magnetic field diffuses into the plasma column towards the end of this phase. It will be completely diffused almost instantaneously, leading to an *anomalous plasma resistance* [17]. The final electron temperature will typically be 1 - 2 keV in this phase, and maximum values of electron density and electron-ion temperatures have been estimated by using spectroscopy [22], interferometry [43], and laser scattering [46].

2.1.3.2 Quiescent Phase

This phase is the beginning of the expansion of the pinch plasma column. This occurs radially and axially and hinders the rate of radial expansion by the confining magnetic pressure. The “fountain-like” geometry of the current sheath causes the rate of axial expansion being hindered, resulting in a formation of an *axial shock front* [11].

An electric field is induced in the plasma column due to the sharp change in plasma inductance starting from the compression phase. This field will cause the acceleration of the ions and the electrons in opposite directions. The drift velocity between the electrons and the ions will approach the increasing electron thermal velocity, which is the condition for the micro-instabilities like the *electron cyclotron* [47] and other forms of beam-plasma instability.

The $m = 0$ instability [48] is developed at the end of the quiescent phase due to the increasing electron temperature. The plasma column will then be further compressed locally due to the $m = 0$ instabilities.

2.1.3.3 Unstable Phase

This phase is responsible for the evolution of phenomena such as the soft and hard x-ray emission, fast ions and electrons, and the neutron products from the D-D reaction using a deuterium operating gas. Electrons are accelerated towards the inner electrode and the ions in the opposite direction due to the induced electric field. Here, the plasma density increases up to 10^{19} cm^{-3} [11].

Due to the bombardment of accelerated runaway electrons on the anode, copious amounts of impurities are injected into the plasma column. At the same time, x-ray is radiated due to electrons impinging on the copper surface. Sequentially, the explosion continues along the plasma column. This disruption goes on until the whole column has been completely broken up, and consequently the plasma density drops. Micro-instabilities give rise to strong

plasma heating. Due to the measured Bremsstrahlung radiation being sufficiently large, the electron temperature reaches up to 4 - 5 keV [4, 29–31].

2.1.3.4 Decay Phase

This is the last phase of the radial collapse and the plasma focus dynamics. A hot and thin plasma cloud is formed due to the complete breaking up of the plasma column. This plasma cloud emits a large amount of Bremsstrahlung radiation. The soft x-ray emission rises sharply during the pinch decay. Moreover, it reaches the first peak shortly after the pinch break-up and continues at a high level for over 300 ns [11]. The neutron pulse reaches its peak in this phase, which has been initiated from the unstable phase.

2.2 The Lee Model

In 1984, a plasma focus program led by a DPF scientist, S. Lee, developed a 2-phase model that is continually developing to its present form. They called it the “Lee model” code [11]. The code includes thermodynamic data such that it simulates in various operating gases. These operating gases include hydrogen, deuterium, deuterium-tritium, nitrogen, oxygen, helium, neon, argon, krypton, and xenon. It can also simulate a wide range of DPF devices including the PF-4000 developed in Chile, the UNU/ICTP PFF by networking countries, the NX-2 in Singapore, the DPF798 and Poseidon in Germany, and the PF1000 in Poland [39].

The Lee model aims to cover the process of the plasma sheath wholly: from the breakdown to axial, to the radial, up to the post-focus phase. Thus, the Lee code is useful for materials deposition and damage simulation. It also prioritizes utility in a way that the energies, masses, and charges are consistent and connected to the total process of experiments and is based on experimental results.

The Lee model allows a simulation of a Mather-type plasma focus by inputting machine

parameters. These parameters include the inductance and capacitance of the capacitor bank, the charging voltage, and the electrodes' length and radii, to name a few.

2.2.1 Model Equations

Some important equations used to implement the code are briefly presented in this section, and a thorough derivation may be found on the UPFLF site [39]. Thus, this section is simply an adaptation to S. Lee's review of the Lee model code [49].

The axial phase is described using coupled equations: the equation of motion and a circuit equation. The equation of motion describes the axial phase parameters. It denotes the mass and current factors, f_m and f_c , respectively. The mass factor, f_m , is responsible for the current sheath's porosity (the moving current sheath shock frontal structure inclination, the effects of the boundary layers, and other effects affecting the total mass in the axial phase). The current factor, f_c , is responsible for the current fraction through the moving plasma sheath.

Figure 2.4 shows the electrodes' configuration used for the Lee model code. The electrodes' radii are a and b for the inner and outer electrodes, respectively. The axial position of the current sheath is denoted as z , referenced to the base of the electrodes that are located at $z = 0$.

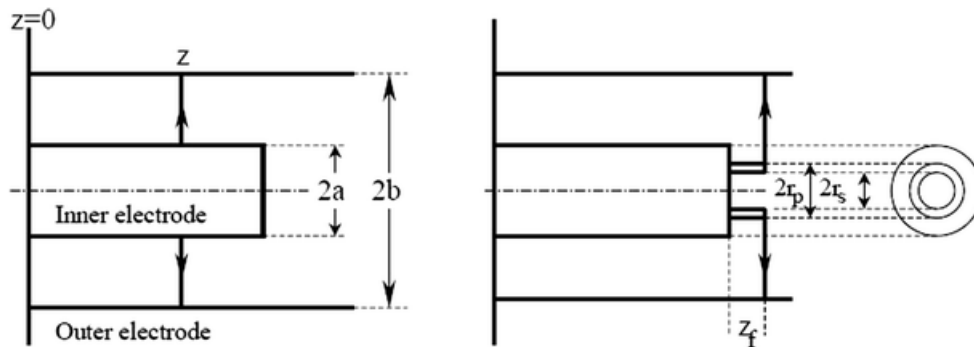


Figure 2.4: The DPF electrodes' configuration and dimensions and plasma dimensions used in the Lee code in the axial (left) and radial (right) phases [11].

In the radial phase, the plasma sheath curls into the inner electrode as it reaches the tip of the electrodes. The dimensions of the plasma in the radial phase are also defined in Fig. 2.4 (right): the inner and outer radii of the plasma at the tip of the electrodes are r_s and r_p , respectively, and the length of the plasma from the tip of the inner electrode is z_f .

The mass brought up by the sheath at the z -axis is given by

$$m_0 = \rho_0 \pi (b^2 - a^2) z \quad (2.1)$$

where ρ_0 is the density of the operating gas.

Since there is the mass loss effect with a constant mass factor, $f_m < 1$, we get the mass carried by the sheath at the z -axis to

$$m_0 = \rho_0 \pi (b^2 - a^2) z \cdot f_m \quad (2.2)$$

At position z of the current sheath, the momentum equation is

$$\frac{d(m_0 v)}{dt} = \frac{d}{dt} \left[\rho_0 \pi (b^2 - a^2) z \cdot f_m \frac{dz}{dt} \right] = \rho_0 \pi (c^2 - 1) a^2 f_m \frac{d}{dt} \left(z \frac{dz}{dt} \right) \quad (2.3)$$

where v is the current sheath velocity, and $c = b/a$. The magnetic force on the current sheath is given by

$$F_B = \int_a^b \left[\left(\frac{\mu_0 I f_c}{2\pi r} \right)^2 / (2\mu_0) \right] \cdot 2\pi r dr = \frac{\mu_0 f_c^2}{4\pi} \ln(c) I^2 \quad (2.4)$$

where r is the plasma radial position, μ_0 is the permeability of free space constant, f_c is the current factor, and I is the discharge current.

Combining equations (2.3) and (2.4), the equation of motion becomes

$$\frac{d^2 z}{dt^2} = \left[\frac{f_c^2}{f_m} \frac{\mu_0 (\ln c)}{4\pi^2 \rho_0 (c^2 - 1)} \left(\frac{I}{a} \right)^2 - \left(\frac{dz}{dt} \right)^2 \right] \cdot z^{-1} \quad (2.5)$$

The DPF circuit used for the Lee code is shown in Fig. 2.5. The parameters of the electrical circuit are defined as follows: r_0 is the circuit stray resistance, L_0 is the external circuit inductance, C_0 is the energy stored capacitance, L_p is the plasma inductance in the DPF, and r_p is the plasma resistance in the DPF.

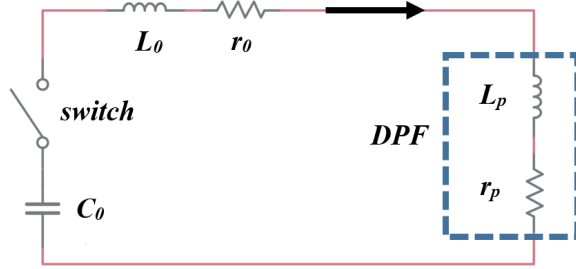


Figure 2.5: The DPF circuit diagram used in the Lee code.

The circuit equation approximation according to Kirchhoff's second law for the circuit in Fig. 2.5 can be written as

$$\frac{1}{C_0} \int I dt - V_0 + r_0 I + \frac{d}{dt}(L_0 I) + r_p I_p + \frac{d}{dt}(L_p I_p) = 0 \quad (2.6)$$

where one can obtain the general circuit equation:

$$\frac{dI}{dt} = \left[V_0 - \frac{\int I dt}{C_0} - r_0 I - I f_c \frac{\mu_0}{2\pi} (\ln c) \frac{dz}{dt} \right] / \left[L_0 + \frac{f_c \mu_0}{2\pi} (\ln c) z \right] \quad (2.7)$$

Equations (2.5) and (2.7) form coupled equations system with two unknown variables, I and z . The equation of motion is greatly affected by the electric current, I . On the other hand, the circuit equation is affected by the motion of the current sheath dz/dt and the position z .

The equations for the compression phase are similarly derived and can be found in [49].

Chapter 3

X-ray Emission from DPF

The dense plasma focus has originally been intended as a fusion device. Yet over the years, the x-ray emission from the plasma focus was studied with the aim of finding production mechanisms. Soft x-rays are concerned mainly with the effect of impurities (coming from the electrodes or in the working gas) on the overall device performance when using deuterium and heavier gases (such as helium and neon) [12]. The DPF's potential as an intense soft x-ray source has been the motivation of intensive studies over the last couple of decades. The high energy density of the hot-spots, as well as radiative collapse, have been the subjects of studies in heavy gases. The problem tackles the process of increasing the total x-ray yield in certain spectrum ranges [19].

In the plasma, the main processes that emit x-rays are the Bremsstrahlung, the recombination, and the de-excitation. The first two processes give rise to the continuum of the x-ray spectrum, while the third process produces the line radiation of the plasma.

The continuum spectrum mainly includes Bremsstrahlung (Fig. 3.1) coming from the Coulomb interactions between electrons and ions in the plasma, and the solid material such as the anode. Incoming electrons at high speeds get decelerated (or retarded) as they approach atoms in solid material. Electrons also interact with the ions in the plasma and the attracting force decelerates and bends its trajectory. During this process, Bremsstrahlung radiation is resulted.

For the plasma at a given temperature $T(\text{eV})$, the peak of its continuum (Bremsstrahlung) occurs at the wavelength of [50]

$$\lambda = \frac{6200}{T(\text{eV})} \text{\AA} \quad (3.1)$$

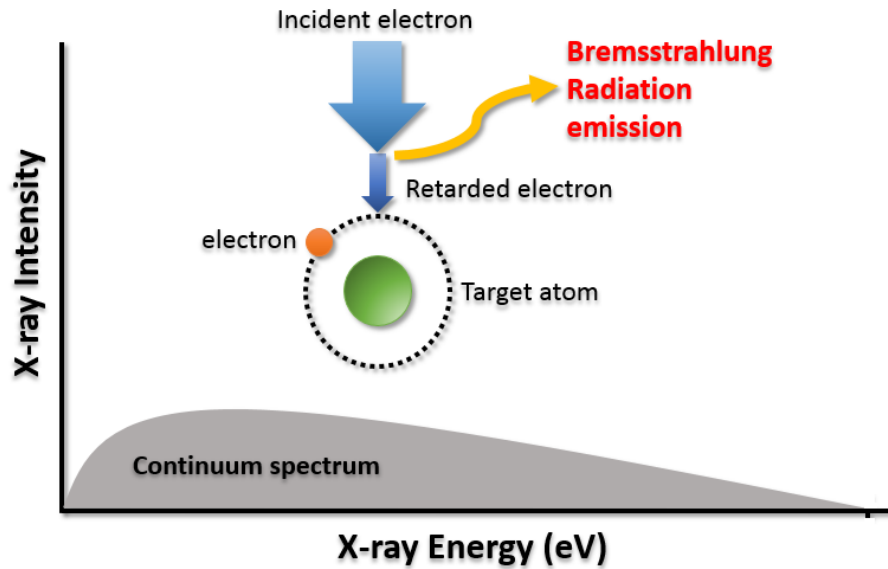


Figure 3.1: The model of the production of Bremsstrahlung x-rays producing a continuum spectrum of radiation caused by the retardation of the incident electron approaching a target atom.

Hence, for a plasma at $T = 1$ keV, the x-ray continuum is predictable to peak at $\lambda = 6.2 \text{ \AA}$, which is in the soft x-ray region.

The continuum radiation also includes recombination radiation that is emitted by an initially-free electron as it loses energy on recombination with an ion.

However, if an already-bound electron loses energy by falling into a lower ionic energy state, then line emission with a characteristic energy is obtained (Fig. 3.2). In this case, the accelerated electrons bombard and eject electrons from the inner shells of the atom. These vacancies will then be immediately filled by electrons from a higher orbital level (losing their energy) to a lower orbital level of the atom. The energy loss is converted to the emission of x-rays. These x-rays are sharply defined and are called “characteristic x-rays”. They are also associated with the energy levels of the target atoms.

X-rays produced from electron transitions from the second orbital state (L-shell) to the ground state (K-shell) are called “ $K\alpha$ x-rays”, and those from the third orbital state (M-shell)

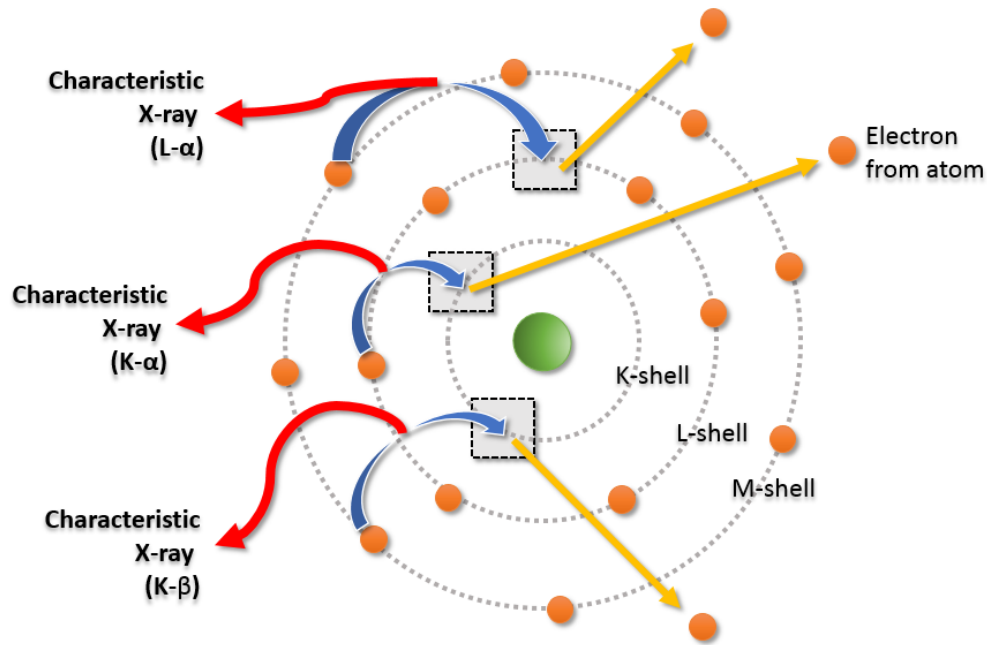


Figure 3.2: The model of the characteristic line radiation x-ray emission: electrons (in orange) orbiting the nucleus (in green) at different orbital states (or shells). EM radiation in the x-ray energy range are emitted due to energy loss due to electron transitions from a higher to a lower orbital state.

to the ground state are called “ $K\beta$ x-rays”.

The relative strengths of the continuum and line emissions depend on how the plasma was formed. Typically, for a plasma formed from a high- Z material, continuum emission dominates, while for a low- Z material, the line emission can be stronger. The superposition of both continuum and line radiation of x-rays is presented in Fig. 3.3.

The energy source for the heating mechanisms is the electromagnetic energy stored in the surrounding magnetic field after being transferred from the capacitor bank. In cases of just pure Bremsstrahlung emission, the effect of radiation cooling on the dynamics of the plasma compression and confinement can be neglected. Using medium Z -gases such as argon and neon, the intensity of electromagnetic radiation would be of the order of a few percent of the total energy of the capacitor bank [11]. At such high levels of energy losses, the radiation has a strong effect on the plasma dynamics.

Other than making the plasma focus an intense x-ray source which is useful in many

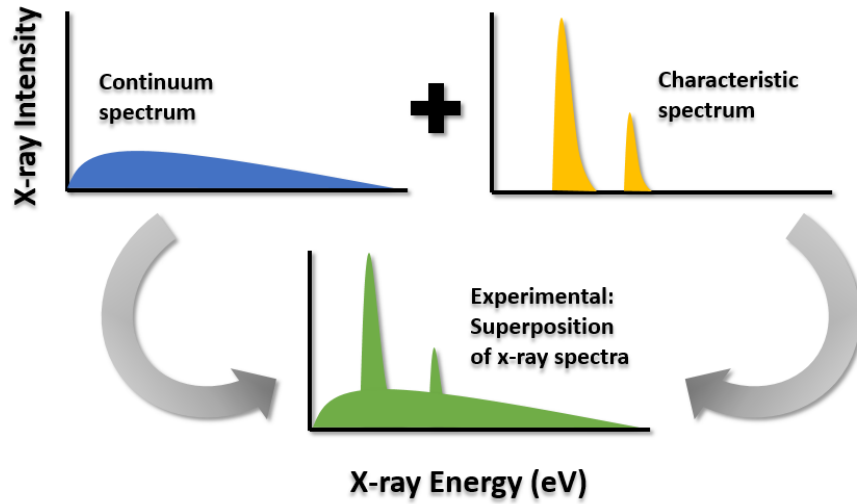


Figure 3.3: The expected experimental spectrum (in green) of the superposition of both continuum (in blue) and line/characteristic (in yellow) x-ray spectra.

applications such as micro-lithography [34–36] and x-ray microscopy [37], the x-ray emitted also provides a suitable means of studying the plasma properties. In high temperatures, almost all of the electrons in the plasma are fully stripped off, and very little visible light is emitted from the hot part of the plasma. The electrons do, however, give off continuum radiation when they pass close to the ions.

The experimental measurement of continuum and line radiations from hot plasmas can be performed using detectors such as a Photo-Conducting Diamond (PCD) [34] or BPX-65 PIN photodiodes [51]. These detectors are sensitive to incoming photons within the x-ray energy range.

3.1 Silicon-PIN Photodiodes

The BPX-65 PIN photodiodes, typically made of a silicon-type layer, can be used for measuring soft x-rays. These silicon PIN diodes are convenient x-ray detectors as they are sensitive with a fast response time. They have a desired flat energy response between 1 Å and 20 Å [52].

A PIN diode is very similar to a PN-junction diode except that it has a large intrinsic layer between the P- and the N-type layers. This intrinsic layer is depleted completely and will absorb the x-ray photon, forming an electron-hole pair. The PIN diode structure is schematically shown in Fig. 3.4, where a reverse-biased voltage is applied across the diode.

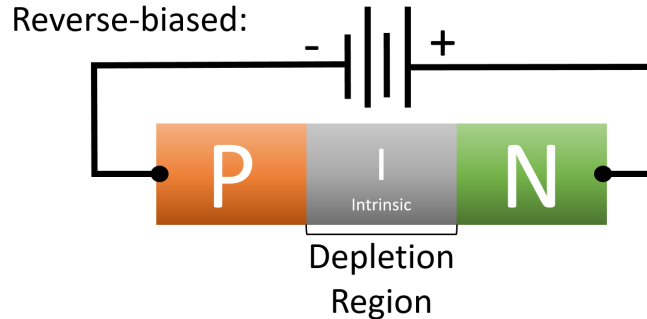


Figure 3.4: PIN diode schematic in reverse-bias with a large intrinsic layer (the depletion region) in between the P- and N- type layers.

The electron-hole pairs are produced when the x-ray photons are absorbed by the diode, having a response of 1 electron-hole pair produced with each 3.55 eV of photon energy being absorbed. Thus, an electron charge of 0.28 C will be produced for each Joule of x-ray energy being absorbed [52].

The electron-hole pairs are separated due to the applied potential. The electrons are swept to the N-type layer, while the holes to the opposite side, which is the P-type layer. The electron-hole pairs that form in the P-type and N-type regions recombine.

Figure 3.5 shows the PIN photodiode layers and the formation of electron-hole pairs from the absorbed SXR.

To calculate the sensitivity of the diode to x-ray photons, the x-ray absorption at the N-type entrance (that acts as a filter) must be considered. The electron-hole pair formation will correspond to the amount of photons absorbed by the intrinsic layer, thus, the sensitivity $S(\lambda)$ is given by [52]

$$S(\lambda) = (0.28) \cdot e^{-\mu_s x_1} (1 - e^{-\mu_s x_2}) \frac{\text{C}}{\text{J}} \quad (3.2)$$

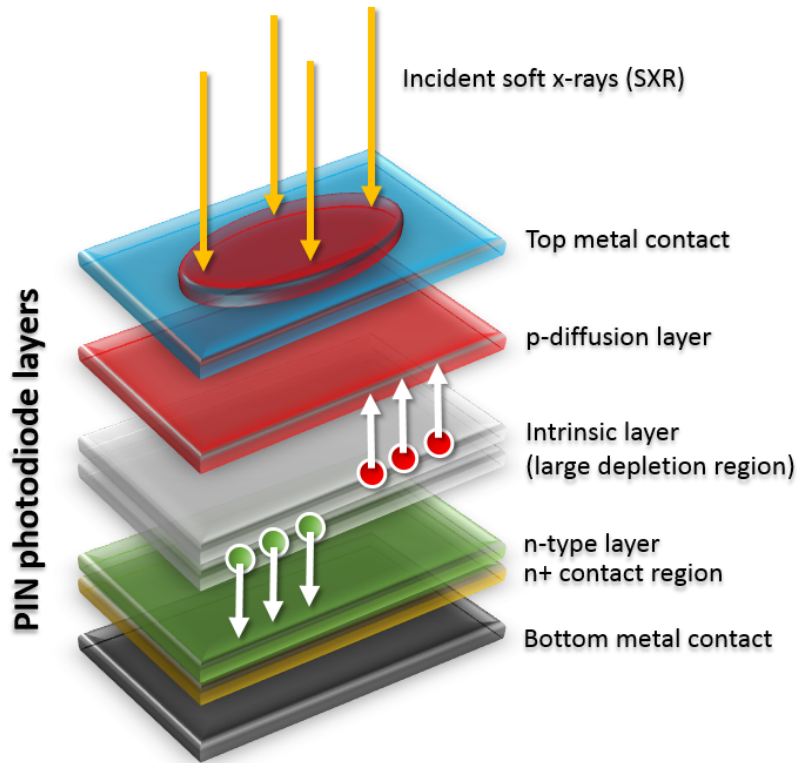


Figure 3.5: PIN diode cross-section with photon absorption and electron-hole pair dynamics. Electron-hole pairs are formed in the intrinsic layer from the photons absorbed through the p-type layer. Electrons (green circles) are swept to the n-type layer and the holes (red circles) into the p-type layer due to the applied potential.

where 0.28 is the electron charge per Joule of x-ray energy absorbed, μ_s is the mass absorption coefficient of the silicon material, and x_1, x_2 are the mass thicknesses of the N-type entrance window and the intrinsic layers, respectively.

At a short wavelength (high photon energy) region, the x-ray photons may pass through the intrinsic layer without being absorbed, hence, the sensitivity is expected to drop. On the other hand, at long wavelength (low photon energy) regions, the x-ray photons will be absorbed by the silicon entrance layer, causing the sensitivity to drop drastically. Thus, the region between these limits has a sensitivity of the Si-diode to be somewhat flat, except at the K-absorption edge of the Si material at 1.840 keV (6.73 Å) [52].

A typical BPX-65 reverse-biased circuit is shown in Fig. 3.6.

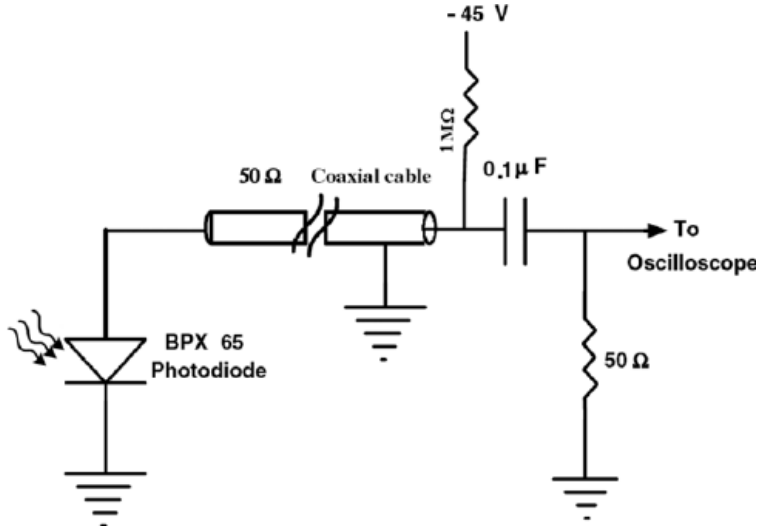


Figure 3.6: Typical BPX-65 reverse-biased circuit diagram [32].

3.2 Ratio Method on SXR

An electron temperature measurement can be done based on two main methods, namely: Bremsstrahlung and line radiations [4], and Thomson scattering [52]. Other than these methods, some diagnostic methods, such as Langmuir probes [52], can also be used to measure local plasma properties such as plasma temperature and plasma density in low temperature and long lifetime plasmas.

The intensities of spectral lines is related to the electron temperature with the consideration of detailed atomic processes. A method of ratios can be applied based on the relative intensities of Bremsstrahlung SXRs [30]. Such method is called the “ratio method” [30–33].

There are two different ratio methods: one is based on the spectroscopic method on resolved line emissions [30], and the other one is based on the spectrum integrated intensity [33].

A brief theory of the spectroscopic method is the following (a detailed derivation can be found in [30]): When one excitation process from ground state by electron collision takes place, followed by a photon emission, the population n_a of level a relative to the population

n_1 of the ground level is given by [30]

$$\frac{n_a}{n_1} = n_e \frac{S_{1a}}{A_a} \quad (3.3)$$

where n_e is the electron density, A_a is the transition probability, and S_{1a} is the electron collisional excitation function for electron temperature.

It can be observed that the intensities of the spectral lines are proportional to the collisional excitation function at different levels. The ratios of the line intensities of the same ion are only dependent on the atomic constants and the electron temperature.

Assuming a Maxwellian velocity distribution for free electrons, the ratio of intensities becomes [30]

$$\frac{I_{1a}}{I_{1b}} = \frac{f_{1a}\chi_{1b}g(\chi_{1a}/kT_e)}{f_{1b}\chi_{1a}g(\chi_{1b}/kT_e)} \exp\left(\frac{\chi_{1b} - \chi_{1a}}{kT_e}\right) \quad (3.4)$$

where the subscripts, $1a$ and $1b$, are the two different line intensities, f is the absorption strength, χ is the excitation potential, g is the Kramers-Gaunt factor [30], and kT_e is the electron temperature. This equation can be used to calculate the intensity ratios against kT_e .

The second method is a more direct approach of calculating the ratio of intensities. The total emitted spectrum from the plasma can be determined using the formula [33]

$$I_p = \int_{all \lambda} P(\lambda, T_e) d\lambda \quad (3.5)$$

where $P(\lambda, T_e)$ ($\text{Wcm}^{-3} \text{ \AA}^{-1}$) is the x-ray intensity from a plasma source, and λ is the wavelength of the photon.

The intensity that is actually detected by the PIN diode considering the absorption with the foil between the source and the detector and the solid angle (point-source approximation) can be written as

$$I_p = \int_{all \lambda} P(\lambda, T_e) d\lambda \cdot S(\lambda) \cdot e^{-\mu x} \quad (3.6)$$

where $S(\lambda)$ is the BPX-65 sensitivity, μ is the mass absorption coefficient of the material, and x is the absorption foil thickness.

Given two emitted spectra through different foil filter thicknesses, one can obtain the ratio of the generated spectrum of these two combinations from the same x-ray pulse (using Mylar and aluminum filters, for example):

$$R = \frac{I}{I_0} = \frac{\int_{all \ \lambda} P(\lambda, T_e) d\lambda \cdot S(\lambda) \cdot e^{-[\mu_{mylar}(\lambda)x_{mylar} + \mu_{Al}(\lambda)x_{Al}]}}{\int_{all \ \lambda} P(\lambda, T_e) \cdot S(\lambda) \cdot e^{-\mu_{mylar}(\lambda)x_{mylar}} d\lambda} \quad (3.7)$$

This can be computed for a fixed T_e , and repeated for a range of temperatures. Based on this, a calibration curve can be plotted for the electron temperature measurement by x-ray ratio method. Evidently, at least two signals of PIN diodes are required for this method. This method is called the “double-filter technique”, and is adopted in this research.

Bremsstrahlung radiation is used for $P(\lambda, T_e)$ in the model for this research. Thus, one is mainly concerned in measuring only the continuum radiation coming from the interaction of electrons and atoms of the operating gas. However, electrons also bombard the copper electrodes in the DPF, consequently emitting copper line radiations. These lines will introduce errors in the data interpretation. A way of minimizing the error due to impurity line radiations is by selecting a particular filter material and thickness. This filter must discriminate the transmission in the energy range of the line radiation.

Chapter 4

The UofS-I Dense Plasma Focus Device

The experiments in this research have been carried out in a low-energy Mather-type plasma focus device powered by a capacitor bank of $5 \mu\text{F}$. The capacitor bank is typically charged to 20 kV. The DPF is operated with argon gas at an optimized pressure of 100 - 200 mTorr.

Figure 4.1 shows a picture of the UofS-I DPF device at the UofS Plasma Physics Laboratory (PPL).



Figure 4.1: The UofS-I dense plasma focus device. A control panel is situated beside the DPF device, and a Faraday cage built by means of copper mesh encloses the signals measurement devices.

Furthermore, an image of the assembly of the electrodes inside the vacuum chamber can

be seen in Fig. 4.2.



Figure 4.2: Electrodes in vacuum: a hollow copper anode nested in 12 concentric cathode rods, and a quartz-infused glass insulator separating the electrodes.

The vacuum system used for the device is a two-stage rotary pump which provides a minimum chamber pressure of 10^{-3} mbar. The power supply is capable of providing up to 30 kV of charging voltage. The capacitor bank is connected to the DPF anode through a pressurized spark gap. The spark gap acts as a switch between the capacitor bank and the DPF anode. It works in a single-discharge mode and is triggered by a fiber-optic pulse signal. A pressure sensor is attached on top of the device and measures the pressure inside the chamber in units of Torr. Several 4-channel digital oscilloscopes (Tektronix TDS 2024c) were used to digitize and record experimental signals. The grounded Faraday cage was built using two layers of copper mesh as walls to minimize electromagnetic noise from the DPF discharge.

4.1 Design Consideration

The main criteria for the design of a plasma focus system can be analyzed based on the dynamic model for the axial acceleration phase. Specifically, it is to match the rise time of the discharge current, t_r , to the time of the arrival of the current sheath at the tip of the inner electrode, t_z . This is also the time when the end of the axial acceleration takes place.

The rise time of the discharge current is taken to be the quarter period of time of the discharge, and is given by [50]

$$t_r = \frac{1}{4} 2\pi \sqrt{L_0 C} \quad (4.1)$$

where L_0 is the static inductance and C is the capacitance of the capacitor bank.

The time it takes for the current sheath to arrive at the tip of the inner electrode is given by [50]

$$t_z = 2 \sqrt{\frac{4\pi^2 (b^2 - a^2) \rho_0 z_0^2}{\mu_0 (\ln \frac{b}{a}) I_0^2}} \quad (4.2)$$

where a and b are the anode and cathode radii, respectively, ρ_0 is the operating gas density, z_0 is the anode length, I_0 is the current, and μ_0 is the permittivity constant.

By matching these two characteristic times (equations (4.1) and (4.2)) one gets

$$\frac{64 (b^2 - a^2) z_0^2}{\mu_0 (\ln \frac{b}{a})} \frac{\rho_0}{C^2 V_0^2} = 1 \quad (4.3)$$

Another matching condition can be derived using the dynamic time and by assuming that a characteristic speed of the current sheath necessary to heat the plasma is around 10 cm/ μ s. This condition is given by [50]

$$z_0(\text{cm}) = \frac{\pi}{4} \cdot 10^7 \sqrt{L_0 C} \quad (4.4)$$

Thus, one can estimate z_0 with a fixed capacitance value and an estimate of the inductance of the capacitor bank. Furthermore, by fixing C , z_0 , ρ_0 , and V_0 , one can find the relation between a and b using equation (4.3).

The Lee model also provides a rule-of-thumb procedure in the design of a plasma focus. Given initial parameters of the capacitance, inductance, and the maximum operating voltage, several properties are suggested. This includes: the undamped peak current, $I = V \sqrt{C/L}$, the central electrode radius, $a(\text{cm}) = (I/250)$ kA using a max undamped current per cm, and the outer electrode radius $b = 2a$ [39].

4.2 Device Schematic, Circuit, and Controls

Figure 4.3 shows the schematic diagram of the UofS-I DPF device when viewed from the base. The PIN diode array is located 30 cm away perpendicular to the plasma sheath trajectory and is facing directly to the pinch position. The pinch position is about 1 cm away from the tip of the anode in the z -direction, and is where the soft x-rays are emitted. The Faraday cup is situated around 35 cm away from the pinch position.

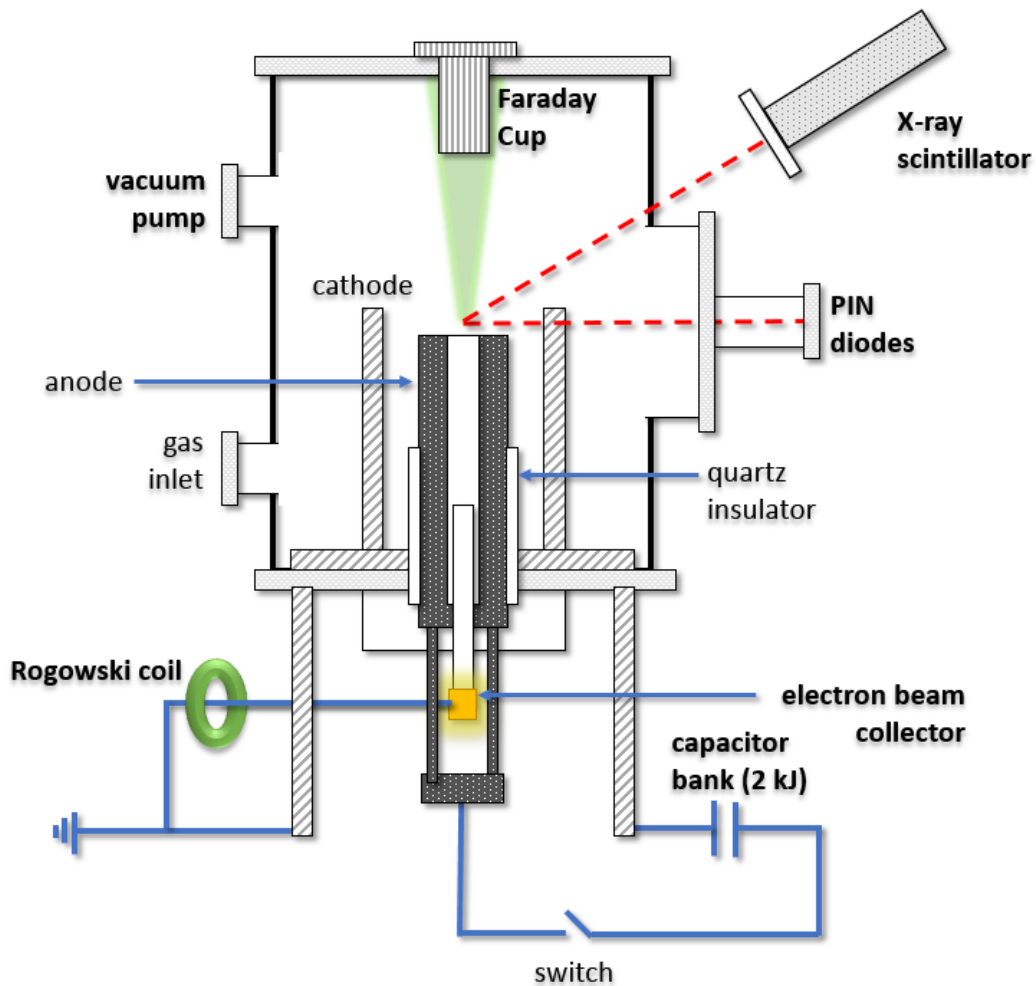


Figure 4.3: The UofS-I DPF device schematic of the major components and detectors with respect to the pinch position. The gas inlet and outlet are situated on the same side. X-ray detectors point directly to the pinch position, while the charged particles detectors are placed in opposite directions in the z -axis. A Rogowski coil measures the current through the grounded wire connected to the electron beam collector, and a Faraday cup is placed inside the chamber opposite the electron beam collector.

Furthermore, Fig. 4.4 shows the cross-section of the chamber and shows the assembly of the electrodes with respect to each other. The central electrode, the anode, is a conventional cylindrical, high conductivity hollow copper rod with a radius of 15 mm. Twelve copper rods, which act as the cathode, are placed symmetrically and concentrically around the anode with a radius of 50 mm and are screwed onto a copper cathode base plate. A 30 mm in length (from the base plate) of quartz-infused glass insulator sleeve is used to separate the anode from the cathode at the base. The entire anode-cathode assembly is placed inside a stainless-steel vacuum chamber.

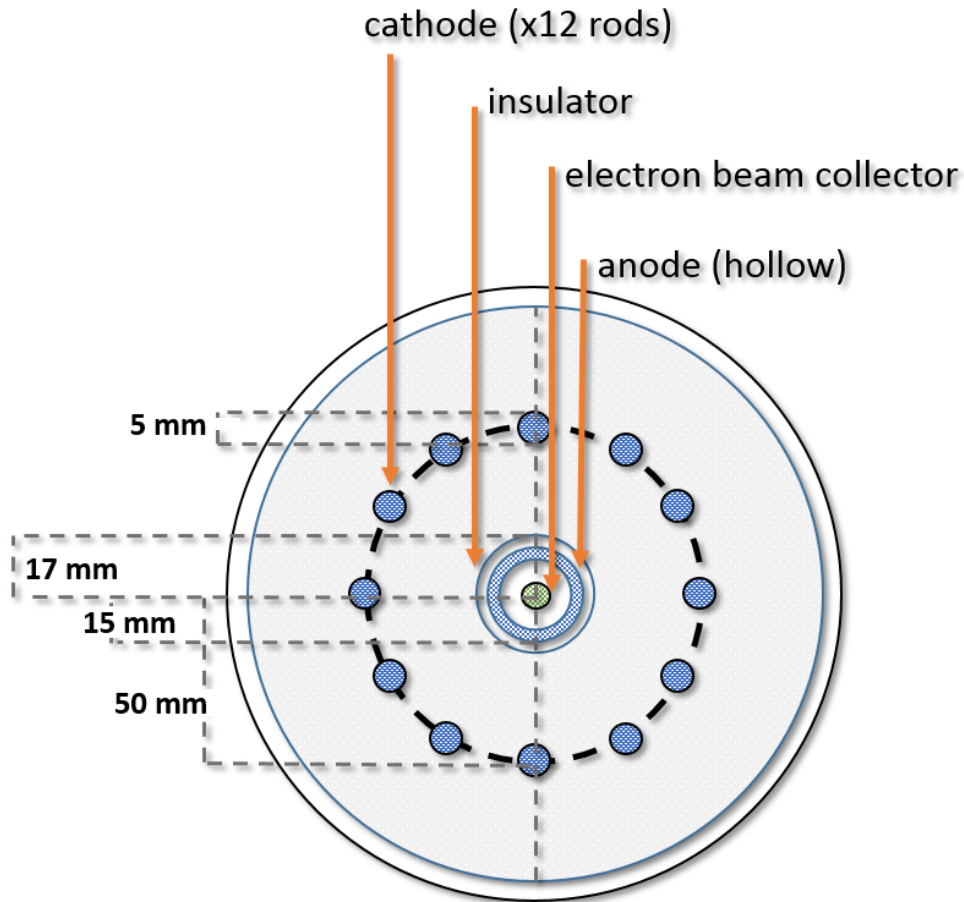


Figure 4.4: A cross-section of the UofS-I DPF showing the electrodes' assembly and dimensions enclosed in the vacuum chamber. Twelve copper rods act as the cathode which concentrically nests the copper anode inside, both separated by a quartz-infused glass insulator. The electron beam collector is situated concentrically inside the electrodes' configuration and is 150 mm away from the anode tip.

Figure 4.5 shows the trigger circuit of the UofS-I DPF. The spark gap is pressurized in the range of 3 - 5 mbar with compressed air. The primary trigger circuit is triggered by a fiber optic (F. O.) pulse. The capacitor bank is charged by a constant current power supply (up to 75 mA).

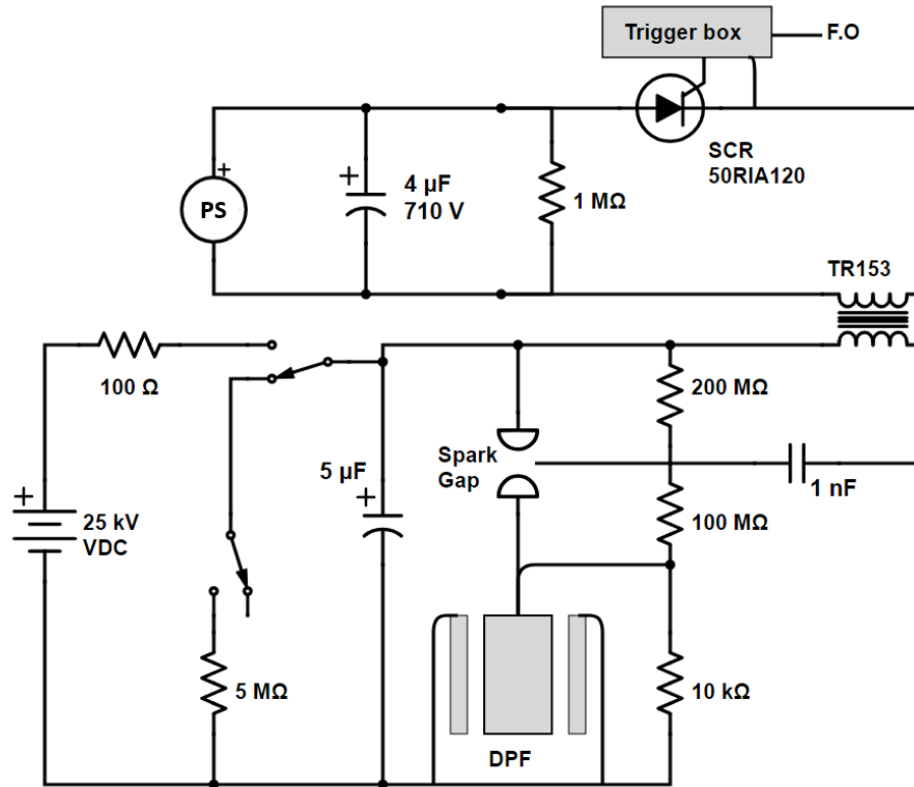


Figure 4.5: The UofS-I DPF trigger circuit.

Figure 4.6 shows the panels in use for the operation of the device. The top panel is the pressure monitor that displays the pressure in the chamber in units of Torr. The middle panel is the control unit. The control unit is responsible for the automated operation for charging and discharging the capacitor bank. A shot counter, a timer knob for resetting the automation cycle, and a spark gap flush timer, are also embedded on this controller. The bottom panel is the power supply. The power supply is capable of charging the capacitor bank up to 30 kV with 75 mA maximum current.

Two identical Ross relay switches that are powered by 115 V AC from the control unit

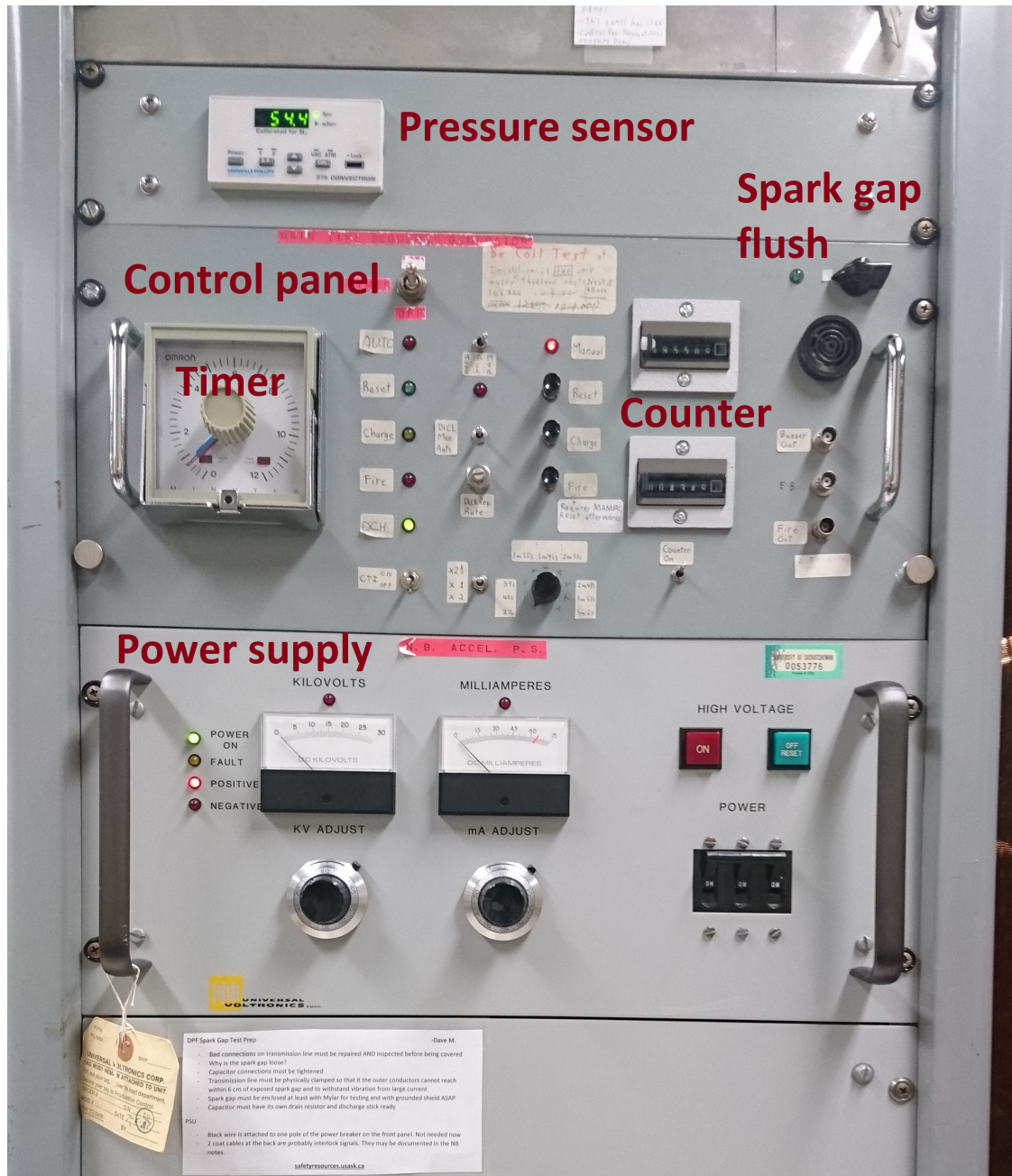


Figure 4.6: DPF control panel: chamber pressure display in Torr (top panel), automated or manual controls for firing/charging/discharging (middle panel), and the power supply controls for capacitor charging (bottom panel).

have been used for charging and discharging the capacitor bank and are shown in Fig. 4.7.

The left Ross relay switch is responsible for both the charging and the idle states (non-charging, non-discharging). The right Ross relay switch is responsible solely for the dumping state after the DPF discharge.

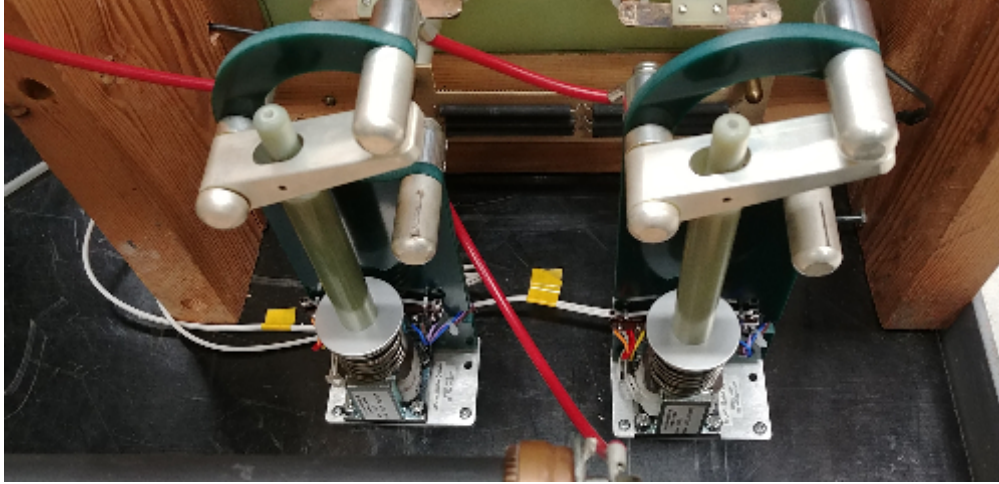


Figure 4.7: Charging and discharging Ross relays used for three different operational states: charging, discharging, and dumping of capacitor. The dumping resistor (behind the relays) consists of parallel resistors in series, equivalently $6.6 \text{ M}\Omega$.

The surplus of discharge (or in cases when there is no discharge or break-down of the spark gap) of current goes through a dumping resistor. The dumping is done using a series of parallel resistors which is equivalently $6.6 \text{ M}\Omega$. The RC time constant for dumping the capacitor is 33 s.

4.3 Electrical Parameter Measurements

4.3.1 Current Measurement

A Rogowski coil can be used to measure a fast current waveform [53]. It consists of windings in toroidal form encircling a current path with current $I(t)$ as shown on Fig. 4.8 (using I explicitly to distinguish from circuit current, i). In this diagram, the minor diameter is $c = (b - a)/2$ with a and b as the major inner and outer diameters of the coil, and R is the resistance parallel to the output signal, $V_{out}(t)$.

According to Ampere's law, the relation between the current flowing through the Rogowski coil and the magnetic field along the axis of the torus is given by

$$I(t) = \frac{1}{\mu_0} \oint \vec{B}(t) \cdot d\vec{s} \quad (4.5)$$

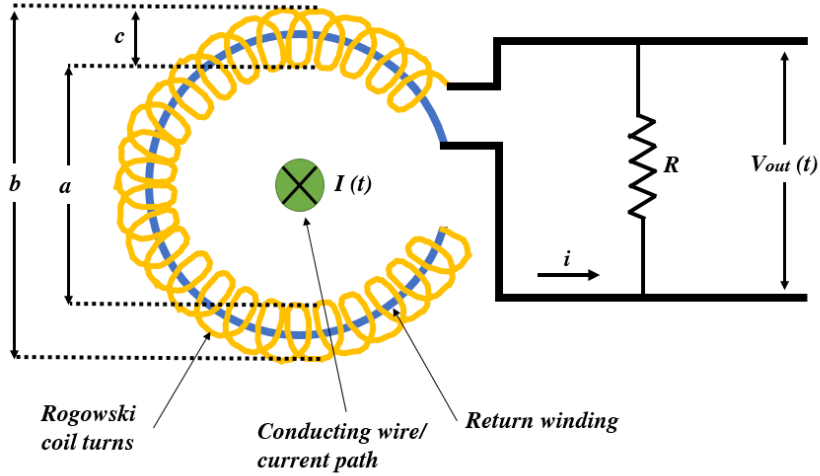


Figure 4.8: Rogowski coil equivalent circuit encircling a current path (in green). Rogowski coil turns (in yellow) wound an internal loop (in blue) forming a toroidal configuration encircling the conducting wire for which the current is to be measured.

where s is the path along the torus, $B(t)$ is the magnetic field, and μ_0 is the permeability of free space constant. Here, the magnetic field variations induce the voltage in the windings.

Furthermore, the magnetic flux that threads along the minor cross-section of the torus is given by

$$\phi(t) = B(t) \cdot A = \left(\frac{\mu_0 A}{2\pi a} \right) I(t) \quad (4.6)$$

where A is the minor cross-section of the windings, and a is the minor radius of the coil.

A relation between the induced voltage in the terminal of the coil, $V(t)$, and the induced flowing current, $I(t)$, can be written using Faraday's law:

$$V(t) = \frac{d\phi}{dt} = \left(N \frac{\mu_0 A}{2\pi a} \right) \frac{dI(t)}{dt} \quad (4.7)$$

where N is the number of turns of the coil.

It is apparent from equation (4.7) that the induced voltage, $V(t)$, across the terminal of the coil is proportional to the rate of change of current, and not the current itself. Thus, an integrator system is necessary at the coil output terminal to derive the current value from

the induced voltage.

A simple RC circuit can be configured as an integrator, which is presented in Fig. 4.9.

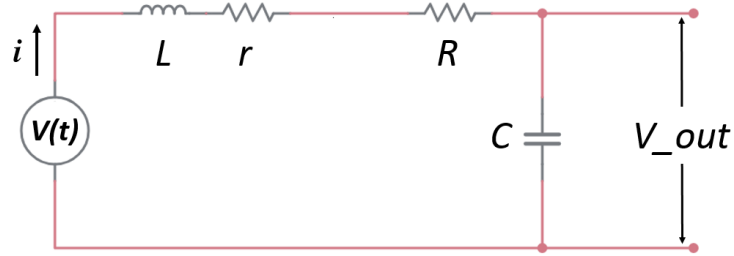


Figure 4.9: RC circuit used as a current integrator connected to the Rogowski coil. L and r are the internal inductance and resistance of the Rogowski coil, and R and C are the external resistor and capacitor. An output signal to oscilloscope is on the right.

In Fig. 4.9, the L and r are the self inductance and resistance of the coil, and R and the C are the resistor and capacitor of the integrator circuit, respectively. Thus, with the current, i , flowing in this circuit, the circuit equation becomes

$$V(t) = L \frac{di}{dt} + (R + r)i + \frac{1}{C} \int_0^t i dt \quad (4.8)$$

For the dominant Fourier component with frequency ω , there may be a situation that the order of the magnitudes of the first two terms in the integral-differential equation (4.8) satisfies the following inequality:

$$R + r \approx R \gg \omega L \quad (4.9)$$

where ω as the highest frequency in the Fourier transform spectrum of the source current. Thus, ignoring the small value of the self-inductance of the coil, L , one can rewrite equation (4.8) as

$$V(t) = Ri + \frac{1}{C} \int_0^t i dt \quad (4.10)$$

A formula can be derived for V_{out} across C as

$$V_{out}(t) = \frac{1}{C} \int_0^t i dt = \frac{1}{RC} \int_0^t V(t) dt = \frac{1}{RC} N \frac{\mu_0 A}{(2\pi a)} I(t) \quad (4.11)$$

The approximation is made if the current pulse duration is much larger than the integration time, $\tau = RC$.

It can be observed in equation (4.11) that the higher the integration time ($\tau = RC$) is, the higher accuracy one can achieve at the cost of smaller signal amplitude, V_{out} .

Furthermore, the Rogowski coil can also possess an intrinsic integrator without requiring an external integration block in high frequency measurements. In this case, the condition from equation (4.9) is inverted:

$$r + R \ll L\omega \quad (4.12)$$

This Rogowski coil self-integrated circuit is presented in Fig. 4.10. Here, a small external resistor, R , is added to the input signal (the external resistance is normally chosen to be approximately equal to the small coil resistance, i.e., $R \approx r$).

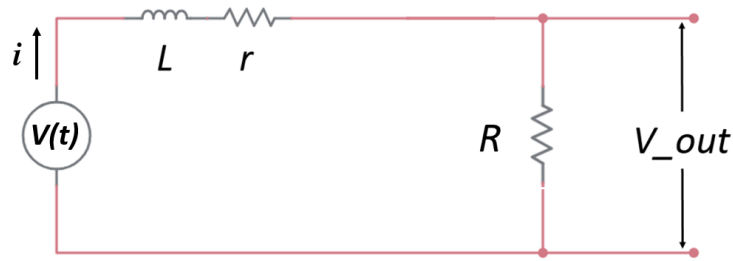


Figure 4.10: Self-integrating circuit of the Rogowski coil. A small external resistor, R , is added to the input signal. An output signal to oscilloscope is on the right.

The Rogowski coil self-integrated circuit equation is

$$V(t) = L \frac{di}{dt} + i(R + r) \quad (4.13)$$

If the inductance of the coil is large (ignoring the terms with R and r):

$$V(t) \approx L \frac{di}{dt} \quad \rightarrow \quad i = \frac{1}{L} \int V(t) dt \quad (4.14)$$

The output voltage across the external resistor, R , is

$$V_{out}(t) = Ri = R \frac{1}{L} \int V(t) dt = R \frac{1}{L} N \frac{\mu_0 A}{(2\pi a)} I(t) \quad (4.15)$$

In such case, the output voltage, $V_{out}(t)$, is proportional to the current through the coil, $I(t)$.

The Rogowski coil is in a closed-loop structure, and the coil can have any shape. This is analogous to the Ampere's law which states that any closed loop integral of the magnetic field around a current path is equal to the current. Moreover, the orientation of the flowing current has no effect on the output. Thus, these features make the Rogowski coil a flexible device for current measurements and is the preferred choice in most cases.

Figure 4.11 shows the commercial "Pearson" Rogowski coil used to measure the fast current waveform in the UofS-I DPF device.



Figure 4.11: A commercial Rogowski coil used to measure the fast, high current waveform from the DPF discharge. Extra "Kapton" tape is added to provide high-voltage insulation.

4.3.2 High Voltage Measurement

The transient voltage across any two points in the circuit can be measured using a resistive voltage probe [53]. A high voltage probe is a resistive divider which consists of a series of resistors shunted by a resistor at one end where the attenuated output signal is sampled. The frequency response of the probe limits its response time, and the divider is connected to an oscilloscope.

Figure 4.12 shows the Tektroniks P6015a voltage probe. The probe has a built-in attenuation of 10^3 . The signal is further attenuated before it is connected to the digital oscilloscope. It is hooked onto the DPF anode outside the chamber to measure the anode voltage with respect to the grounded cathode.

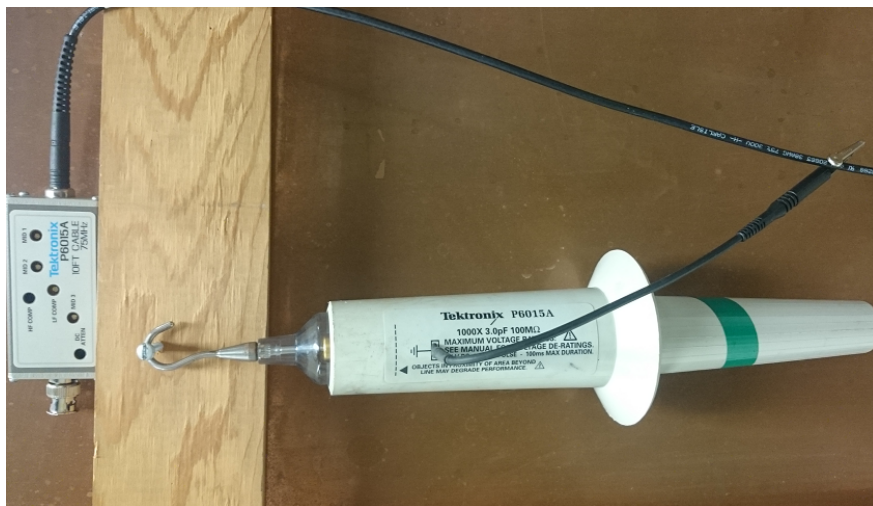


Figure 4.12: A Tektroniks P6015a voltage probe used to measure the voltage of the DPF anode.

4.3.3 Soft and Hard X-ray Measurements

Measurements of x-ray emissions provide information about the condition of the high temperature and density plasma from a pulsed discharge, thus, it is important to examine the emission characteristics including its intensity, waveform, and its spectra.

Time-resolved radiation of SXR and information related to the energy spectra can be

studied using a four-channel photodiode array. This detector consists of four windowless silicon PIN BPX-65 photodiodes that have wide spectral range and fast response. These PIN diodes are sensitive to soft x-rays. Masking the windows of the photodiodes with thin filters of selected material and thickness allows the control of transmission energy band of x-rays.

The negatively-biased BPX-65 circuitry is shown in Fig. 4.13. The response time delay of the BPX-65 detector is assumed to be negligible. A picture of the circuit box and several Si-PIN photodiodes are shown on Fig. 4.14.

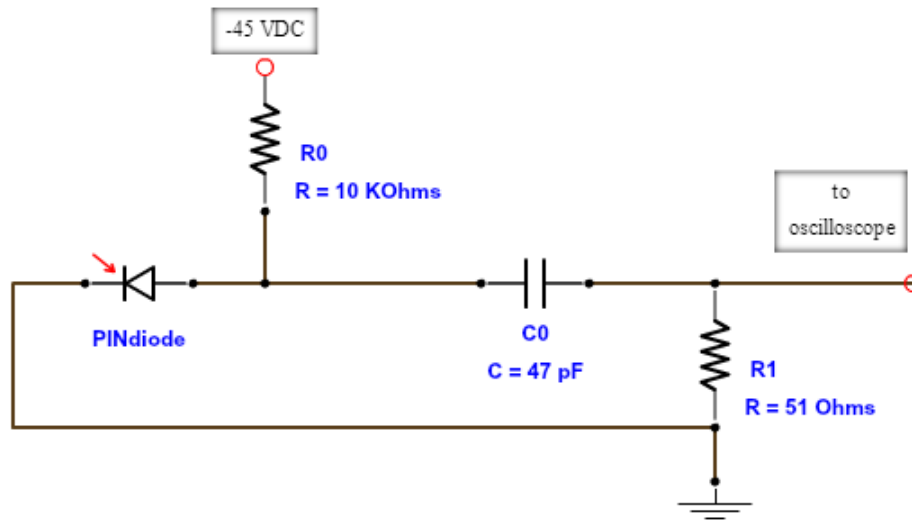


Figure 4.13: Negatively-biased BPX-65 circuit.

All four PIN diodes have been cross-calibrated using the same filter type and thickness prior to experimentation. All the signals were obtained using long, equal-length coaxial cables and BNC connectors.

Figures 4.15 and 4.16 show the attachments of the two sets of SXR detectors on the DPF chamber. Both detectors have equal distances away from the pinch position. One set views horizontally and the other set vertically upwards to the pinch position.

A double-filter method has been used to analyze the energy spectrum of the soft x-rays. The filters are different thicknesses of cobalt foils ranging from 5 to 30 μm . The cobalt

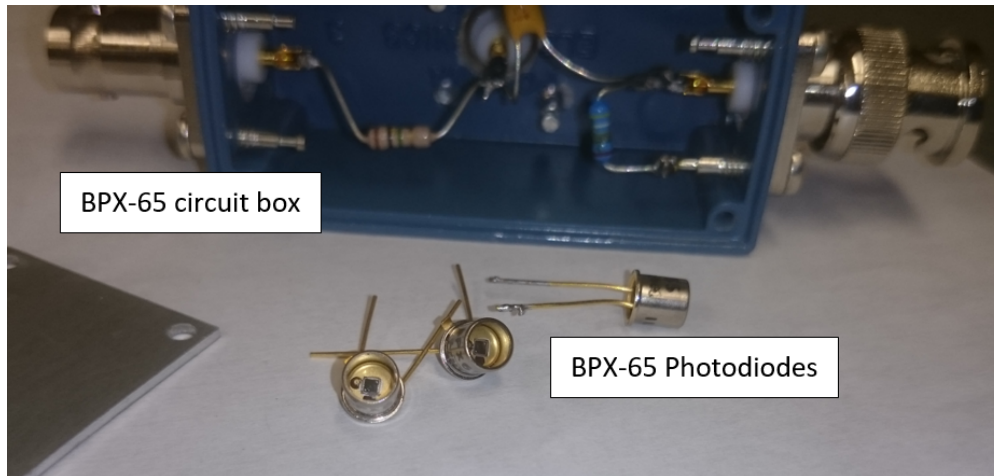


Figure 4.14: Silicon-PIN BPX-65 photodiodes and the circuit box.

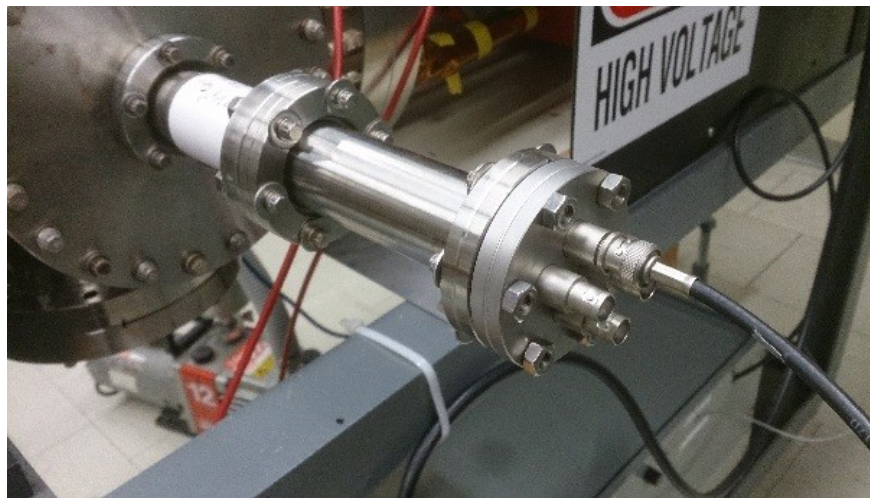


Figure 4.15: A 4-PIN photodiode array attachment on one side of the chamber situated at the same distance from the pinch position as that of the other array under the chamber. The other array is shown in Fig. 4.16.

material has been chosen because it allows primarily a specific energy window that transmits x-rays through it. For example, when the detector is masked with a copper filter, the detector mainly allows the transmission of x-rays in the 4 - 9 keV energy range which includes the $\text{Cu-K}\alpha$ (8.05 keV) and $\text{Cu-K}\beta$ (8.9 keV) lines. The detector masked with an aluminum filter allows the transmission of x-rays from 3 keV onward, and from 8 keV onward when masked with lead. The detector masked with a cobalt filter, however, makes the detector sensitive only to x-rays in the 4 - 7.7 keV range (Fig. 4.17) [54], discriminating the Cu-K emission



Figure 4.16: A 4-PIN photodiode array attachment under the chamber to allow more simultaneous detection of SXR per shot.

lines significantly.

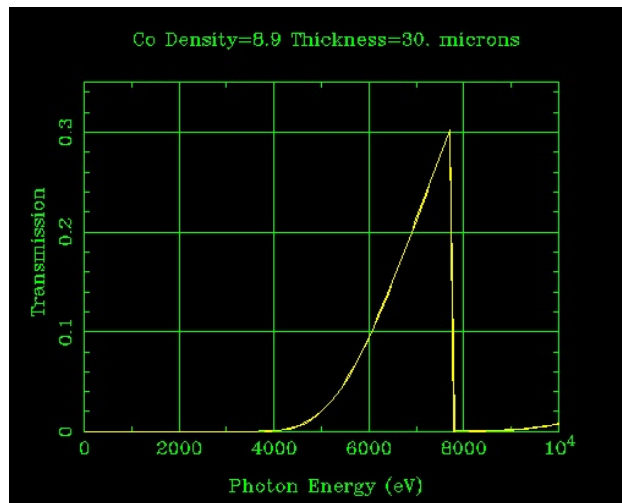


Figure 4.17: A 30-micron cobalt foil filter x-ray transmission as a function of photon energy in eV calculated using the CXRO site [54]. The curve shows a transmission window of 4 to 7.7 keV, which discriminates the copper line at 8.08 keV. The sharp drop of the transmission around 7.7 keV is due to the resonant absorption edge of cobalt.

Since the aim of this research is to solely measure the continuum radiation emission (avoiding the impurity line radiations coming from the copper electrode and electron interactions), using cobalt as a filter is highly suitable.

The comparison of the intensities absorbed by the detectors masked with different types of

filters (such as Cu, Co, and Ni) can also demonstrate the contribution of Cu-K α and Cu-K β in the x-rays radiated from the plasma [24]. Selecting a set of filter type is critical in studying relevant information about the x-ray transmission that comes from the bombardment of energetic electrons on the anode tip.

Furthermore, it has been well observed from recent experiments that most (up to 95%) of the measured soft x-rays come from the Cu-K α due to the interaction of the accelerated electrons with the copper anode during the post-pinch phase. It has also been widely suggested that the use of a hollow or engraved anode will suppress this line emission contribution in the time-resolved SXR intensity measurement [21]. As a result, a hollow anode is used in this research to minimize the electron-anode interaction. The use of a hollow anode will also allow the measurement of the electron beam.

A photomultiplier tube (PMT) has been used for hard x-ray diagnostics [53]. It is a device that is sensitive to high-energy photons and is capable of converting photon signals into electrons using a photo-cathode. These electrons are then multiplied through stages of biased dynodes into the anode.

PMTs are paired with a scintillator for x-ray detection. This is mainly due to the fact that the photocathodes in the PMTs are only sensitive to photons in the UV and visible spectrum. Scintillators are sensitive to photons up to the gamma ray region, as well as particles of sufficient energies, including neutrons. When used as an x-ray detector, the scintillator converts these high energy photons to a suitable wavelength that matches the peak of energy response curve of the PMT photocathode.

The assembly of the PMT and scintillator for hard x-ray detection can be seen in Fig. 4.18. The detector is situated inside the Faraday shielding room and around 2 meters away from the chamber directly facing the anode tip of the DPF. The hard x-ray must penetrate the vacuum chamber and air before being detected.



Figure 4.18: Picture of the assembled scintillated PMT for detecting hard x-rays situated 2 meters away from the chamber in the Faraday cage, directly facing the anode tip.

4.3.4 Ion Beam Measurement

A Faraday cup is designed to measure the primary positive ion beam current from an ion source through a magnetic field. The Faraday cup collector for ion beams is biased to -124 V in order to reabsorb the secondary electron emission.

Figure 4.19 shows the negatively-biased circuit for the Faraday cup. The response time delay of the Faraday cup detector is assumed to be negligible.

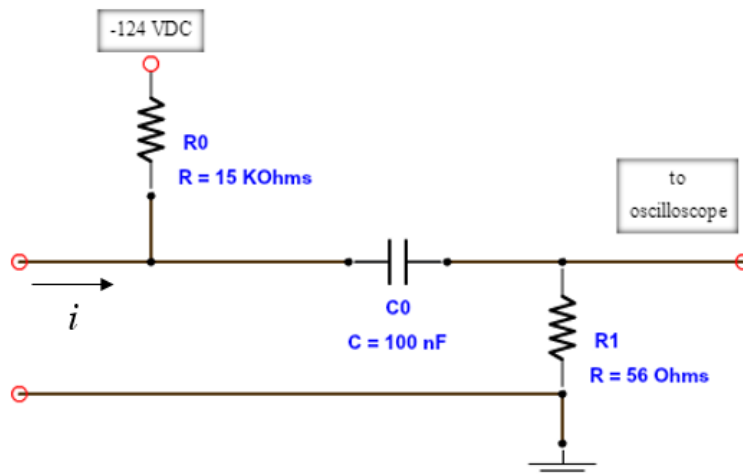


Figure 4.19: A negatively-biased Faraday cup circuit.

The current of the beam is measured using an electrometer connected to a BNC vacuum

feed-through. A shield skirt at the base of the cup prevents the electron or ion current from entering the cup aperture. The shield is also to prevent sputtering of ceramics, which could short out the collector from the grounding [53].

Electrons may be present in the vacuum chamber from the ionization gauges and from the secondary electron emission from the surface due to the interaction between the ion beam with the components in the vacuum system. These electrons need to be filtered. One of the approaches is to use a pair of permanent magnets at the entrance of the cup. These magnets create a magnetic field across the cup entrance that block and trap the electrons from entering.

Moreover, low energy ions are created when a primary ion collides with the background gas atoms. At the instance when the ions collide inelastically, the ion charge and its kinetic energy are transferred to the gas atoms, leaving the resultant ion with a lower energy. Biasing the collector to a positive potential higher than the potential required to repel the incoming primary ion beam allows the low energy charged ions to be rejected at the collector and repelled to the grounded wall of the cup chamber. This low energy ion contribution to the total primary ion beam is very small, however, it varies with background gas pressure and distance from the cup to the source. It could also introduce a significant error to the primary ion current being measured.

A picture of the Faraday cup used in this experiment is presented in Fig. 4.20. The size of the aperture was so chosen to limit the signal amplitude. It was found in other devices that the ion beam intensity depends sensitively on the angle between the axis of the device and the line-of-sight linking the aperture and the plasma focus. In this study, the main concern is the relative ion beam intensity under various pinch conditions rather than its angular distribution.

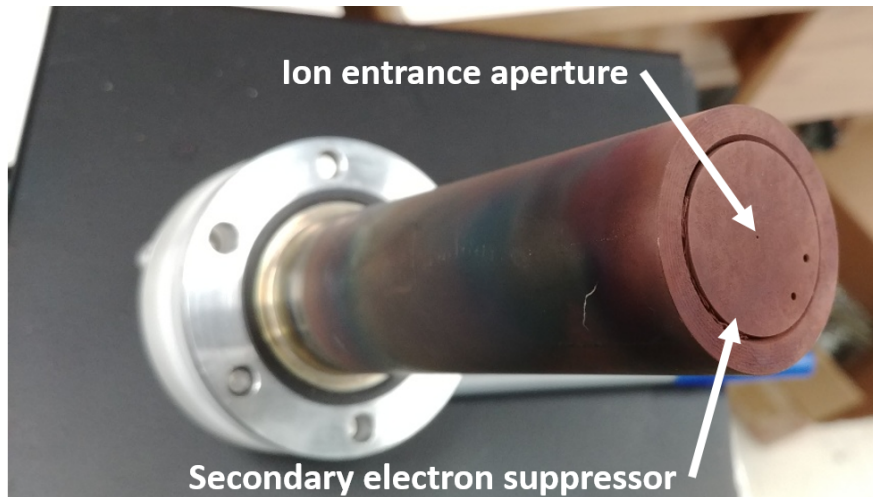


Figure 4.20: The Faraday cup. The cup is attached inside the vacuum chamber and the collector end is situated 70 mm away from the anode tip. The copper layer on the surface of the cup is due to the copper impurities.

4.3.5 Data Acquisition

Three identical digital oscilloscopes (Tektronix TDS 2024c) have been used to record various signals. The picture of the oscilloscopes is shown in Fig. 4.21.



Figure 4.21: Tektronix oscilloscopes (TDS 2024c) for signals measurement and recording, with attached USB flash drives for storage. Each oscilloscope inputs 4 channels triggered by a common signal.

Each oscilloscope allows 4 different signals through a BNC input, and all oscilloscopes can be triggered simultaneously using one external trigger. The signals on the displays are color coded and are graphed simultaneously on the same time scale. The oscilloscopes are equipped with a USB slot for saving data files.

The initial input stage of digital storage oscilloscopes is a vertical amplifier. These vertical attenuation controls allow the adjustment of the amplitude range to match that of the signals. The analog-to-digital converter built in the oscilloscopes then samples the signal at discrete points to digital values. These sample points are then stored in the oscilloscopes' memory. The oscilloscopes' display retrieves these record points from memory, and the start and the stop points to record are determined by a trigger system.

A display of signals on the oscilloscope is shown on Fig. 4.22. The information on scale divisions is shown at the bottom of the oscilloscope screen. In this particular case, the horizontal scale is set to 500 ns per division, while the vertical division is indicated by each of the color-coded signals.

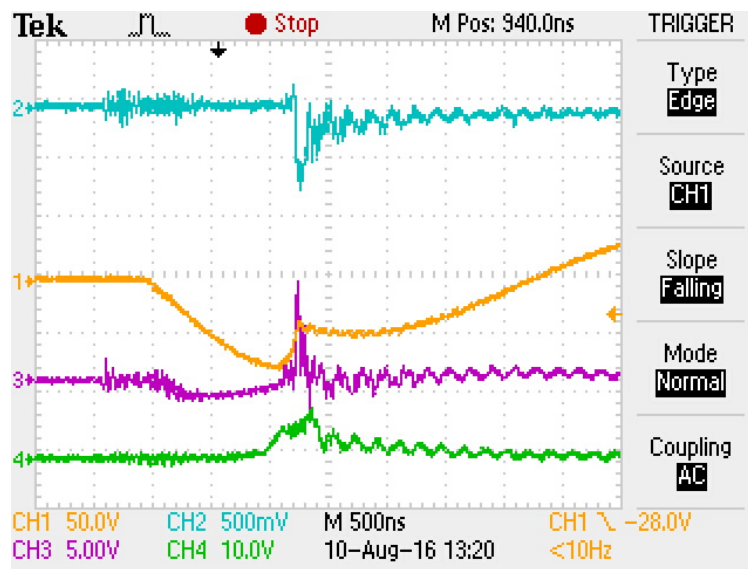


Figure 4.22: Tektronix oscilloscope (TDS 2024c) signals display: labels at bottom indicate divisions of four channels and time division of 500 ns. Ch. 1 (in orange) represents the inverted current trace with 50.0 V/div.; ch. 2 (in blue) represents the inverted HXR signal with 500 mV/div.; ch. 3 (in magenta) represents the electron beam signal with 5.00 V/div.; and ch. 4 (in green) represents the ion beam signal with 10.0 V/div. The signals are triggered by a common falling edge from ch. 1.

In this figure, channel 1 represents the inverted discharge current signal in orange, with a vertical scale of 50.0 V per division. Channel 2 represents an inverted HXR signal with 500 mV per division in blue. Channel 3 represents the electron beam signal with 5.00 V per division in purple, and channel 4 represents the ion beam signal with 10.0 V per division in green. The trigger settings are shown on the right. It shows that the oscilloscope is triggered using a falling-edge slope of the current signal from channel 1.

4.4 UofS-I DPF Operation and Parameters

The operation of the DPF device is initiated by pumping the chamber to a low pressure. A 2-stage rotary vacuum pump is used to vacuum the chamber down to a base pressure of 5 mTorr. Once the vacuum pressure stability is achieved, argon gas is supplied up to the desired operating pressure (100 - 200 mTorr in this experiment). This cycle is typically done several times to clear the chamber of possible impurities.

While the pressure is stable with the suitable operating pressure, a power supply is used to charge the capacitor bank up to 20 kV. Once the capacitor is charged up to the desired operating voltage, a discharge from the capacitor bank through a pressurized spark gap connected the anode chamber is delivered by means of a trigger signal. The oscilloscopes subsequently measure and record the input signals.

Figure 4.23 shows the sequence of operation in automation for the UofS-I DPF device using the control unit. Here, the capacitor bank is charged up to 20 kV within a duration of 25 s, and subsequently the buzzer and the fire signals are initiated at the 28th second and 30th second, respectively. The capacitor is then dumped right after the firing with a duration of 30 s until the sequence resets after 1 min. After at least 10 shots, the chamber is pumped and then filled with fresh argon gas.

The running parameters of the UofS-I DPF device is summarized in Table 4.1.

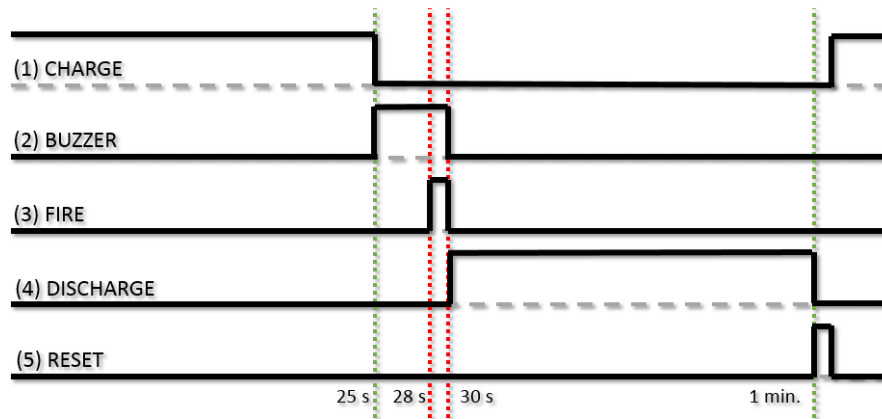


Figure 4.23: Timing sequence for operation in automation: capacitor charging duration of 25 s, buzzer at 25th s, fire at 28th s, dumping at 30th s with a duration of 30 s, and resets after 1 min. The cycle repeats after the reset.

Table 4.1: The UofS-I DPF device parameters and locations of detectors.

UofS-I DPF Device	
Bank capacitance, C_0	5 μ F
Static inductance, L_0	150 nH
Charging voltage, V_0	20 kV
Operating gas	argon
Operating pressure, p_0	100-200 mTorr
Electrode material	copper
Anode radius, a	15 mm
Anode length, z_0	50 mm
Cathode radius, b	50 mm
Insulator material	quartz-infused glass
Insulator radius	17 mm
Insulator length	30 mm
Si-PIN photodiodes	300 mm away anode tip
HXR scintillator	2 m away anode tip
Electron beam core conductor	150 mm away anode tip
Faraday cup	70 mm away anode tip

Chapter 5

Simulation and Experimental Results

The shots recorded in this experiment have been obtained at different sessions over a spread of several months. Nevertheless, the operating parameters and the DPF configuration have been kept constant. The operating conditions have also been verified prior to experimentation such that the plasma focusing were occurring at the same pinch time, which is mainly affected by the charging voltage and the operating pressure. The less-than-ideal reproducibility of the pinch phenomenon is intrinsic [8] and will resort the study to statistical methods in analysis.

5.1 UofS-I DPF Plasma Dynamics

The plasma dynamics can be studied using the anode voltage and the current discharge signals. Furthermore, the emission of charged particles and x-ray radiation with respect to the pinch phase gives information of the pinch phenomenon. Figure 5.1 shows the plotted typical raw signals obtained using argon gas at 20 kV charging voltage and 150 mTorr operating pressure. The traces, from top to bottom, are the anode voltage, the discharge current, the electron beam, the ion beam, the soft x-ray, and the hard x-ray signals. It can also be observed that there exist some time delays between the signal peaks with respect to the pinch time, as marked.

The discharge current and the tube voltage signals give information on the plasma dynamics of the pinch phenomenon. The axial rundown phase is ended when the voltage signal starts to rise, initializing the radial compression phase. As can be observed, this is also the time when the discharge current signal starts to plateau, and where the Faraday cup detector

signal experiences a slow increase in signal. Once the plasma is compressed at the tip of the anode, the anode voltage reaches its maximum value.

The peak of the voltage signal indicates the time when the plasma is compressed to a minimum radius. This voltage spike and the current dip are features of the pinch when an increase of the plasma column impedance has occurred. This has also been verified by using a set of photo detectors wherein a column-shape of the compressed plasma can be photographed (Fig. 2.3).

At some time after the pinch phase, beams of ions and electrons are emitted along opposite axial directions due to a sharp change in the electric field. This occurs right after the compression phase. The electrons are emitted back axially, while the ions are emitted in the opposite axial directions, hitting the Faraday cup. X-rays are also radiated due to this compression, as well as from the interaction of the scattered electrons with the electrodes.

For the UofS-I DPF device, the plasma sheath typically takes $1.15 \mu\text{s}$ to be accelerated axially from the base to the tip of the electrodes (axial acceleration phase). When the sheath arrives at the tip of the electrodes, it takes 400 ns to fully compress the plasma radially inwards (radial compression phase). The pinch phase occurs at around $1.55 \mu\text{s}$. These time durations agree with other comparatively small DPF devices [10].

The time delays relative to the pinch time of several signals are also studied in Fig. 5.1. It takes 60 ns for the electron beam to peak from the pinch time, while it takes around 300 ns for the ion beam flux to peak. These beams are, indeed, a product of the plasma compression and the change in electric field, wherein the ions are emitted axially upwards to the Faraday cup while the electrons are accelerated axially backwards towards the anode. Moreover, given these time delays and the distance from the pinch location, one can further study the energy distribution of ion beams using the time of flight (TOF) method [13].

Furthermore, it takes 30 ns for the SXR to peak, and 120 ns for the HXR to peak relative to the pinch time. The radiation emissions take a relatively short amount of time right after the pinch effect compared with the ion beam.

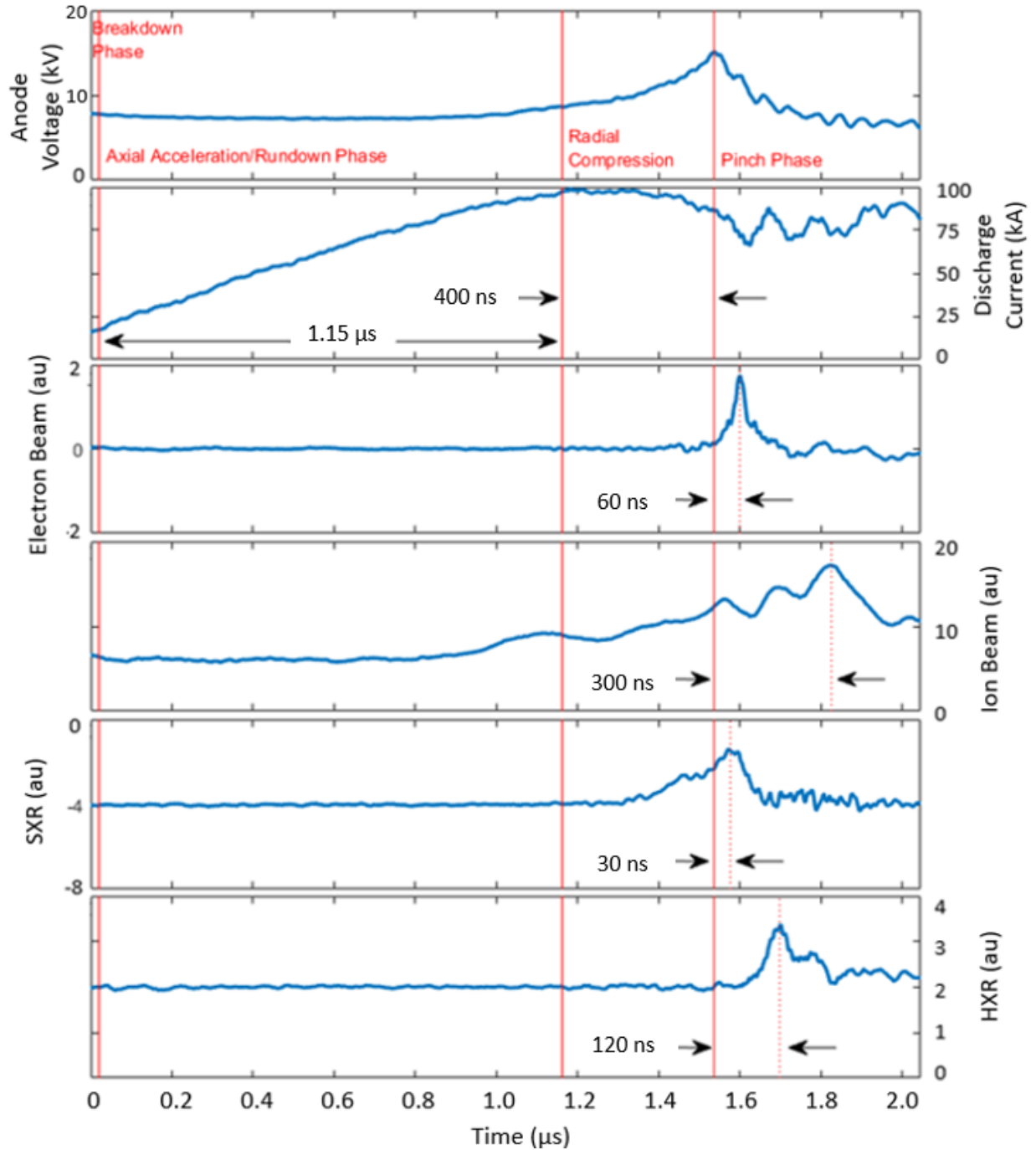


Figure 5.1: Raw signals (from top to bottom): Discharge current from Rogowski coil, anode voltage from voltage probe, electron beam from charge collector and Rogowski coil, ion beam from Faraday cup, SXR from PIN diode, and HXR from PMT-scintillator. The different phases of plasma dynamics, and the time difference of peaks of signals relative to the pinch phase are also defined.

5.2 Lee Model Simulation

In order to evaluate the performance of the UofS-I DPF device, the experimental waveforms are compared with the Lee model current trace (as discussed in section 2.2). The Lee model worksheet has been configured for the UofS-I DPF machine with known capacitance, inductance, electrodes' dimensions, and the operating parameters, which are presented in Fig. 5.2.

	A	B	C	D	E	F
1	Plasma Focus Computation: 5 Phase Model by S Lee: RADPFV5.15de.c					
2	I. Axial Phase	II. Radial Inward Shock	III. Radial Reflected Shock	IV. Slow Co		
3	Device:					
4	Lo	Co	b	a	zo	ro mOhm
5	143	5	4.5	1.5	5	18
6	massf	currf	massfr	currfr	Model Parameters	
7	0.046	0.7	0.31	0.7		
8	Vo	Po	MW	A	At-1 mol-2	Operational
9	20	0.2	40	18	1	Parameters

Figure 5.2: The model and operational parameters of the UofS-I DPF encoded onto the Lee code excel file for simulation and computation: The first two rows in the box are the DPF geometrical and electrical circuit parameters, the next two are the fitting and model parameters, and the last two are the operating parameters [39].

The following parameters are used: Capacitor inductance $L_0 = 143$ nH, capacitor bank capacitance $C_0 = 5$ μ F, cathode radius $b = 4.5$ cm, anode radius $a = 1.5$ cm, anode length $z_0 = 5$ cm, and capacitor resistance $r_0 = 18$ m Ω .

The model parameters, *massf*, *currf*, *massfr*, and *currfr* are the fitting parameters that are the constants at play in the equations used in the computations, particularly the mass and current factors. Output values of $f_m = 0.046$, $f_c = 0.7$, $f_{mr} = 0.31$, and $f_{cr} = 0.7$, have been obtained from the Lee code fitting (Fig. 5.6).

The charging voltage in the simulation is set to $V_0 = 20$ kV, and the operating pressure to $P_0 = 0.2$ Torr. The atomic mass of the operating gas is set to $MW = 40$ for argon, and its atomic number $A = 18$. The *At - 1 mol - 2* represents whether the operating gas is atomic (eg. Ar, N, He) or molecular (eg. N₂, O₂, H₂, etc.) and is set to "1" for argon.

Figure 5.3 shows the short-circuit current waveform of the device obtained from a Pearson

Rogowski coil. The period and the frequency of the current waveform are measured to be $T = 5.3 \mu\text{s}$ and $f = 188 \text{ kHz}$, respectively. Consequently, the frequency of the waveform is used to calculate the static inductance, L_0 , based on the known capacitance. The decaying envelope of the oscillations in the plot can be used to calculate the resistance in the circuit, but that is not a main concern for the circuit analysis or the Lee model.

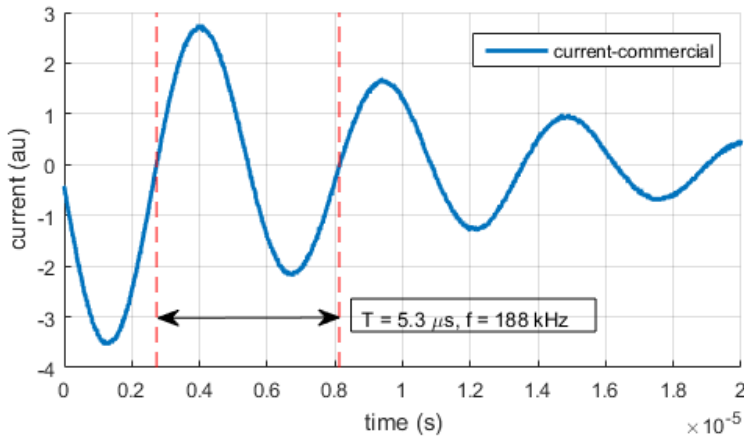


Figure 5.3: A short-circuit RLC current waveform signal of the UofS-I DPF measured using a Rogowski coil (solid blue), with a recorded and measured time period of around $5.3 \mu\text{s}$ and a frequency of 188 kHz calculated from the zeroes of the sinusoid (vertical dashed red).

Furthermore, the Lee code is also used to find the optimal operation conditions. Figure 5.4 shows several current traces computed from the Lee code. The current waveforms are plotted as a function of time and charging voltage ranging from 15 to 25 kV with a fixed operating pressure of 150 mTorr of argon gas.

It is very important to stress that the plasma focus current waveform is significantly distorted from the unloaded damped sinusoidal waveform of the RLC circuit discharge. Such distortions are mainly due to the electrodynamic effects of the motion of the plasma, particularly the axial and radial dynamics, as well as the SXR emission of the plasma. It is also good to note that the dynamic resistance caused by the motion of the plasma in the radial phase dominates and causes the current dip in the current trace, as can be seen in Fig. 5.4.

Figure 5.4 also shows how the current dip shifts to an earlier time when the charging

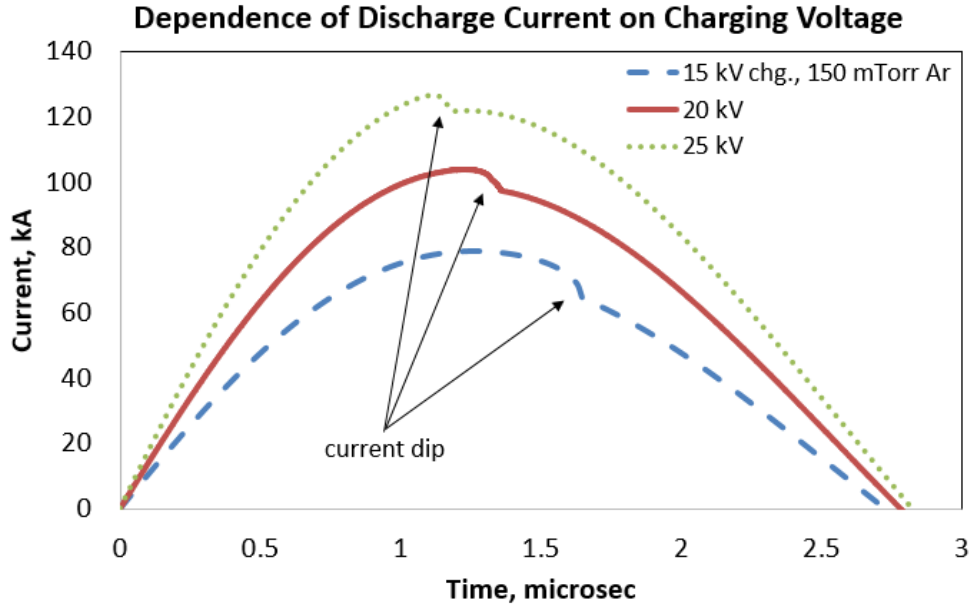


Figure 5.4: Calculated current waveforms at various charging voltages: 15 kV (dashed blue), 20 kV (solid red), and 25 kV (dotted green) at a fixed operating pressure of 150 mTorr of argon gas using the Lee code. An increase in current and a time shift of the current drop to the left, is evident due to an increase in charging voltage.

voltage is increased, as well as increasing the discharge current (both at a fixed operating pressure of 150 mTorr). This is because of the faster motion of the current sheath at larger charging voltage and discharge current during the axial phase due to a larger $\mathbf{J} \times \mathbf{B}$ force. At 15 kV, the pinch occurs well after the current peak, which is not preferred.

A general task for optimizing the operating parameters is setting the pinch time close to where the current peaks (as discussed in section 4.1). This is to maximize the stored inductive energy in the DPF head which, in turn, is converted to the energy in the pinched plasma. Thus, if one sets the operating pressure to 150 mTorr of argon gas, one can deduce from Fig. 5.4 that a charging voltage of 20 kV is optimal that has a pinch time at 1.3 μs .

Likewise, Fig.5.5 shows the shifting effects of the pinch time caused by varying the operating pressure ranging from 100 to 300 mTorr (with a fixed charging voltage of 20 kV). It is apparent that the current drop is shifted to an earlier time as the pressure is decreased. Thus, if one operates at a fixed charging voltage of 20 kV, the optimal operating pressure in argon gas must be around 150 mTorr, where the current drop occurs at the current peak at

around $1.3 \mu\text{s}$.

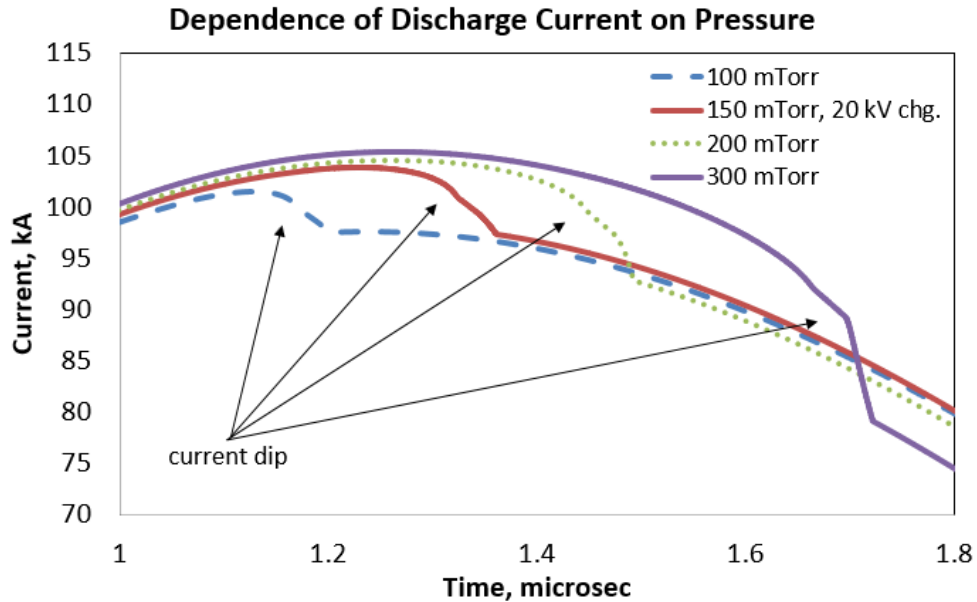


Figure 5.5: Calculated current waveforms at various operating pressures: 100 mTorr (dashed blue), 150 mTorr (solid red), 200 mTorr (dotted green) and 300 mTorr (solid violet) of argon gas at a fixed charging voltage of 20 kV using the Lee code. A time shift of the current drop to the left is evident as the pressure is decreased.

The Lee code provides rich information on the plasma dynamics based only on the critical experimental current waveform fitted with the computed current waveform. The simulation provides information on the plasma radius and speed in the radial phase, the pinch time and duration, the plasma temperature, the tube voltage, and the radiation power, just to name a few. An example of a good fitting in the Lee code can be seen in Fig. 5.6. The fitting is obtained by varying the model parameters (mass and current factors for the axial and radial phases).

Figure 5.7 shows the computed current trace as well as the anode voltage, and showing the current dip at the current peak. The radial phase starts at $1.275 \mu\text{s}$ with a duration of $0.218 \mu\text{s}$, and the duration of the pinch is 19.0 ns. It is good to point out that the end of the axial phase, which is the start of the radial phase, does not occur at the apparent current dip, but slightly earlier. In fact, the Lee code expects that there is no distinct indication on the current trace that precisely marks the start of the radial phase [49]. The end of the axial

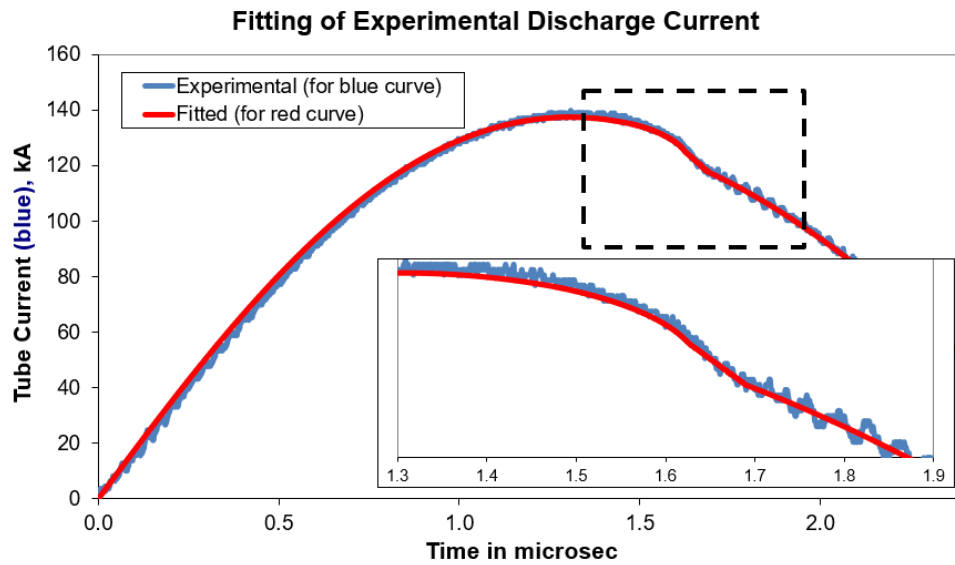


Figure 5.6: Comparison between the experimental (blue) and computed (red) discharge current waveforms. The fitting is nearly perfect, and both shows that the pinch phase starts at around $1.5 \mu\text{s}$.

phase likely occurs when the current trace starts to plateau, right before the current dips.

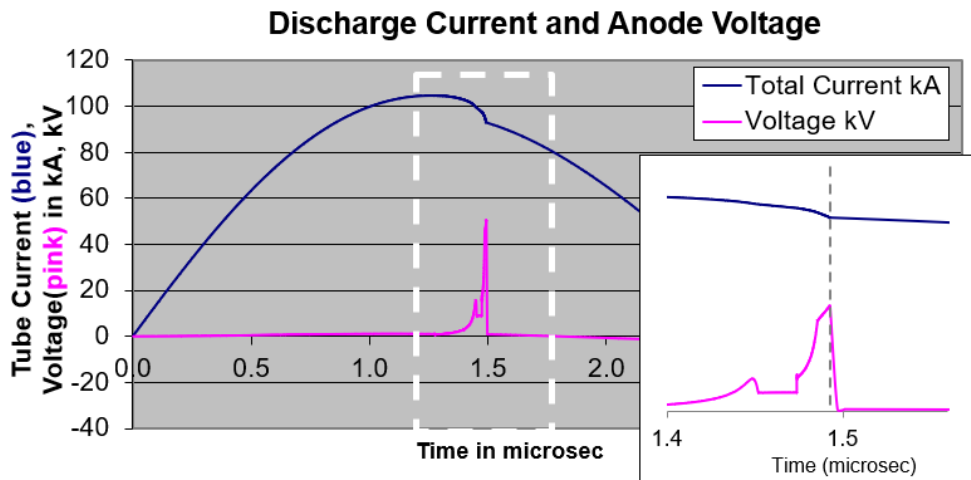


Figure 5.7: The computed discharge current waveform (blue) and the anode voltage (pink) from the Lee code, showing the pinch effect corresponding to the peak of the voltage and the end of the current dip.

Figure 5.8 shows the axial position and speed of the plasma sheath. The peak axial speed is also calculated to be $6.4 \text{ cm}/\mu\text{s}$. Expressing such value as 64 km/s gives an idea of how fast the speeds are in a DPF. Likewise, since it is in strong shock wave speeds, it can give

an idea of the temperature by the conversion of a high kinetic energy to high temperature. The kinetic energy of argon ions at this speed can reach up to a 100 eV, or a temperature of around a million Kelvin.

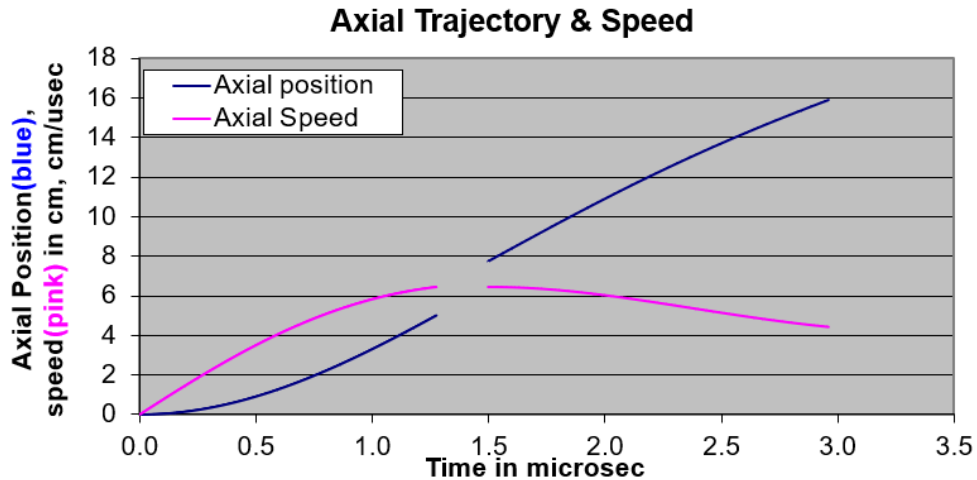


Figure 5.8: The computed axial plasma position (in blue) and the speed (in pink) in the axial trajectory, with a peak axial speed of $6.4 \text{ cm}/\mu\text{s}$. The gap in the curves indicate that the plasma trajectory is in the radial direction.

The gap in Fig. 5.8 (between $1.25 \mu\text{s}$ and $1.5 \mu\text{s}$) indicates that the plasma sheath has shifted its trajectory from the axial to the radial inward direction.

Figure 5.9 shows the radial positions of the shocks, piston, and elongation of the plasma column during the radial phase.

The inward shock, in dark blue in Fig. 5.9, hits the axis (radius = 0 mm) at 175 ns, where consequently an outgoing reflected shock, in light blue, hits the incoming piston, in pink, at around 200 ns at a radius of 2 mm. It can be interpreted that the pinch phase starts at 200 ns and ends at around 220 ns where the plasma is further compressed to a radius down to 1 mm.

5.3 Electron Temperature Measurement

The electron temperature measurements in this research were done using the double-filter technique based on the ratio method. The ratio method requires a calibration curve

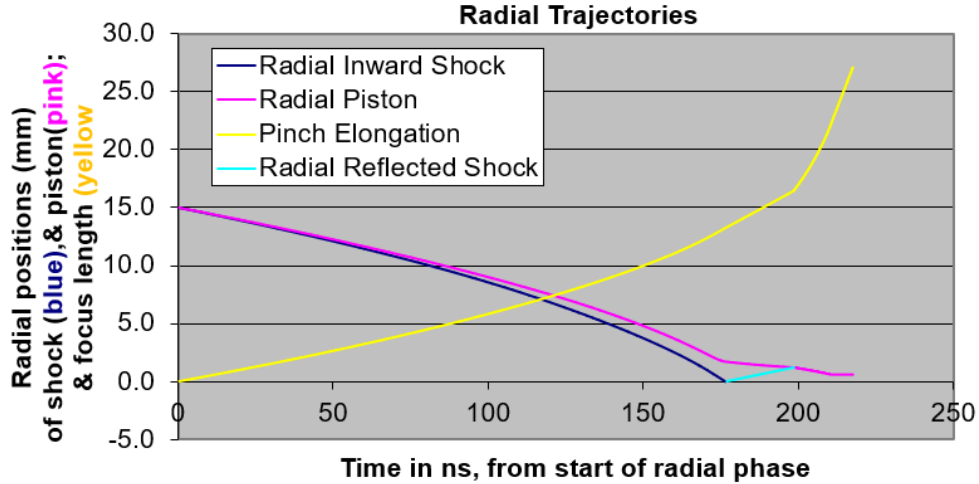


Figure 5.9: The computed radial positions: Radial inward shock (in dark blue), radial piston (in pink), pinch elongation (in yellow), and the radial reflected shock (in light blue). The pinch phase starts at 200 ns.

where the experimental ratio of SXR intensities can be superimposed onto. The calibration curve can be computed based on the attenuation lengths of the filters being used.

The attenuation length is the depth into a material at which the intensity of photons drops to e^{-1} or 37% of its incident value at the surface. The feature to note is that the attenuation in this medium shows a discrete drop at some given energy. Atoms or molecules can be excited from the ground state to some higher levels when incident photons have the matching energies corresponding to the energy difference between the two states. Photons corresponding to the excitation energies of these atoms or molecules are absorbed selectively when they are exposed to external radiation. This is referred to as the *resonant absorption* [55]. These abrupt drops in attenuation length coefficients are caused by the increase in photon absorption when a photon energy radiation equals each of those excitation energies.

Figure 5.10 shows the x-ray attenuation lengths of several filter types (Ti, Ni, Co, and Si) as a function of energy. The data can be obtained from an interactive web application at the CXRO site [54]. The application requires the chemical formula or the element, and the density of the material.

The K-absorption edges of the corresponding materials can be obtained from the NPL

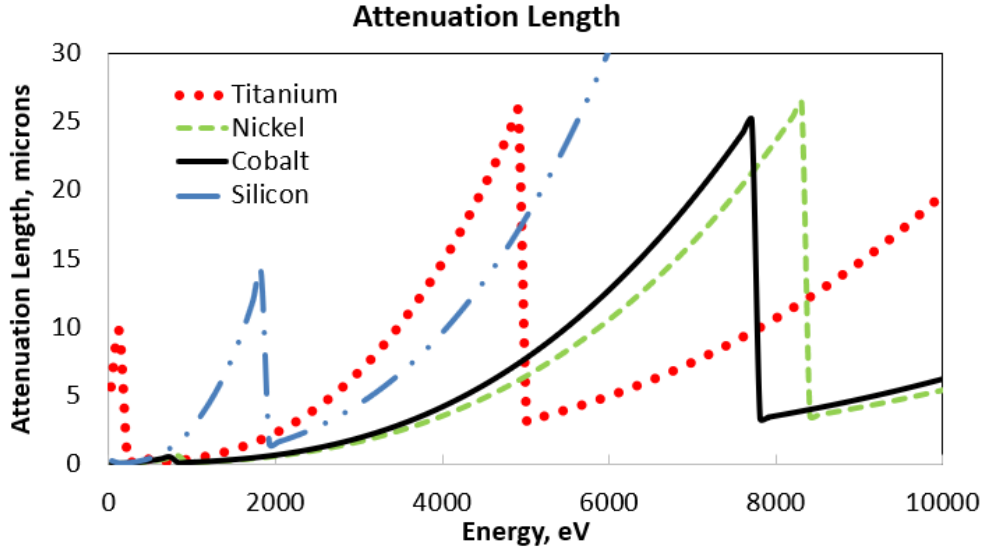


Figure 5.10: Attenuation length coefficients of titanium (dotted red), nickel (dashed green), cobalt (solid black), and silicon (dashed dotted blue), as a function of photon energy. The abrupt drops are due to the corresponding material’s resonant absorption. The x-ray absorption K-edges of Ti, Ni, Co, and Si are 4.965 keV, 8.339 keV, 7.712 keV, and 1.840 keV, respectively.

site [56]. The atomic numbers of these specific materials are close together such that they have neighboring K-edge values (eg. titanium, nickel, cobalt, and silicon have K-edge values of 4.965 keV, 8.339 keV, 7.712 keV, and 1.840 keV, respectively).

The transmission intensities through a given filter at particular energies can be calculated using the formula

$$I = I_0 e^{-x/\mu} \tag{5.1}$$

where I_0 is the incident x-ray intensity, μ is the attenuation length of the filter material, and x is the thickness of the filter.

Figure 5.11 shows the transmission curves of some of the types of filter materials and at different thicknesses. It can be observed that an increase in thickness of a filter (cobalt, for example) causes a decrease in transmission, nevertheless, allows the transmission of x-rays in the same energy range (2500 eV to 7800 eV). The titanium filter, on the other hand, allows a transmission range of 3000 eV to 5000 eV, and increases again at around 7000 eV. The aluminum filter shows a transmission range of around 4000 eV and higher.

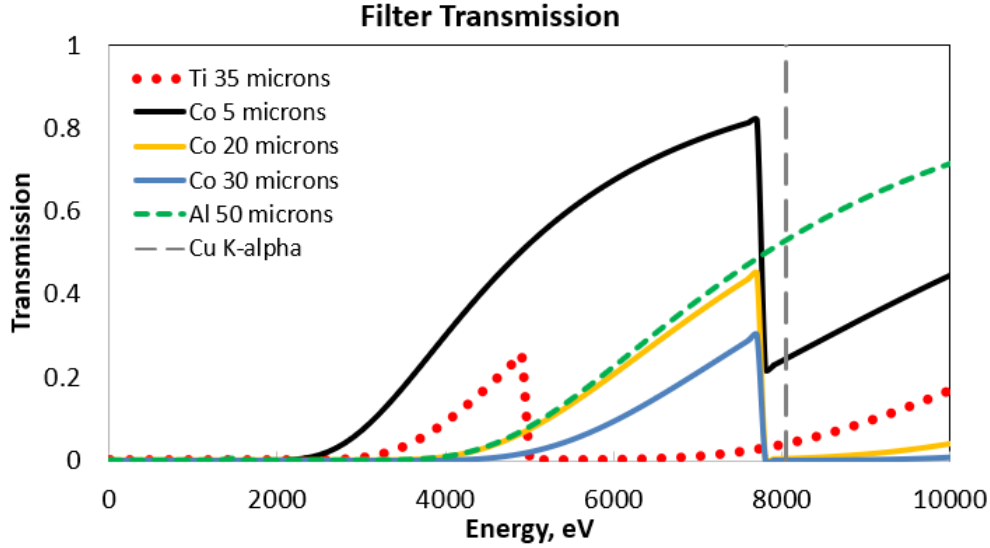


Figure 5.11: The transmission of several foil filters: Ti of 30 microns (dotted red), Co of 5 μm (solid black), Co of 20 μm (solid yellow), Co of 30 μm (solid blue), and Al of 50 μm (dashed green). The Cu-K α at 8050 eV (dotted gray) is also drawn as a reference.

The Cu-K α line is also explicitly presented in Fig. 5.11 at 8050 eV. This is important because it has been widely observed that in a plasma pinch, the interaction of the electrons in the post-pinch phase with the electrodes (particularly with the anode surface that is a copper material) contributes up to 95% of the total emission of the x-rays that is detected. This has been confirmed using a set of nickel and cobalt filters such that the Cu-K α line radiation lies between the K-absorption edges of nickel and cobalt (i.e., the impurity line radiation can be transmitted through a nickel filter, however, discriminated in a cobalt filter).

A BPX-65 photodiode detector has been implemented and attached to the DPF device for the detection of SXR. The sensitivity of the silicon-type PIN photodiode model is calculated using the thicknesses of intrinsic (0.5 μm) and active (10 μm) silicon layers, and plotted in Fig. 5.12. The BPX-65 model has been chosen because it has a spectral sensitivity in the SXR energy range of around 0.5 to 10 keV, which accounts for the argon x-ray emission.

As expected, the sensitivity drastically drops at shorter wavelengths since the x-rays simply pass through the intrinsic layer of the PIN photodiode without being absorbed. Likewise, a decrease in sensitivity is expected as the wavelength increases since the x-rays

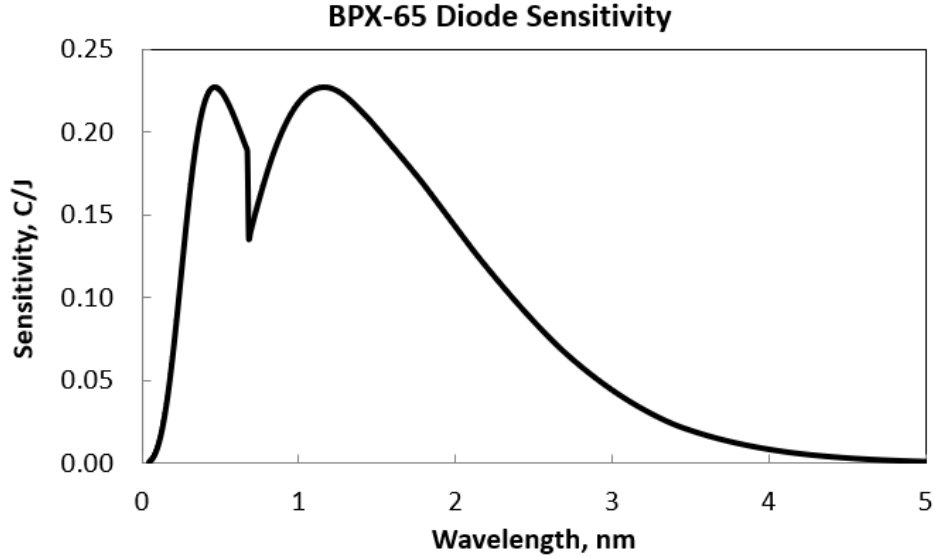


Figure 5.12: The calculated BPX-65 Si-PIN photodiode sensitivity with the thickness of the intrinsic and the active layers of the photodiodes are $0.5 \mu\text{m}$ and $10 \mu\text{m}$, respectively.

are absorbed by the silicon entrance layer. It can also be observed that a drop in sensitivity occurs at around 0.673 nm , which is due to the property of resonance absorption edge of the silicon layer.

The transmission of several foil filters (Fig. 5.11) are combined (or “folded”, from nomenclature) with the sensitivity of the silicon PIN photodiodes (Fig. 5.12), giving the response of the BPX-65 detector. The response of the detector, including the filters, as a function of x-ray energy is presented in Fig. 5.13.

This set of cobalt filters and the BPX-65 detector with silicon-PIN photodiodes are well suited for argon electron temperature measurements because one aims to measure x-rays in the range of 3 keV to 7.7 keV to significantly discriminate the copper impurity line radiation at an energy of 8.05 keV .

The x-ray spectrum is dependent on temperature and can be incorporated in the instrument response for calculating the ratios as a function of electron temperature. An example of the argon spectrum fixed at 6 keV is shown on Fig. 5.14.

The spectrum in Figure 5.14 was obtained from the NIST site [57] and calculated at an electron density of 10^{18} cm^{-3} that is typical and assumed for the size and parameters of the

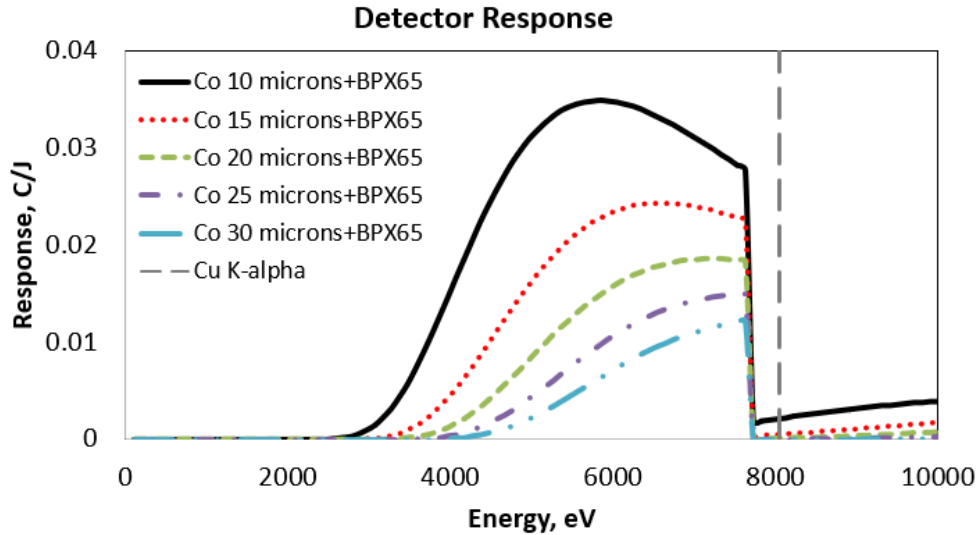


Figure 5.13: The calculated response of the detector as a function of energy: Co of 10 μm with BPX-65 (solid black), Co of 15 μm with BPX-65 (dotted red), Co of 20 μm with BPX-65 (dashed green), Co of 25 μm with BPX-65 (dashed violet), Co of 30 μm with BPX-65 (dashed blue), and the Cu-K alpha line (dotted gray).

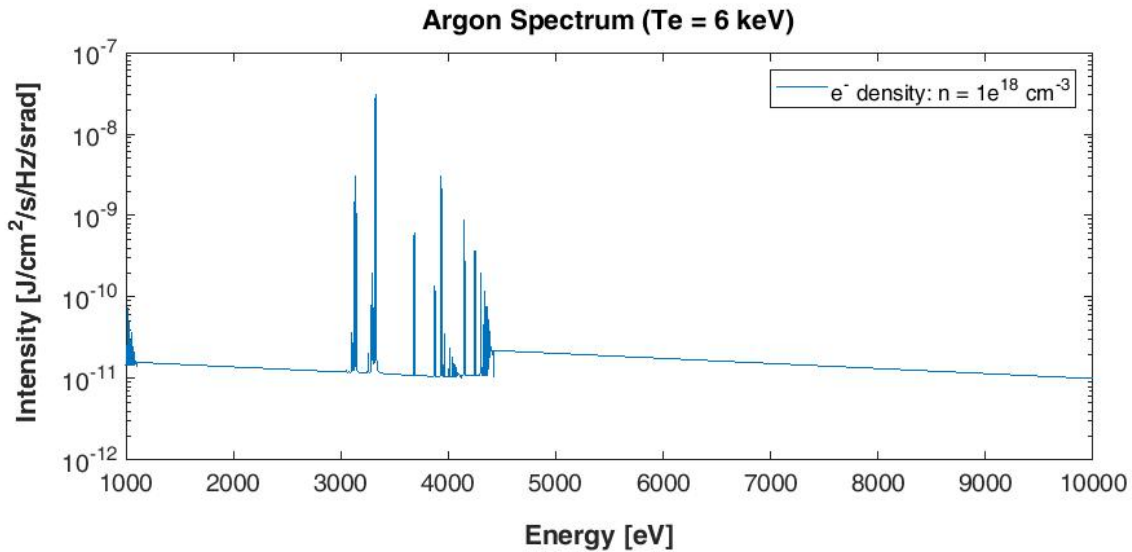


Figure 5.14: Argon spectrum at electron density of 10^{18} cm^{-3} and electron temperature of 6 keV. The spectrum is obtained based on calculation from the NIST site [57].

UofS-I DPF. It can be seen that the line emission spectrum in the range 3 - 4.5 keV may have some effects on the accuracy of the temperature measurement. Quantitative assessment on the effect is difficult without knowing the Bremsstrahlung emissivity in relation to that of line emission.

The ratios can be calculated at fixed temperatures ranging from 3 to 7 keV as a function of filter thickness. A plot of these ratios is shown on Fig. 5.15. This plot serves as a calibration curve for the experimental ratios of SXR intensities based on the selected filter thicknesses.

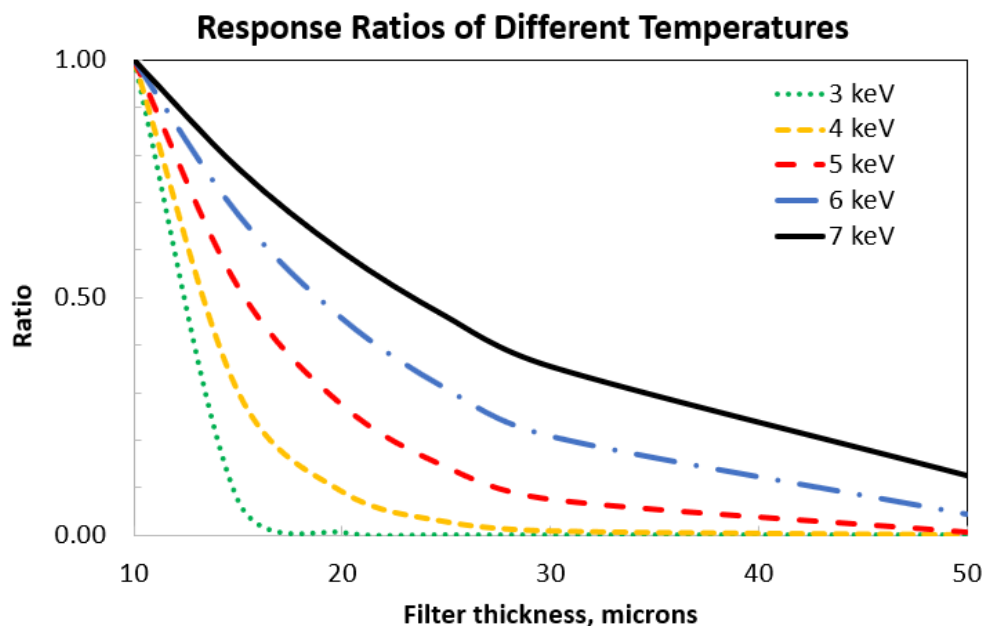


Figure 5.15: Ratio of response as a function of cobalt filter thickness for various temperatures: 3 keV (dotted green), 4 keV (dashed yellow), 5 keV (dashed red), 6 keV (dash-dot blue), and 7 keV (solid black). The reference filter thickness is 10 μm cobalt.

As expected, the temperature increases as the ratio increases. It is also worthy to note that the use of a 5 μm cobalt filter as a reference (as initially designed) may not give accurate results because it allows some x-ray transmission in the copper $K\alpha$ range (see Fig. 5.11). Therefore, the 10 μm thickness has been chosen as a reference filter so that the copper impurity line is almost totally absorbed.

Figure 5.16 shows the SXR signals obtained through the different cobalt filters (10 μm , 15 μm , 20 μm , 25 μm , and 30 μm).

Figure 5.16 (a) shows the plot of SXRs at $p_0 = 100$ mTorr. It also shows the differences in intensities of the detected SXR signals using the 10 μm , 15 μm , and 20 μm cobalt filters. As shown, the 15 μm and 20 μm cobalt filters are 51% and 30% of the 10 μm cobalt reference filter, respectively.

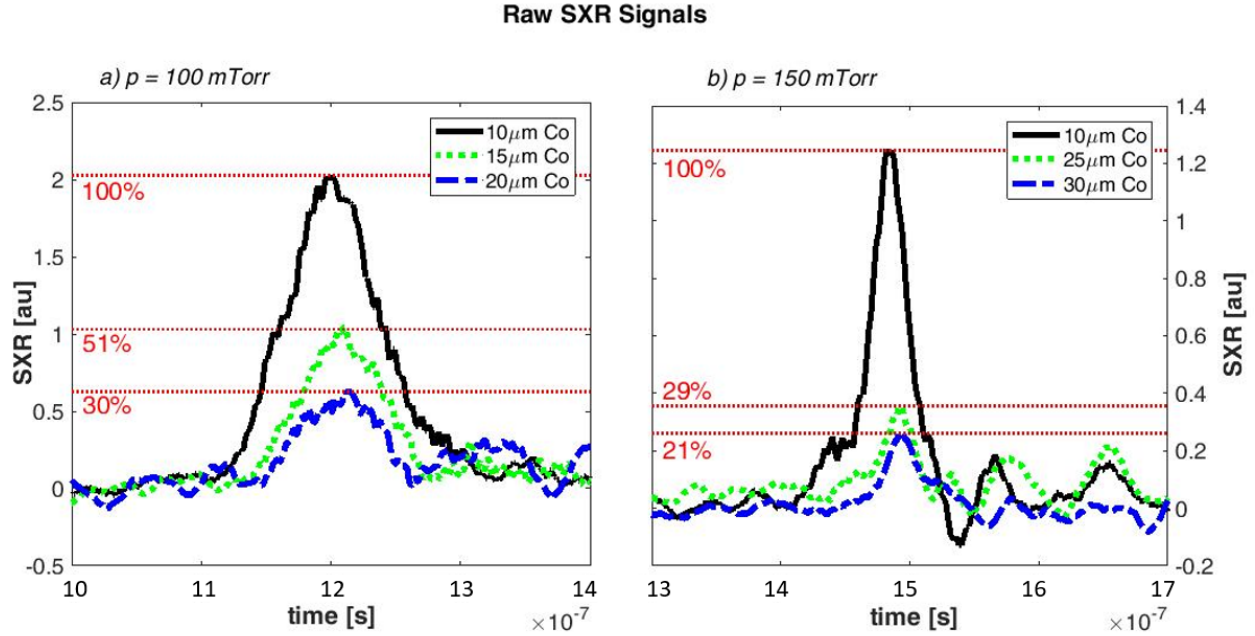


Figure 5.16: SXR signals measured from Si-PIN BPX-65 detectors through different cobalt foil filters. Shot (a) at $p_0 = 100$ mTorr shows the measured intensities through 3 filters: Co $10 \mu\text{m}$ reference (black), Co $15 \mu\text{m}$ (green), and Co $20 \mu\text{m}$ (blue). Shot (b) at $p_0 = 130$ mTorr shows the measured intensities through the same filters: Co $10 \mu\text{m}$ reference (black), Co $25 \mu\text{m}$ (green), and Co $30 \mu\text{m}$ (blue). The percentage of intensities are labelled with respect to the reference intensity from the Co $10 \mu\text{m}$ reference. The pinch time shift is caused by the difference in operating gas pressure.

Likewise, Fig. 5.16 (b) shows the plot of SXR signals at $p_0 = 150$ mTorr and the percent differences in intensities (also relative to the $10 \mu\text{m}$ cobalt reference filter) of 29% and 21% for the $25 \mu\text{m}$ and $30 \mu\text{m}$ cobalt filters, respectively. It is also good to note that the SXR signals were obtained at different run times. Nevertheless, it has been considered that since these signals were not taken simultaneously (i.e., not coming from the same SXR radiation source), several shots were taken while maintaining all the device parameters and conditions the same throughout the experiment.

Moreover, it can be observed that there lies a slight peak time difference between these signals (plot (a) vs. plot (b)). The differences in peak times are due to the pinch time of the shot, which is highly dependent on the operating pressure. Thus, operating with a range of pressures can cause inconsistent peak times for SXR signals.

Figure 5.17 shows the curves of the ratios of intensities as a function of cobalt foil filter thickness for various temperatures. Superimposed on this calibration curve are the ratios calculated based on experimental measurement of intensities of SXR at different cobalt filter thicknesses. Around 50 good discharges were collected and used to extract an average temperature.

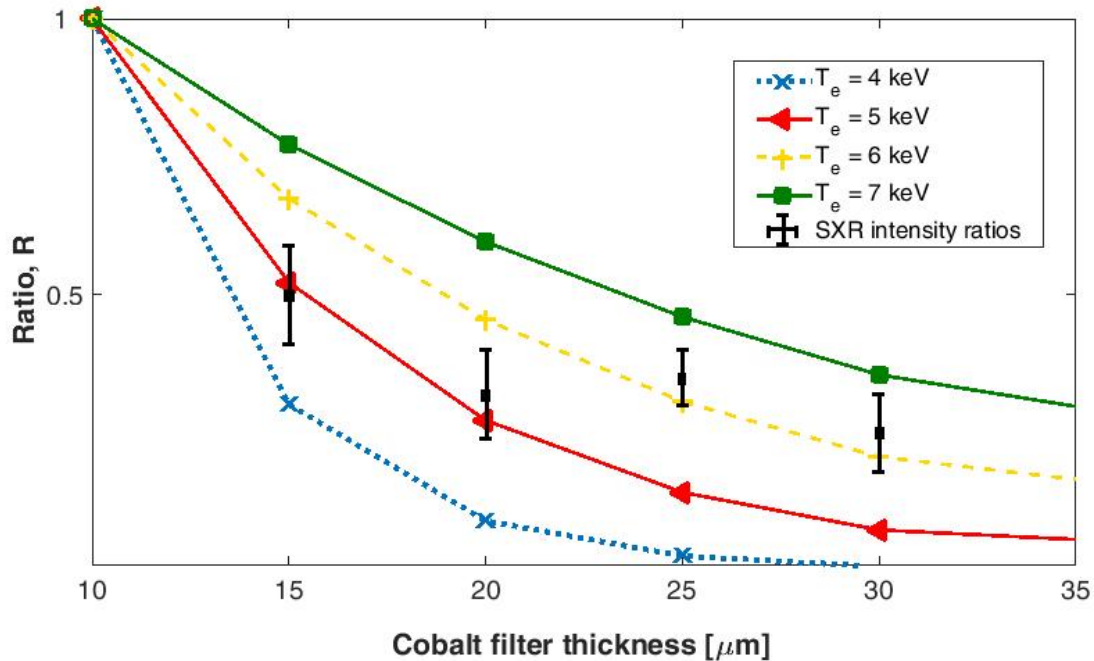


Figure 5.17: Ratio of experimental SXR intensities superimposed on the calibration curve. An electron temperature can be interpreted to fall in the range of 5.5 keV to 7.5 keV. An electron temperature average of 4.7 keV, 5.2 keV, 6.2 keV, and 6.1 keV were obtained from the Co 15 μm , 20 μm , 25 μm , and 30 μm , respectively. Based on data collected from 50 good discharges, the measured electron temperature is 5.7 ± 0.7 keV.

Through interpolation, the UofS-I DPF device operated at $V_0 = 20$ kV in argon gas at $p_0 = 100 - 200$ mTorr achieves an electron temperature ranging from 5.5 - 7.5 keV. Ten best shots per filter thickness were recorded at different times, but at constant parameters and conditions.

Table 5.1 shows a summary of the data on Fig. 5.17. Using the 10 μm cobalt filter as reference for the ratios of the different cobalt foil filter thicknesses, an overall average electron temperature of 5.7 ± 0.7 keV was obtained.

Table 5.1: Summary of ratios and corresponding interpolated temperatures for different cobalt foil filter thicknesses. Electron temperatures range from a minimum of 4.35 keV and a maximum of 6.6 keV. An overall average for the electron temperature is 5.7 ± 0.7 keV.

Cobalt Filter Thickness [μm]	Intensity Ratio, R [%]	Electron Temperature, T_e [keV]
10	100	(reference)
15	49	4.9 ± 0.5
20	32	5.2 ± 0.4
25	36	6.3 ± 0.3
30	24	6.3 ± 0.4
$T_{e,Average}$		(5.7 ± 0.7)

Preliminary experimental data suggest that higher anode voltages result in higher SXR intensities, and thus higher electron temperatures. In the following subsections, the inter-correlation among the measured electron temperature and other measured parameters such as: the anode voltage, the current dip, the intensities of emitted soft and hard x-ray, and the charge particles, will be discussed.

5.4 Correlation of DPF Properties with the Anode Voltage

The anode voltage has been used as basis for good focusing of the plasma. It has been observed that as the peak anode voltage increases, the current dip and the intensities of the charged particles and x-ray emissions also increase. The anode voltage signal has been recorded simultaneously with the other signals (discharge current, electron and ion beams, and SXR and HXR), and is compared to the other signals.

The signals were recorded simultaneously using the following fixed parameters: charging voltage of 20 kV, and operating pressure of 100 - 200 mTorr argon gas.

A typical signal of the anode voltage and the discharge current waveform from the same shot is presented in Fig. 5.18.

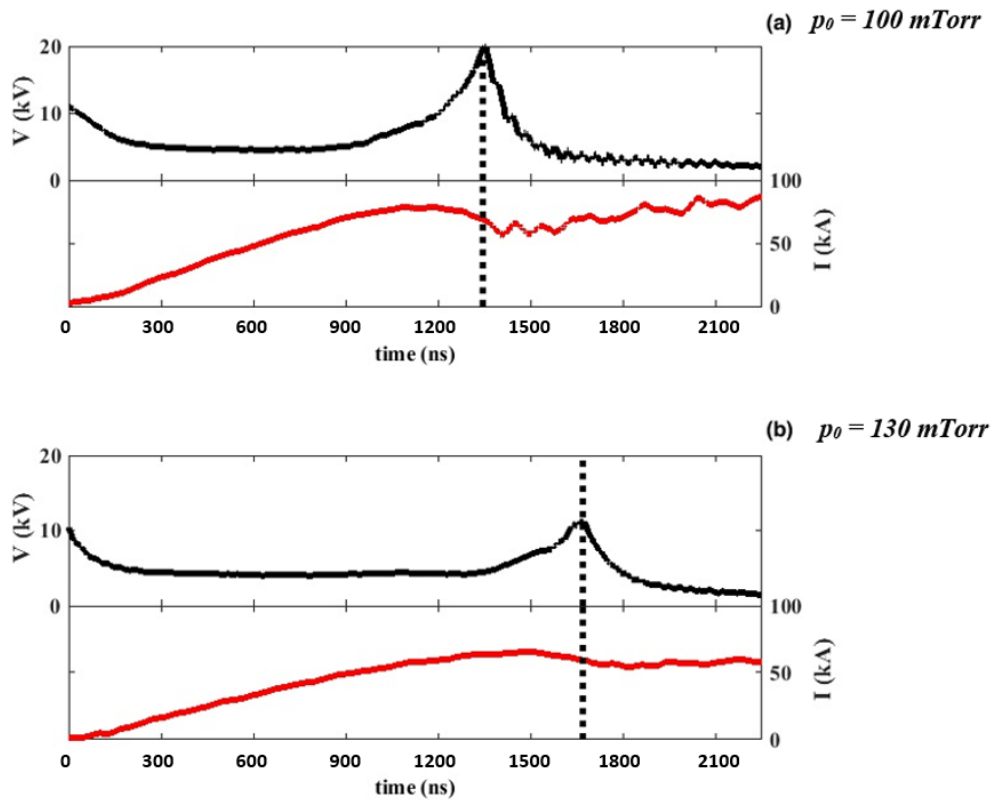


Figure 5.18: Anode voltage (in black) and Pearson Rogowski coil signal (in red) for shot (a) at $p_0 = 100$ mTorr and shot (b) at $p_0 = 130$ mTorr. The vertical dashed lines indicate the plasma pinch times, which correspond to the voltage peak and the current dip. The shift in pinch time is due to the difference in operating pressure.

Figure 5.18 (a) refers to a shot with an operating pressure of 100 mTorr and Fig. 5.18 (b) to a shot with an operating pressure of 130 mTorr. Shot (a) has a significantly higher peak anode voltage of 20 kV and a current dip of 25 kA versus shot (b) which only has 12 kV and 6 kA for the peak anode voltage and current dip, respectively. As can be seen, a higher discharge current dip corresponds to a higher peak voltage.

For the UofS-I DPF device, the typical voltage spike reaches up to 20 kV at around 1.3 μs (for an operating pressure of 100 mTorr), which correspond to the maximum compression time of the plasma. At the same time, the discharge current dips due to the dynamic resistance. At this time, the pinch phase has started. The typical discharge current rise time is 1.2 μs with a current dip of around 25 kA.

According to the Lee code, the current dip is highly dependent on the static inductance, L_0 , of the device. In fact, a way to optimize the device is to decrease the static inductance. Decreasing the inductance results in a significant increase in current dip and the emission of x-rays [58]. Thus, a low inductance is highly desirable especially in the production of x-rays in DPF devices. Since the current dip is dependent on the inductance, the current dip must also depend on the anode voltage.

Figure 5.19 shows the relationship between the peak voltage and the current dip of 25 different shots at fixed parameters. The plot suggests a linear correlation between the discharge current dip and the peak anode voltage.

The signals of the intensities of the charged particles have also been recorded. A hollow anode has been implemented to allow the electron beam to traverse axially through the bore at the center of the inner electrode to a collector that is grounded. The recorded electron beam signals using a Pearson Rogowski coil reflects the number of electrons that reach the collector.

Typical electron beam signals as a function of the anode voltage are presented in Fig. 5.20. As expected based on the DPF dynamics, electron beams are emitted in the unstable phase right after the pinch phase.

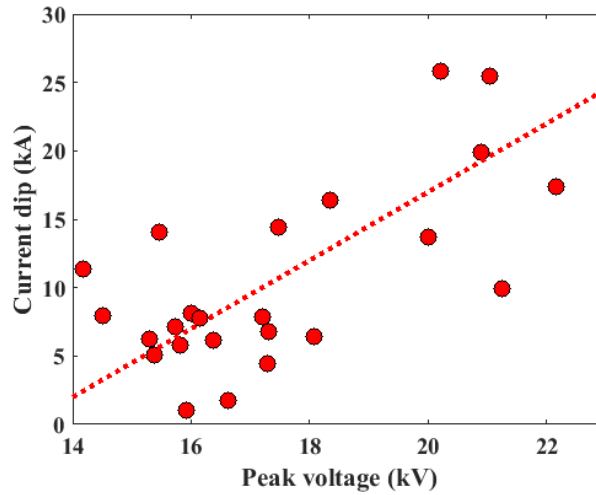


Figure 5.19: Correlation of the discharge current dip and the peak anode voltage of different shots at fixed running parameters of 20 kV charging voltage and 100-200 mTorr argon gas. A linear trend between the discharge current dip and the peak anode voltage can be observed (dashed red).

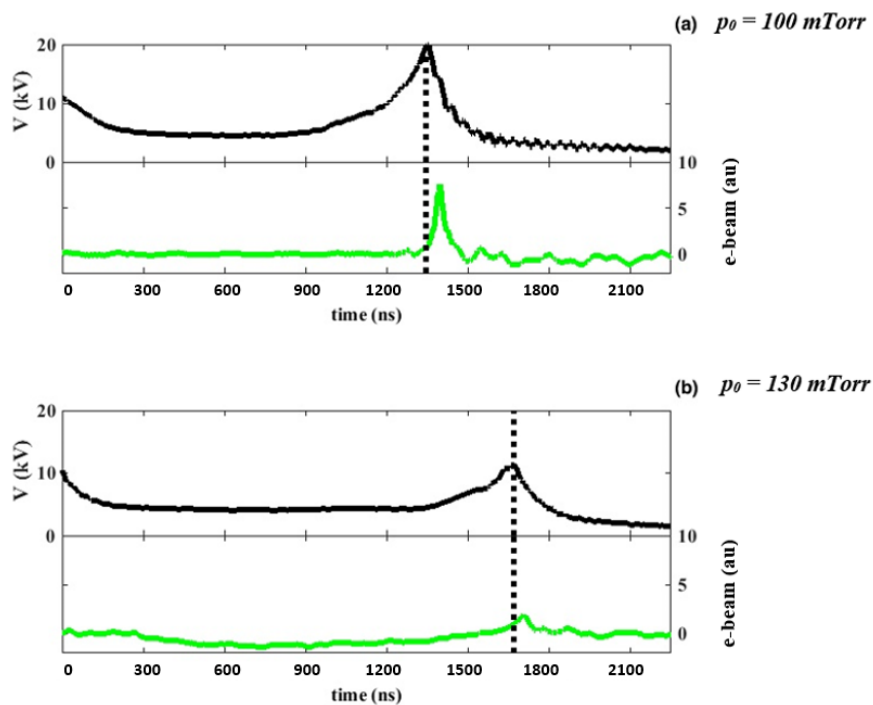


Figure 5.20: Anode voltage (in black) and electron beam signal (in green) for shot (a) at $p_0 = 100$ mTorr and shot (b) at $p_0 = 130$ mTorr. Dashed lines indicate the plasma pinch time which correspond to the voltage peak. A time delay between the pinch time and the electron beam peak is around 60 ns for both operating pressures.

The electron beam signals have a relatively quick rise time of around 100 ns, and a delay time from the pinch phase of around 60 ns. Electrons start to arrive at the charge collector right after the pinch phase. It can also be observed that an increase in the peak anode voltage results in an increase in the electron beam intensity.

Similarly, the waveforms of the Faraday cup signals are presented in Fig. 5.21 together with their corresponding anode voltage signals for two operating pressures.

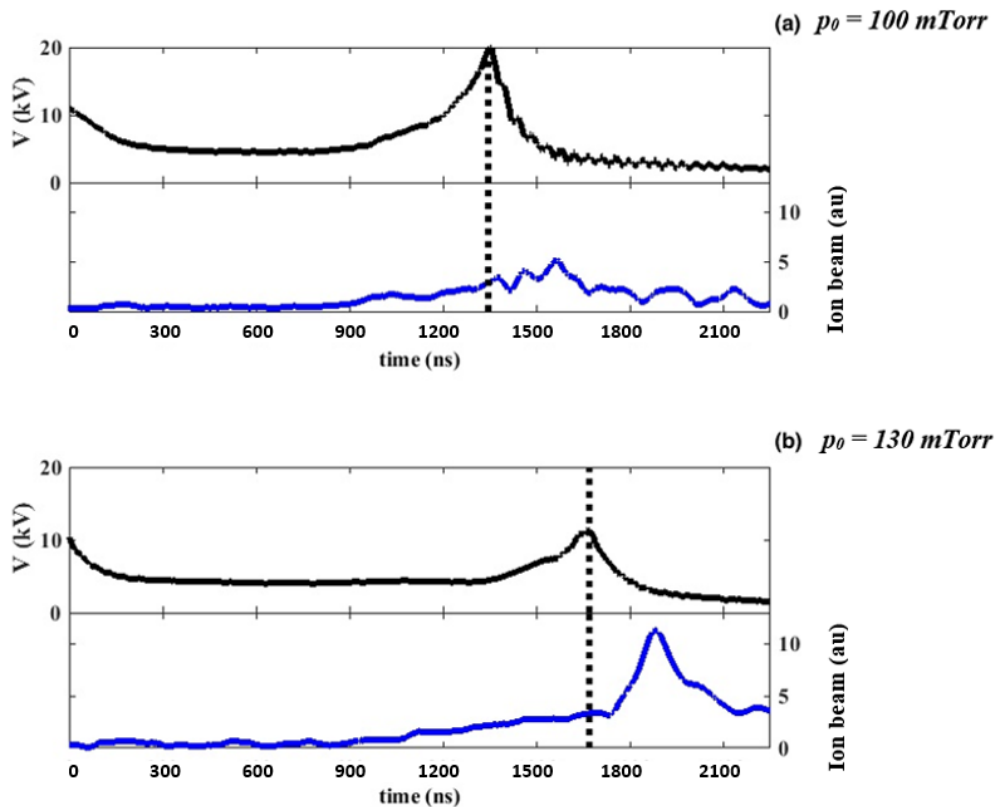


Figure 5.21: Anode voltage (in black) and Faraday cup signal (in blue) for shot (a) at $p_0 = 100$ mTorr and shot (b) at $p_0 = 130$ mTorr. Dashed lines indicate the plasma pinch time which correspond to the voltage peak. A time delay between the pinch time and the ion beam peak is observed to be around 300 ns for both operating pressures.

The ion beam signals start to increase at a time well before the voltage peak. The rise time is as long as 900 ns, and the delay time from the pinch is about 300 ns. The Faraday cup signal suggests that the ions start to be produced during the axial acceleration phase at around 900 ns from the breakdown phase. Contrary to the electron beam, the ion beam does not increase with the anode voltage. It can be seen on Fig. 5.21 that the ion beam

intensity of a lower anode voltage for shot (b) is about three times higher than that for shot (a) with about twice the anode voltage.

The delay of the peak and the waveform of the ion beam signal with respect to the SXR peak are often used to estimate the energy distribution of the ion beam based on time-of-flight method.

It is known that an increase in voltage results in an increase in the velocity of the electron beam, and thus, the energy of the electron beam. Since the electron beam intensity is proportional to the number of electrons arriving at the charge collector, an increase in voltage should result in an increase in electron beam intensity if the density remains the same.

Figure 5.22 shows the correlation of the peaks of the charged particles with the peak anode voltage for both electrons and ions.

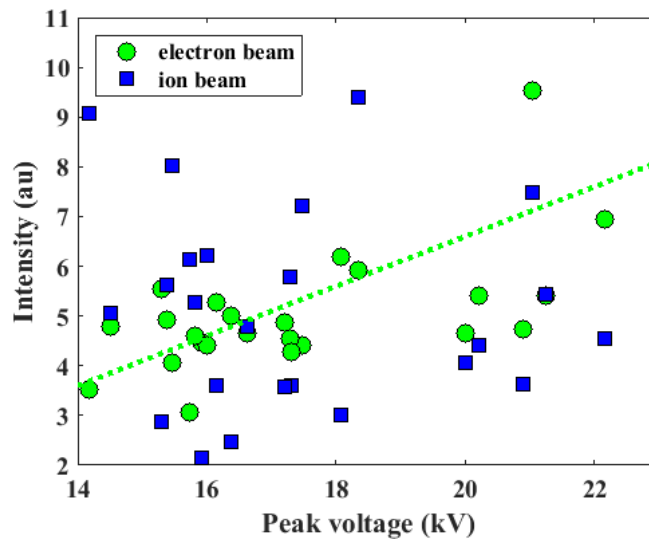


Figure 5.22: Correlation of the electron beam (green circles) and ion beam (blue squares) intensities and the peak anode voltage of a collection of shots at fixed running parameters (20 kV charging voltage and 100-200 mTorr argon gas). A linear trend between the electron beam intensity and the peak voltage can be observed (dashed green). No apparent correlation for the ion beam intensity can be observed.

The peaks of the electron beam suggest a strong linear correlation with the peak voltage, whereas the peaks of the ion beam suggest otherwise. A random scatter of data from the

ion beam intensities and voltage peaks is apparent, thus, no correlation can be deduced for this case.

The x-ray radiations from the UofS-I DPF plasma have also been concurrently measured. Figure 5.23 shows the typical SXR signals along with their corresponding anode voltage signals.

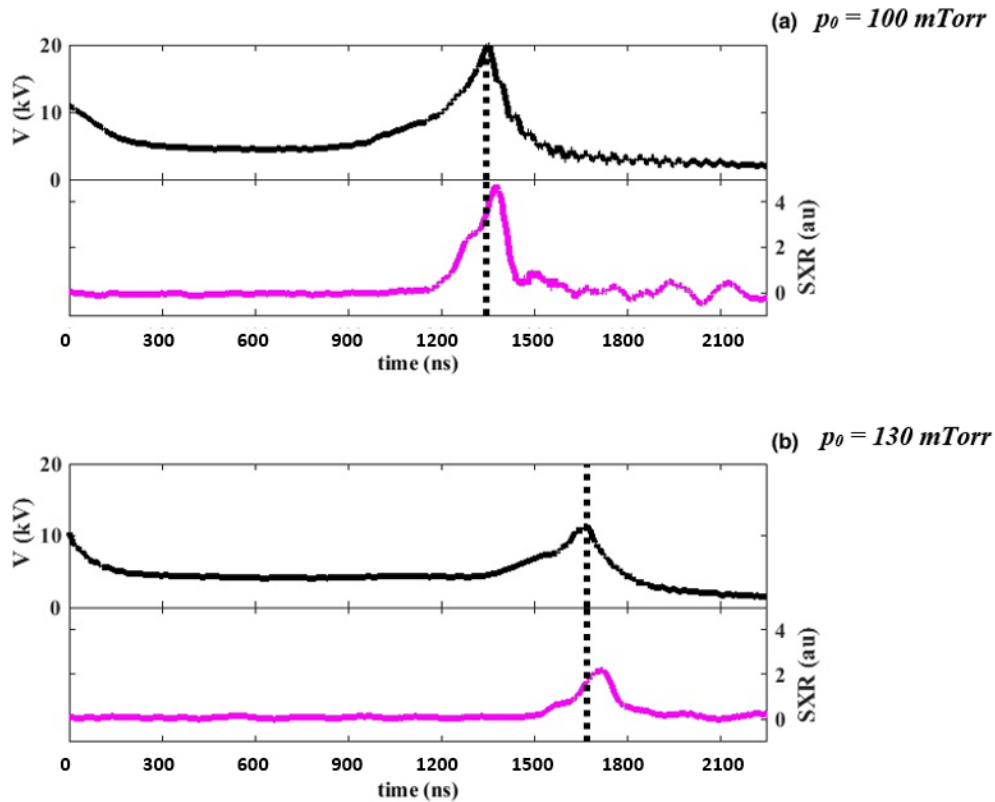


Figure 5.23: Anode voltage (in black) and BPX-65 photodiode signal (in magenta) for shot (a) at $p_0 = 100 \text{ mTorr}$ and shot (b) at $p_0 = 130 \text{ mTorr}$. Dashed lines indicate the plasma pinch time which correspond to the voltage peak. A time delay between the pinch time and the SXR peak is observed to be around 30 ns for both operating pressures.

The rise time for the SXR is around 200 ns, and a delay time between the the SXR peak and the pinch time is around 30 ns. This agrees with the expectation based on the DPF dynamics that x-rays are emitted during the decay phase that is right after the unstable phase. It can also be easily observed that the peak of the SXR intensity increases with the peak anode voltage.

On the other hand, typical hard x-ray signals are presented in Fig. 5.24 along with their

corresponding anode voltages.

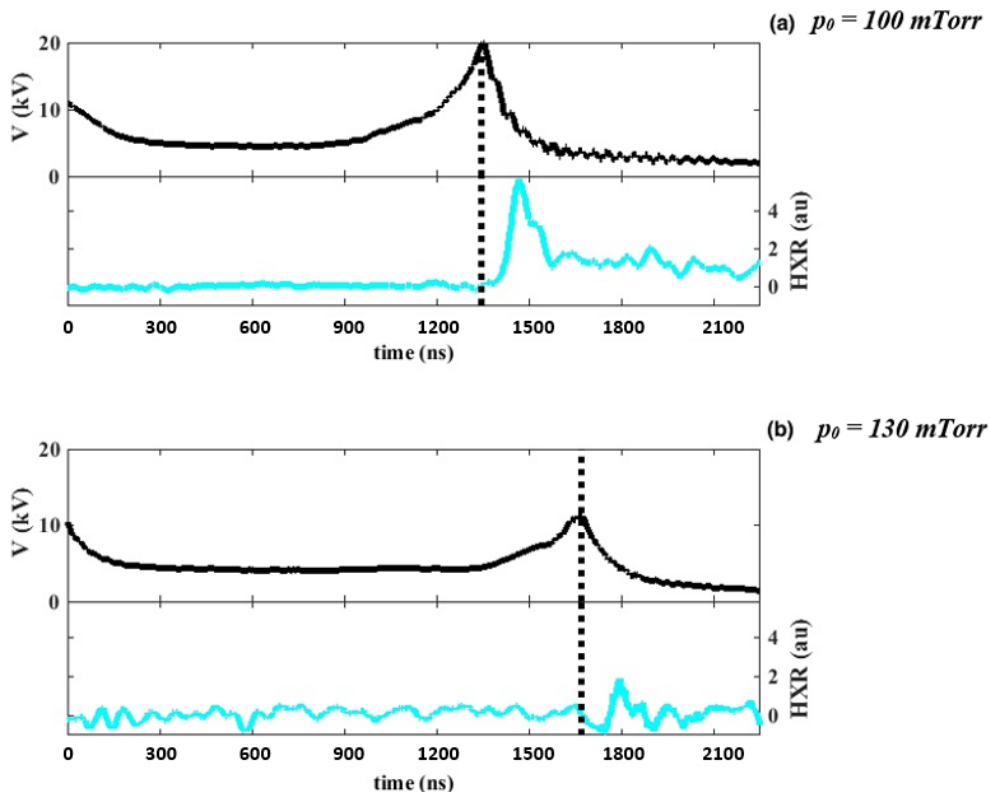


Figure 5.24: Anode voltage (in black) and HXR (in blue) for shot (a) at $p_0 = 100$ mTorr and shot (b) at $p_0 = 130$ mTorr. Dashed lines indicate the plasma pinch time which correspond to the voltage peak. A time delay between the HXR peak and the pinch time is about 120 ns for both operating pressures.

In contrast, the HXR delay time from the pinch is significantly longer compared to that of SXR. The HXR delay time averages up to about four times longer, however, with a rise time of five times shorter than that of the SXR. The longer delay time from the pinch suggests that the emission of HXRs occur in the far end of the decay phase when copious amounts of Bremsstrahlung radiation are emitted from the plasma cloud.

The total x-ray intensity that is released in a time interval is known to be proportional to the atomic number of the target, Z , and the accelerating voltage, V . Therefore, using argon gas (which has a higher atomic number compared to N or H, for example) in the DPF device, and a higher voltage in the anode theoretically result in higher x-ray emission intensities.

Furthermore, the number of electrons that impinge a target surface (the copper anode,

for example) is related to the voltage between the electrodes [61]. Therefore, a higher anode voltage must result in an increase in the number of electron collisions, and in turn, an increase in x-ray intensity.

The correlation between the anode voltage peak with the intensities of the soft and hard x-rays are presented in Fig. 5.25.

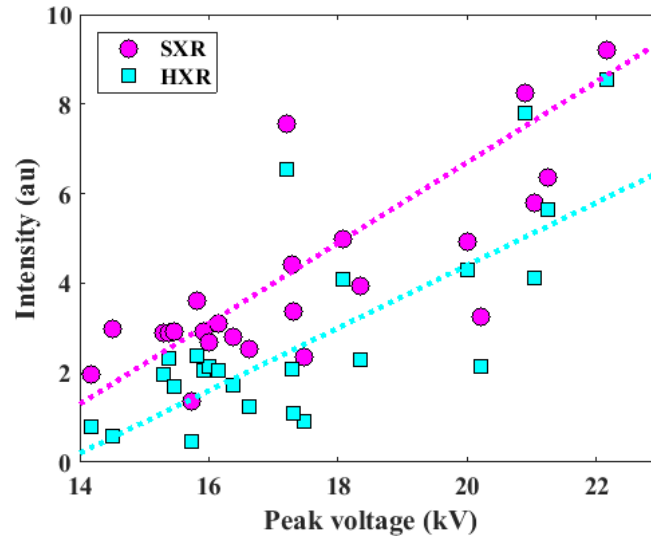


Figure 5.25: Correlation of the soft x-ray (magenta circles) and hard x-ray (blue squares) intensities and the peak anode voltage of different shots at fixed running parameters of 20 kV charging voltage and 100-200 mTorr argon gas. A linear trend for the soft x-rays and hard x-rays with the peak voltage can be observed (dashed magenta and blue, respectively).

It can be observed that, for both cases, the intensity of the x-rays increases up to 8 times with an increase of around 8 kV of anode voltage (from 14 kV to 22 kV). Similarly, the trend of increase with the peak anode voltage is almost linear for both cases. Thus, by simply doubling the peak anode voltage, the intensities of x-rays can be significantly increased up to a factor of 8.

Furthermore, it is also known that the number of electrons in the electron beam is directly proportional to the number of x-rays that is generated. Thus, since an increase in voltage resulted in an increase in x-ray intensity, an increase in voltage must also result in an increase in electron beam intensity. This agrees with the correlation of the anode voltage and the electron beam intensity in Fig. 5.22.

As a summary, the correlations of intensities between the peak anode voltage and the electron beam and x-ray radiation emissions have been found, and as observed in other experiments [61]. The data obtained are useful for enhancement and optimization of emission of charged particles [62] and x-ray emissions for their potential applications in applied science and technology.

5.5 Correlation of DPF Properties with the Electron Temperature

It is evident from the previous section that the intensities of the electron beam and the x-rays are correlated with the anode voltage. Thus, if the anode voltage is correlated with the electron temperature, it can be deduced indirectly that the current dip, the electron beam and the x-ray radiation emissions must also be correlated with the electron temperature.

Figure 5.26 shows the the almost-linear correlation between the anode voltage and the measured electron temperatures. The anode voltage, the current dip, the electron beam and the SXR and HXR emission intensities also show a linear correlation with the measured electron temperature. Similar to the anode voltage, no correlation between the intensities of the ion beam and the other signals can be observed.

The correlations with electron temperatures are of great importance concerning hot-spots formed in the DPF plasmas. Due to magneto-hydrodynamic instabilities ($m = 0$), localized plasma regions of small dimensions with high electron concentrations are formed. The studies of L. Jakubowski *et al.* were concerned with the formation of micro-regions (or so-called “hot-spots”) where the electron concentration is very high. Consequently, the electron temperatures are relatively higher than others in these regions. They have also identified that these hot-spots are the sources of intense x-ray emissions as well as the pulsed electron and ion beams [63]. Ultimately, they have found that the values of local electron temperatures were higher when the observed hot-spots were situated close together in time and space. Therefore, it has been suspected that a wide range of electron temperatures can be estimated due to the occurrence of hot-spots. These hot-spots hold a stochastic character,

which greatly affects the preciseness of experimental data [63,64]. Nonetheless, correlations of the electron beam and x-ray emissions with the electron temperature have been found, which likely is due to the occurrence of magneto-hydrodynamic instabilities. Further study incorporating a pin-hole camera [44] is necessary to directly verify the dependence of electron temperature to hot-spots.

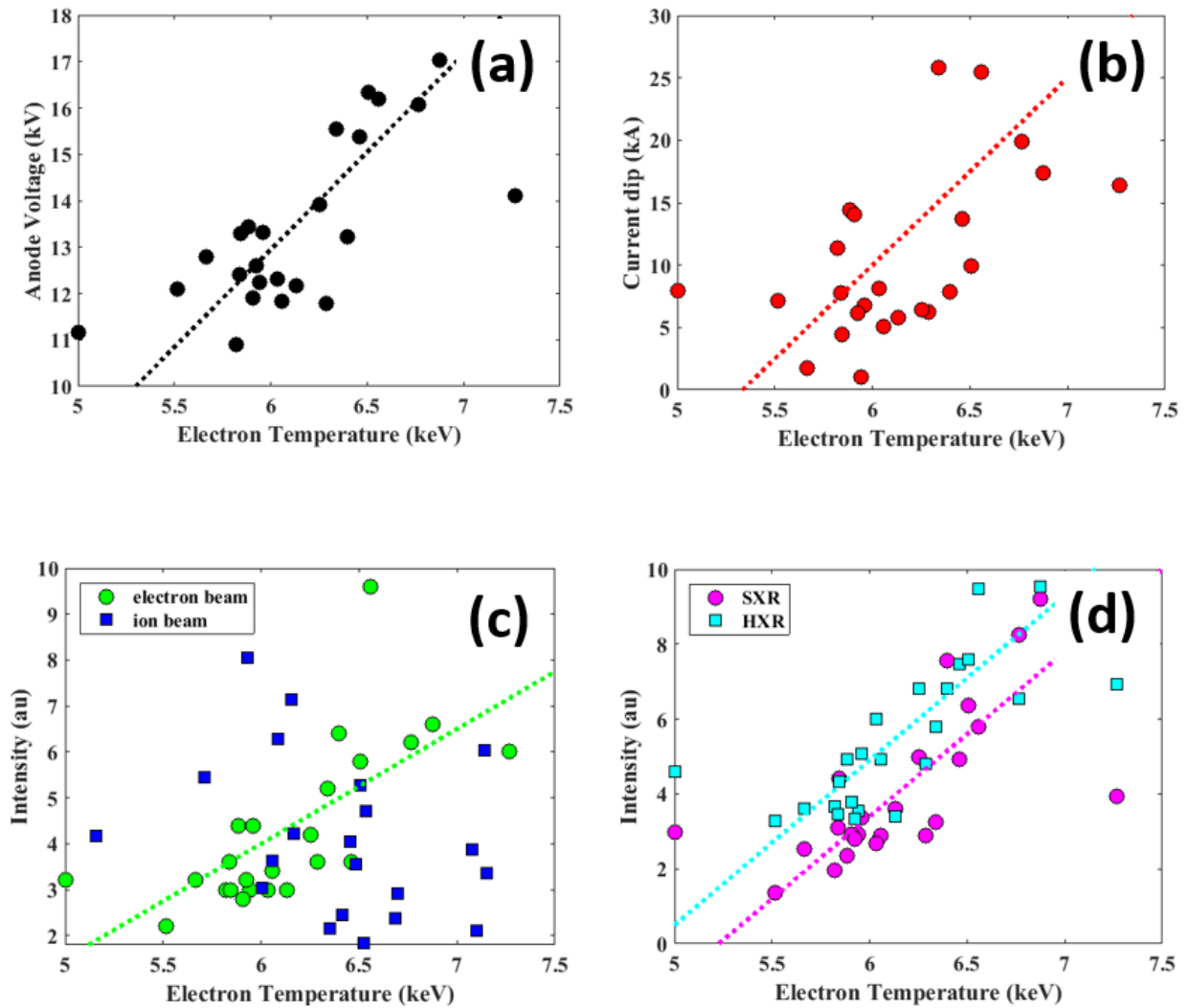


Figure 5.26: Correlations with the electron temperature: (a) A linear correlation between the anode voltage (in black) and the electron temperature; (b) a linear correlation between the current dip (in red) and the electron temperature; (c) a linear correlation between the electron beam (in green) and the electron temperature, no correlation with the ion beam (in dark blue); and (d) a linear correlation between the SXR (in magenta) and HXR (in blue) with the electron temperature.

Chapter 6

Summary and Suggested Future Work

The UofS-I DPF, a 1 kJ Mather-type dense plasma focus device powered by a 5 μF capacitor bank with a charging voltage of 20 kV and an optimized operating pressure range of 100 - 200 mTorr of argon, has been used to study the features of plasma dynamics. A hollow copper anode has been implemented to allow electron beam emission detection and to minimize copper impurity line radiation.

The following signals of interest have been measured using different techniques: the discharge current waveform using a Pearson Rogowski coil, the anode voltage using a fast Tektronix P6015a high-voltage probe, the electron beam using an electron collector and a Pearson Rogowski coil, the ion beam using a Faraday cup, the soft x-ray using a BPX-65 PIN photodiode array, and the hard x-ray using a PMT-scintillator detector. The signals have been recorded simultaneously using Tektronix TDS 2024c oscilloscopes.

In the UofS-I DPF, the axial acceleration phase duration has been found to be 1.15 μs and the radial compression phase duration is 400 ns. These time durations agree with other comparatively small DPF devices [60]. The pinch phase occurs typically at around 1.55 μs from the start of the capacitor discharge. The waveforms of the emission of charged particles and x-ray radiations relative to the focusing event (pinch phase) have also been compared. Time delays of the peaks of the signals after the pinch time have been found to be around 30 ns, 60 ns, 120 ns, and 300 ns for the SXR, electron beam, HXR, and ion beam, respectively.

The Lee model code has been used to extract information regarding the optimization of the charging voltage and the operating pressure for the UofS-I DPF device. Moreover, it has been used for fitting of the experimental current waveform with the calculated current waveform to obtain the mass and current factors. These factors allow the calculation of the

radial positions and speeds of the focusing plasma. A static inductance value from a short-circuit RLC waveform has been calculated to be $L_0 = 150$ nH. Model parameters (mass, current and their factors) of $massf = 0.046$, $currf = 0.7$, $massfr = 0.31$, and $currfr = 0.7$ have been determined through a good fit of the experimental current waveform. The dependence of the current dip on the charging voltage and the operating pressure have been investigated through computations. As a result, an optimal charging voltage and operating pressure for argon gas have been determined to be $V_0 = 20$ kV and $p_0 = 150$ mTorr, respectively.

The electron temperature of argon plasma in the UofS-I DPF has been measured by implementation of a BPX-65 SXR detector and the application of the ratio method on SXR intensities. An array of BPX-65 silicon-PIN photodiodes with a set of cobalt foil filters of thicknesses ranging from 10 - 30 μm have been carefully selected based on the SXR energy range of argon plasma and the Cu-K impurity emission line. A calibration curve plotted as a function of filter thickness at different electron temperatures has been calculated for the SXR detector. The calculated ratios based on experimental SXR data have been superimposed on the calibration curve. The interpolation of experimental data based on the calibration curve results in an overall averaged electron temperature of 5.7 ± 0.7 keV for $p_0 = 100 - 200$ mTorr argon working gas during the post-pinch phase.

Correlations of the discharge current dip, the electron and ion beam intensities, and the SXR and HXR intensities with the anode voltage have been investigated. The peak anode voltage has been found to correlate linearly with the discharge current dip, the electron beam intensity, and the SXR and HXR intensities with the peak anode voltage. However, no clear correlation of the ion beam intensity with the rest of parameters have been found.

Similarly, the electron temperature has been found to correlate linearly with the anode voltage, the discharge current dip, the electron beam intensity, and the SXR and HXR intensities. Hot-spots due to magneto-hydrodynamic instabilities have been suspected to cause a large spread in the measured electron temperature. An implementation of a pin-hole

camera could be used to further study the formation and location of hot-spots as well as to give information regarding the time evolution and the formation of the pinching plasma.

Consequently, the lack of correlation of ion beam intensity needs to be studied. It is not clear whether this phenomenon is limited to the specific experimental conditions chosen in this set of experiments, or whether it is an intrinsic feature due to some unknown processes in the DPF. It is also important to find and control those mechanisms so that ion beams can be produced with consistent and controllable intensities.

DPFs are highly capable of producing neutrons [25]. Diagnostics in neutron production on DPFs are typically performed using deuterium gas based on D-D reactions. The emission of neutrons, thus, can be studied concurrently with the emission of charged particles and x-ray radiations. Moreover, the study on neutrons allow experimental verification of extensive theoretical works on scaling laws for building DPFs based on neutron yields and inductance values [58, 59].

The production of short-lived radioisotopes (SLRs) in DPFs can also be studied using deuterium gas with neutrons as a by-product [65]. The high-energy deuterons from the DPF can be used to produce ^{13}N SLRs, for example, by bombarding a graphite target based on the reaction: $^{12}\text{C} (d, n) ^{13}\text{N}$.

DPFs are good sources of ion and electron beams, and thus can be applied in the field of material processing [66, 67]. Films can be grown on substrates using the charged particles from a DPF, and the porosity and mechanical hardness of the treated surface layer at various axial positions relative to the focusing region can be studied through x-ray diffractometers (XRD) and field-emission scanning electron microscopy (SEM) [68].

The UofS-I DPF device has also been configured as a dual-stage pinch-accelerator [69]. The occurrence of several focusing events in this new Z-pinch structure have been observed. Further investigation with respect to charged-particle acceleration mechanisms, x-ray radiations, and neutron production from this innovative configuration may prove important.

References

- [1] M. Boulos, P. Fauchais, E. Pfender, “Thermal plasmas, fundamentals and applications”, vol. 1, *Plenum Press*, 1994.
- [2] F. F. Chen, “Introduction to Plasma Physics and Controlled Fusion”, *Springer Science and Business Media*, LLC, 2006.
- [3] N. Krall, A. Trivelpiece, “Principles of plasma physics”, *San Franc. Press Inc.*, 1986.
- [4] E. Skladnik-Sadowska, D. Zaloga, M. Sadowski, R. Kwiatkowski, K. Malinowski, R. Miklaszewski, M. Paduch, W. Surala, E. Zielinska, K. Tomaszewski, “Research on soft x-rays in high-current plasma focus discharges and estimation of plasma electron temperature”, *Plasm. Phys. and Controlled Fusion*, vol. 58, no. 9, pp. 1-10, 2016.
- [5] A. Fridman, L. Kennedy, “Plasma physics and engineering”, *Taylor & Francis Grp. Inc.*, 2004.
- [6] J. Freidberg, “Plasma physics and fusion energy”, *Cambridge Uni. Press*, 2007.
- [7] I. Wright, “Tokamak confinement of nuclear fusion plasma”, <https://www.engineering.com/DesignerEdge/DesignerEdgeArticles/ArticleID/10972/Plasma-Fusion-is-Heating-Up.aspx>. [Accessed: 01-Jun-2018].
- [8] J. A. Bittencourt, “Fundamentals of plasma physics”, *Springer-Verlag NY Inc.*, 2004.
- [9] E. A. Witalis, “Z-pinch dynamics from the generalized Bennett relation”, *Physical Rev. A*, vol. 10, no. 6, pp. 2373-2377, 1974.
- [10] S. Lee, S. Saw, “Numerical Experiments Providing New Insights into Plasma Focus Fusion Devices”, *Energies*, vol. 3, no. 4, pp. 711-737, 2010.
- [11] S. Lee, “Plasma radiative model: review of the lee model code”, *Journ. of Fusion Energy*, vol. 33, no. 4, pp. 319-335, 2014.

- [12] K. Hirano, T. Yamamoto, S. Takada, H. Sone, K. Shimada, “Production of highly charged metal ions and soft x-ray emission in a plasma focus”, *Japanese Journ. of Appl. Phys.*, vol. 27, no. 1, pp. 89-94, 1988.
- [13] V. Damideh, J. Ali, S. Saw, R. Rawat, P. Lee, K. Chaudhary, Z. Rizvi, S. Dabagh, F. Ismail, L. Sing, “Fast Faraday cup for fast ion beam TOF measurements in deuterium filled plasma focus device and correlation with Lee model”, *Phys. of Plasmas*, vol. 24, no. 6, pp. 1-5, 2017.
- [14] W. Harries, J. Lee, D. McFarland, “Trajectories of high energy electrons in a plasma focus”, *Plasma Phys.*, vol.20, no. 2, pp. 95-106, 1978.
- [15] J. Smith, C. Luo, “Operation of a plasma focus device as a compact electron accelerator”, *Phys. of Fluids*, vol. 28, no. 27, pp. 2305-2307, 1985.
- [16] “DPF compression”, <http://web.brasimone.enea.it/plasma/plasma1.htm>. [Accessed: 01-Dec-2015].
- [17] R. A. Behbahani, A. Hirose, C. Xiao, “Plasma heating and emission of runaway charged particles in a plasma focus device”, *Europhys. Lett.*, vol. 113, no. 5, pp. 1-5 2016.
- [18] M. Khan, L. Kim, S. Yap, C. Wong, “Imperative function of electron beams in low-energy plasma focus device”, *Pramana Journ. of Phys.*, Vol. 85, No. 6, pp. 1207-1219, 2015.
- [19] Z. Zakaullah, K. Alagmir, M. Shafiq, M. Sharif, A. Waheed, “Scope of plasma focus with argon as a soft x-ray source”, *IEEE Trans. On Plasma Sci.*, vol. 30, no. 6, pp. 2089-2094, 2002.
- [20] F. Beg, I. Ross, A. Lorenz, J. Worley, “Study of x-ray emission from a table top plasma focus and its application as an x-ray backlighter”, *Journ. Of Appl. Phys.*, vol. 88, no. 6, pp. 3225-3230, 2000.

- [21] M. Khan, Y. Ling, W. San, “Variation of radiation emission with argon gas pressure in UM plasma focus with hollow anode”, *Open Jour. of Appl. Sci.*, vol. 3, no. 2, pp. 194-201, 2013.
- [22] M. Akel, S. Salo, C. Wong, “Numerical study of radiation emission from the argon plasma focus”, *Journ. of Fusion Energy*, vol. 32, no. 2, pp. 242-246, 2013.
- [23] R. A. Behbahani, C. Xiao, “Common features of particle beams and x-rays generated in a low energy dense plasma focus device”, *Phys. of Plasmas*, vol. 22, no. 2, pp. 2-3, 2015.
- [24] F. Aghamir, R. Behbahani, “Energy spectrum of multi-radiation of x-rays in a low energy Mather-type plasma focus device”, *Chin. Phys. B.*, vol. 23, no. 6, pp.1-5, 2014.
- [25] M. Milanese, Niedbalski, M. Barbaglia, F. Castillo, S. Guichón, “Small plasma focus as neutron pulsed source for nuclides identification”, *Rev. of Sci. Instr.*, vol. 84, no. 10, pp. 1-3, 2013.
- [26] M. Hassan, A. Qayyum, R. Ahmad, R. S. Rawat, P. Lee, S. M. Hassan, G. Murtaza, M. Zakaullah, “Dense plasma focus ion-based titanium nitride coating on titanium”, *Nucl. Instr. and Methods in Phys. Res. B*, vol. 267, no. 11, pp. 1911-1917, 2009.
- [27] C. Kant, M. Srivasta, R. Rawat, “Dense plasma focus energetic ions based fullerene films on a Si (111) substrate”, *Phys. Lett. A*, vol. 239, no. 1, pp. 109-114, 1998.
- [28] H. Kelly, A. Lepone, A. Marquez, D. Lamas, C. Oviedo, “Coating on metallic samples produced by a small energy plasma focus”, *Plasma Sources Sci. and Tech.*, vol. 5, no. 704, pp. 704-709, 1996.
- [29] M. Asif, A. Ikram, “Electron temperature measurement using PIN diodes as detectors to record the x-ray pulses from a low-energy Mather-type plasma focus”, *Plasma Sci. and Tech.*, vol. 6, no. 2, pp.2199-2203, 2004.

- [30] L. Heroux, "A spectroscopic method of measuring electron temperatures in plasmas", *Nature*, vol. 198, no. 4887, pp. 1291-1293, 1963.
- [31] M. Khan, S. Yap, C. Wong, "Estimation of electron temperature and radiation emission of a low energy (2,2 kJ) plasma focus device", *Indian Journ. of Phys.*, vol. 88, no. 1, pp. 97-102, 2014.
- [32] M. Zakaullah, K. Alamgir, M. Shafiz, S. Hassan, G. Murtaza, A. Waheed, "Improved temperature measurement in a plasma focus by means of a cobalt filter", *Plasma Sources Sci. Tech.*, vol. 10, no. 2, pp. 295-301, 2001.
- [33] M. Akel, A. Salo, C. S. Wong, "Electron Temperature Measurement of Argon Focussed Plasma Based on Non-local Thermodynamic Equilibrium Model", *Journ. of Fusion Energy*, vol. 32, no. 3, pp. 350-354, 2013.
- [34] Y. Kato, I. Ochiai, Y. Wantanabe, S. Murayama, "Plasma focus x-ray source for lithography", *Journ. of Vacuum Sci. and Tech., Nanotech. and Microelectronics: Mat. Proc. Meas. and Phenomena*, vol. 6, no. 1, pp. 195-198, 1988.
- [35] Y. Kato, S. Be, "Generation of soft x rays using a rare gas-hydrogen plasma focus and its application to x-ray lithography", *Appl. Phys. Lett.*, vol. 48, no.11, pp. 686-688, 1986.
- [36] P. Lee, X. Feng, G. Zhang, M. Liu, S. Lee, "Electron lithography using a compact plasma focus", *Plasma Sources Sci. and Tech.*, vol. 6, no. 3, pp. 343-348, 1997.
- [37] R. Lebert, W. Neff, D. Rothweiler, "Pinch plasma source for x-ray microscopy with nanosecond exposure time", *Journ. of X-ray Sci. and Tech.*, vol. 6, no. 2, pp. 107-140, 1996.
- [38] S. Hussain, M. Shafiq, R. Ahmad, A. Waheed, M. Zakaullah, "Plasma focus as a possible x-ray source for radiography", *Plasma Sources Sci. and Tech.*, vol. 14, no. 1, pp. 61-69, 2005.

- [39] S. Lee, “Institute for Plasma Focus Studies”, <http://www.plasmafocus.net/>. [Accessed: 01-May-2015].
- [40] J. W. Mather, “Dense Plasma Focus”, *Methods in Exp. Phys.*, vol. 9, Part B, pp. 187-249, 1971.
- [41] N. V. Filippov, T. I. Filippova, M. A. Karakin, V. I. Krauz, V. P. Tykshaev, V. P. Vinogradov, Y. P. Bakulin, V. V. Timofeev, V. F. Zinchenko, J. R. Brzosko, J. S. Brzosko, “Filippov Type Plasma Focus as Intense Source of Hard X-Rays”, *IEEE Trans. on Plasma Sci.*, vol. 24, No. 4, pp. 1215-1223, 1996.
- [42] H. Bruzzone, D. Grondona, “Magnetic probe measurements of the initial phase in a plasma focus device”, *Plasma Phys. Control Fusion*, vol. 39, No. 1, pp. 1315–1326, 1997.
- [43] P. Kubes, M. Paduch, T. Pisarczyk, M. Scholz, T. Chodukowski, D. Klir, J. Kravarik, K. Rezac, I. Ivanova-Stanik, L. Karpinski, K. Tomaszewski, E. Zielińska, “Interferometric Study of Pinch Phase in Plasma-Focus Discharge at the Time of Neutron Production”, *IEEE Trans. on Plasma Sci.*, vol. 37, No. 11, pp. 2191-2196, 2009.
- [44] M. Zakaullah, I. Akhtar, G. Waheed, “Imaging of fusion reaction zone in plasma focus”, *Journ. of Fusion Energy*, vol. 6, no. 8, pp. 3188-3193, 1999.
- [45] A. J. Toepfer, D. R. Smith, E. H. Beckner, “Ion Heating in the Dense Plasma Focus”, *The Physics of Fluids*, vol. 14, No. 1, pp. 52-61, 1971.
- [46] J. P. Baconnet, G. Cesari, A. Coudeville, J. P. Watteau, “90° laser light scattering by a dense plasma focus”, *Phys. Lett. A*, vol. 29, No. 1, pp. 19-20, 1969.
- [47] W. Harries, J. Lee, D. McFarland, “Trajectories of high energy electrons in a plasma focus”, *Plasma Phys.*, vol. 20, No. 2, pp. 95-106, 1978.
- [48] A. B. Bud’Ko, F. Felber, A. I. Kleev, “Stability analysis of dynamic Z pinches and theta pinches”, *Phys. of Fluids B*, vol. 3, No. 1, pp. 598-607, 1989.

- [49] P. Gautam, R. Khanal, “Introduction to numerical experiment on plasma focus using Lee model code”, *Himalayan Phys.*, vol. 5, no. 5, pp. 137-141, 2014.
- [50] J. Cooper, “Plasma spectroscopy”, *Reports on Prog. in Phys.*, vol. 29, no. 35, pp. 99-102, 1966.
- [51] S. Al-Hawat, M. Akel, C. Wong, “X-ray emission from argon plasma focus contaminated with copper impurities in AECS PF-2 using five channel diode spectrometer”, *Journ. of Fusion Energy*, vol. 30, no. 6, pp. 503-508, 2011.
- [52] C. S. Wong, R. Mongkolnavin, “Elements of plasma technology”, *Springer Sci. + Business Media*, 2016.
- [53] I. H. Hutchinson, “Principles of plasma diagnostics”, *Cambridge Uni. Press*, 1987.
- [54] E. Gullikson, “X-Ray Interactions With Matter”, http://henke.lbl.gov/optical_constants/. [Accessed: 01-May-2015].
- [55] T. Fujimoto, “Plasma Spectroscopy”, *Oxford Sci. Publ.*, 2004.
- [56] D.M. Poole, “X-ray absorption edges, characteristic X-ray lines and fluorescence yields”, http://www.kayelaby.npl.co.uk/atomic_and_nuclear_physics/4_2/4_2_1.html. [Accessed: 01-May-2015].
- [57] H. K. Chung, M. Chen, R. W. Lee, Y. Ralchenko, “FLYCHK: Generalized population kinetics and spectral model for rapid spectroscopic analysis for all elements”, <https://nlte.nist.gov/FLY/>. [Accessed: 01-May-2015].
- [58] F. Karami, M. Roshan, M. Habibi, R. Asadnejad, P. Lee, S. Saw, S. Lee, “Neutron yield scaling with inductance in plasma focus”, *IEEE Trans. on Plasma Sci.*, vol. 443, no. 7, pp. 2155-2158, 2015.
- [59] S. Saw, S. Lee, “Scaling laws for plasma focus machines from numerical experiments”, *Energy and Power Engg.*, vol. 2, no. 1, pp. 65-72, 2010.

- [60] L. Soto, P. Silva, J. Moreno, G. Silvester, M. Zambra, C. Pavez, L. Altamirano, H. Bruzzone, M. Barbaglia, Y. Sidelnikov, W. Kies, “Research on Pinch Plasma Focus Devices of Hundred of Kilojoules to Tens of Joules”, *Braz. Journ. of Physics*, vol. 34, no. 4B, pp. 1814-1821, 2004.
- [61] M. Zakaullah, K. Alamgir, A. Rasool, M. Shafiq, G. Murtaza, A. Waheed, “Correlation of plasma electron temperature with neutron emission in a low-energy plasma focus”, *IEEE Trans. on Plasma Sci.*, vol. 29, no. 1, pp. 62-68, 2001.
- [62] R. A. Behbahani, “Enhancement of Charged Particle Emission from a Plasma Focus Device”, Doctoral dissertation, *University of Saskatchewan, SK*, 2017. [Retrieved from <https://ecommons.usask.ca/bitstream/handle/10388/8121/ALIBAZIBEHBAHANI-DISSERTATION-2017.pdf?sequence=1>].
- [63] L. Jakubowski, M.J. Sadowski, “Hot-Spots in Plasma-Focus Discharges as Intense Sources of Different Radiation Pulses”, *Braz. J. Phys.*, vol.32, no.1, pp. 1-5, 2002.
- [64] P. Silva, M. Favre, “Properties of hot-spots in Plasma Focus discharges operating in Hydrogen-gas mixtures”, *Intl. Conf. on High-Power Part. Beams*, pp. 245-248, 2002.
- [65] M. Roshan, S. Razaghi, F. Asghari, R. S. Rawat, S. V. Springham, P. Lee, S. Lee, T. L. Tan, “Potential medical applications of the plasma focus in the radioisotope production for PET imaging”, *Phys. Lett. A*, vol. 378, No. 30, pp. 2168-2170, 2014.
- [66] S. H. Saw, V. Damideh, J. Ali, R. S. Rawat, P. Lee, S. Lee, “Damage Study of Irradiated Tungsten using fast focus mode of a 2.2 kJ plasma focus”, *Vacuum*, vol. 144, no. 1, pp. 14-20, 2017.
- [67] V. Gribkov, A. Srivastava, P. Keat, V. Kudryashov, S. Lee, “Operation of NX2 dense plasma focus device with argon filing as a possible radiation source for micro-machining”, *IEEE Trans. on Plasma Sci.*, vol. 30, no. 3, pp. 1331-1338, 2002.

- [68] M. Izurieta, E. Ramos-Moore, L. Soto, “Morphological and structural effects on tungsten targets produced by fusion plasma pulses from a table top plasma focus”, *Nucl. Fusion*, vol. 55, no. 9, pp. 1-8, 2015.
- [69] R. A. Behbahani, A. Hirose, C. Xiao, “Formation of a dual-stage pinch-accelerator in a Z-pinch (plasma focus) device”, *A Lett. Journ. Expl. the Front. of Phys.*, vol. 121, no. 2, pp. 1-4, 2018.